



Leveraging Nucleated Graphitization for Super-Strong and Deformation Sensing Hybrid Nanomaterials

Mohammad Naraghi
TEXAS ENGINEERING EXPERIMENT STATION COLLEGE STATION

11/01/2019
Final Report

DISTRIBUTION A: Distribution approved for public release.

Air Force Research Laboratory
AF Office Of Scientific Research (AFOSR)/ RTA1
Arlington, Virginia 22203
Air Force Materiel Command

DISTRIBUTION A: Distribution approved for public release.

REPORT DOCUMENTATION PAGE		<i>Form Approved</i> <i>OMB No. 0704-0188</i>	
<p>The public reporting burden for this collection of information is estimated to average 1 hour per response, including the time for reviewing instructions, searching existing data sources, gathering and maintaining the data needed, and completing and reviewing the collection of information. Send comments regarding this burden estimate or any other aspect of this collection of information, including suggestions for reducing the burden, to Department of Defense, Executive Services, Directorate (0704-0188). Respondents should be aware that notwithstanding any other provision of law, no person shall be subject to any penalty for failing to comply with a collection of information if it does not display a currently valid OMB control number.</p> <p>PLEASE DO NOT RETURN YOUR FORM TO THE ABOVE ORGANIZATION.</p>			
1. REPORT DATE (DD-MM-YYYY) 21-05-2020	2. REPORT TYPE Final Performance	3. DATES COVERED (From - To) 01 Aug 2015 to 31 Jul 2019	
4. TITLE AND SUBTITLE Leveraging Nucleated Graphitization for Super-Strong and Deformation Sensing Hybrid Nanomaterials		5a. CONTRACT NUMBER	
		5b. GRANT NUMBER FA9550-15-1-0170	
		5c. PROGRAM ELEMENT NUMBER 61102F	
6. AUTHOR(S) Mohammad Naraghi		5d. PROJECT NUMBER	
		5e. TASK NUMBER	
		5f. WORK UNIT NUMBER	
7. PERFORMING ORGANIZATION NAME(S) AND ADDRESS(ES) TEXAS ENGINEERING EXPERIMENT STATION COLLEGE STATION 1470 WILLIAM D FITCH PKY COLLEGE STATION, TX 77843-3577 US		8. PERFORMING ORGANIZATION REPORT NUMBER	
9. SPONSORING/MONITORING AGENCY NAME(S) AND ADDRESS(ES) AF Office of Scientific Research 875 N. Randolph St. Room 3112 Arlington, VA 22203		10. SPONSOR/MONITOR'S ACRONYM(S) AFRL/AFOSR RTA1	
		11. SPONSOR/MONITOR'S REPORT NUMBER(S) AFRL-AFOSR-VA-TR-2020-0008	
12. DISTRIBUTION/AVAILABILITY STATEMENT A DISTRIBUTION UNLIMITED: PB Public Release			
13. SUPPLEMENTARY NOTES			
14. ABSTRACT Our overarching goal in this project has been to develop microstructural design and scalable processing capabilities of carbon nanomaterials with unprecedented mechanical strength, surpassing carbon fibers, and tailorable electromechanical coupling. The focus was on carbon nanofibers (CNFs). To achieve the goal, we have accomplished the following as discussed in section 4. In section 4.1, we performed a systematic study on mechanics of CNFs in relation to their microstructure. The CNFs were fabricated via pyrolysis of polymeric nanofibers. In order to develop super-strong and super-tough one-dimensional nanomaterials, processing steps were aimed at reducing defects, e.g., poor graphitic alignment. The degree of graphitization was controlled to benefit from strong graphitic bonds while avoiding strength-compromising interactions between graphitic domains. The best processing condition led to record high average strength of 6.30.8 GPa (7.7 GPa maximum), 66% higher than previous reports. More importantly and contrary to most engineering materials, the high strength was achieved together with remarkable energy to failure. The CNF exhibited significant ductility of 3.00.7 %, with energy-to-failure of over 80 J/g, the highest reported for graphitic fibers. The research on simultaneously strong and tough CNF provides a promising pathway to develop the next generation of nanoscale reinforcements for lightweight and safety-critical structural applications. [Sources: Carbon, 109, 813-822 (2016), Carbon, 117, 208-219 (2017), Carbon 137, 242-251 (2018)]			
15. SUBJECT TERMS carbon fiber, composites			
16. SECURITY CLASSIFICATION OF:			

Standard Form 298 (Rev. 8/98)
Prescribed by ANSI Std. Z39.18

DISTRIBUTION A: Distribution approved for public release.

a. REPORT Unclassified	b. ABSTRACT Unclassified	c. THIS PAGE Unclassified	17. LIMITATION OF ABSTRACT UU	18. NUMBER OF PAGES	19a. NAME OF RESPONSIBLE PERSON TILEY, JAIMIE
					19b. TELEPHONE NUMBER <i>(Include area code)</i> 703-588-8316

Final Report, Year 4 (one year extension):

AIR FORCE OFFICE OF SCIENTIFIC RESEARCH

Reporting Period: 08/01/2015-07/31/2019

Young Investigator Research Program

Funding opportunity Number: BAA-AFOSR-2014-0003

Complex Material and Devices (RTD): Low Density Materials,
Dr. Jamie Tiley (Former PMs Drs. Joycelyn Harrison and then Kenneth Goretta)

Leveraging Nucleated Graphitization for Super-Strong and Deformation Sensing Hybrid Nanomaterials

Principal Investigator:

Mohammad Naraghi, Associate professor, Texas A&M University, Department of Aerospace Engineering, College Station TX 77843-3141

Email: Naraghi@Aero.tamu.edu

Tel: 979-862-3323

Table of Contents

Pages

Contents

Table of Contents	Pages	2
Abstract of the Report		3
1. Publications based on the above efforts		4
2. Patents and Invention Disclosure		5
3. Graduated Students and Degrees Awarded		6
4. Detailed description of the accomplishments		7
4.1. Mechanics of CNFs with preferentially aligned graphitic domains (Obj 1)		7
Experimental Section		7
Results and Discussion		9
Conclusions of this section		18
4.2. Effect of graphitic templating on Mechanics of carbon nanofibers		19
Experimental Section		19
Results and Discussion		20
Conclusion of this section		28
4.3. Numerical Analysis of Electrical Conduction in Hybrid Nanomaterials		30
Model Development		30
Results and Discussion		33
Conclusion of this section		38
4.4. Formation of Wavy and Helical CNFs with Controlled Morphology		40
Experimental Section		40
Theoretical analysis for the formation of wavy/helical CNFs		41
Results and Discussions		45
Conclusion of this section		50
4.5. Mechanics of Porous CNFs with Application To Energy Storage		51
Experimental Section		51
Results and Discussion		52
Conclusion of this section		59
4.6. Production of Graphene Nanoparticles and single layer graphene from graphite and expanded graphite via rod milling		61
Results		62
References		63

Abstract of the Report

Our overarching goal in this project has been to develop microstructural design and scalable processing capabilities of carbon nanomaterials with unprecedented mechanical strength, surpassing carbon fibers, and tailorable electromechanical coupling. The focus was on carbon nanofibers (CNFs). To achieve the goal, we have accomplished the following as discussed in section 4.

In section 4.1, we performed a systematic study on mechanics of CNFs in relation to their microstructure. The CNFs were fabricated via pyrolysis of polymeric nanofibers. In order to develop super-strong and super-tough one-dimensional nanomaterials, processing steps were aimed at reducing defects, e.g., poor graphitic alignment. The degree of graphitization was controlled to benefit from strong graphitic bonds while avoiding strength-compromising interactions between graphitic domains. The best processing condition led to record high average strength of 6.3 ± 0.8 GPa (7.7 GPa maximum), 66% higher than previous reports. More importantly and contrary to most engineering materials, the high strength was achieved together with remarkable energy to failure. The CNF exhibited significant ductility of 3.0 ± 0.7 %, with energy-to-failure of over 80 J/g, the highest reported for graphitic fibers. The research on simultaneously strong and tough CNF provides a promising pathway to develop the next generation of nanoscale reinforcements for lightweight and safety-critical structural applications. [Sources: *Carbon*, **109**, 813-822 (2016), *Carbon*, **117**, 208-219 (2017), *Carbon* **137**, 242-251 (2018)]

Having learnt the benefits of isolated graphitic domains within the structure of CNFs, in section 4.2, we addressed a lingering question about the potential effect of templated graphitization on mechanics of CNFs. The templated graphitization refers to the conversion of certain polymers such as polyacrylonitrile to highly graphitic structures when carbonized in atomic vicinity of a graphitic nanoparticle such as CNTs. While this phenomenon is manifested by the formation of highly-ordered graphitic (HOG) microstructures, it is not clear whether it leads to stronger nanostructures, or on the contrary, factors such as elastic mismatch between HOG and the rest of the carbonized structures can lead to premature failure due to stress concentration. In this work, the templating effect of functionalized single-walled CNTs in CNFs and its influence on the microstructure and mechanical properties of hybrid CNFs are studied. To improve the alignment of CNTs and polymer chains, and packing density of chain on surface of CNTs, the as-fabricated precursor nanofibers were subjected to hot-drawing. The correlation between the microstructure of precursor nanofibers and CNFs revealed the crucial effect of chain alignment in precursor on defect density in CNFs, and thus their mechanical properties. Through continuum models describing the mechanics of CNFs and comparison with experiments, existence and evolution of the high-performance HOG around the CNTs and its reinforcing effect on the overall mechanical property of CNF were demonstrated. [Sources: *Acta Materialia*, **162**, 46-54 (2018)]

We then focused on electromechanical couplings in CNFs, i.e., the piezoresistivity. We developed a comprehensive multi-resolution two-dimensional (2D) resistor network model, as described in section 4.3, to analyze the electrical conductivity of hybrid nanomaterials made of insulating matrix with conductive particles such as CNT reinforced nanocomposites and thick film resistors. For the first time in the open literature, our model took into account the impenetrability of the particles and their random placement within the matrix, and presented a detailed description of intra-particle conductivity via finite element analysis, while the inter-particle conductivity is assumed to be primarily due to electron tunneling. The model was then used to predict the electrical conductivity of electrospun carbon nanofibers as a function of microstructural parameters such as turbostratic domain alignment and aspect ratio. To simulate the microstructure of single CNF, random positioned nucleation sites were seeded and grown as turbostratic particles with anisotropic growth rates. Particle growth were in steps and growth of each particle in each direction was stopped upon contact with other particles. The study pointed to the significant contribution of both intra-particle and inter-particle conductivity to the overall conductivity of hybrid composites. Influence of particle alignment and anisotropic growth rate ratio on electrical conductivity was also discussed. The results unraveled approaches to enhance electrical conductivity of hybrid materials through controlling their

microstructure which is applicable not only to carbon nanofibers, but also many other types of hybrid composites such as thick film resistors. [Sources: *Modelling Simul. Mater. Sci. Eng.* **24**, 065004 (15pp) (2016)]

An unintended consequence of the work that was carried out in this research was the development of wavy nanofibers and nanocoils. These structures were formed while the team of the PI had attempted to align the chains of the precursor (polyacrylonitrile) by placing it within another polymer matrix, followed by co-drawing to achieve orientation-induced alignment. An initially miscalculated step led to the formation of the wavy nanofibers and nanocoils, with broad application base, including antennas and flexible electronics. In section 4.4, we presented this approach to develop carbon nanofibers, in which their controllable waviness will provide them adjustable deformability with minimal internal stresses in their unloaded wavy state for flexible electronic applications. The method to produce them is based on matrix restricted shrinkage of composite precursor nanofiber which induces microbuckling during the thermal stabilization process. We then developed mechanistic models which can predict the formation of 2D wavy or 3D helical nanostructures as well as the wavelength/amplitude/pitch of the forming structures. [Sources: *Journal of the Mechanics and Physics of Solids (JMPS)*, **In press** (2019)]

In section 4.5 we investigated the multifunctional capabilities of CNFs with a particular application to structural energy storage. The structural energy storage materials belong to an emerging field of materials and refer to a broad category of multifunctional materials which can simultaneously provide load-bearing and energy storage to achieve weight reduction in weight-sensitive applications. Reliable and satisfactory performance in each function, load bearing or energy storage, requires peculiar material design with potential trade-offs between them. In this section, the tradeoffs between functionalities in an emerging class of nanomaterials, carbon nanofibers (CNFs) is unraveled. The CNFs were fabricated by emulsion and coaxial electrospinning and activated by KOH at different activation conditions. The effect of activation on supercapacitor performance was analyzed using two electrode test cells with aqueous electrolyte. Porous CNFs show promising energy storage capacity (191.3 F g⁻¹ and excellent cyclic stability) and load-bearing capability (strength of over 1 GPa). While activation enhances surface area and capacitance, it introduces flaws in material, such as nanopores, reducing mechanical properties. It was found that moderate activation can lead to dramatic improvement in capacitance (by >300%), at a rather moderate loss in strength (< 17%). The gain in specific surface area and capacitance in CNFs is many times those observed in bulk carbon structures, such as carbon fibers, indicating that activation is mainly effective near the free surfaces and for low-dimensional materials. [Sources: *ACS Applied Materials and Interfaces*, **10**, 38310-38318 (2018), *Advanced Functional Materials* 1901425 (2019)]

Lastly, in section 4.6, we have presented a novel method to mass produce graphene, which can be used as reinforcement of our CNFs to induce templated graphitization. The method is based on rod-milling of graphite, which is employed to more effectively distribute the impact forces between rods and graphite particles in a milling jar. We intend to use the method as a basis to develop superstrong CNFs by benefiting from the so-called templated graphitization (similar to section 5.2) to investigate the effect of defects in graphitic nuclei on mechanics of CNFs. [Source: invention disclosure].

The work has also led to two invention disclosures, one fully filed and the other one in process. Certain entrepreneurial activities, including forming startups, are being pursued.

1. Publications based on the above efforts

Peer Reviewed Journal Papers

1. Khatri S., Cai J. and Naraghi M., "Formation of Wavy Carbon Nanofibers and Nanocoils via Precursor Constrained Microbuckling", *Journal of the Mechanics and Physics of Solids (JMPS)*, In press (2019)

2. Chen Y., Amiri A., Boyd J. and Naraghi M., “Promising Trade-Offs Between Energy Storage and Load Bearing in Carbon Nanofibers as Structural Energy Storage Devices”, **Advanced Functional Materials** 1901425 (2019) *–[IF ~15.6]*
3. Chen Y., Cai J., Boyd J., Kennedy J. and Naraghi M., “Mechanics of Emulsion Electrospun Porous Carbon Fibers as Building Blocks of Multifunctional Materials”, **ACS Applied Materials and Interfaces**, 10, 38310-38318 (2018)
4. Cai J. and Naraghi M., “The formation of highly ordered graphitic interphase around embedded CNTs controls the mechanics of ultra-strong carbonized nanofibers”, **Acta Materialia**, 162, 46-54 (2018)
5. Cai J. and Naraghi M., “Non-intertwined graphitic domains leads to super strong and tough continuous 1D nanostructures”, **Carbon** 137, 242-251 (2018).
6. Chawla S., Cai J. and Naraghi M., “Mechanical tests on individual carbon nanofibers reveals the strong effect of graphitic alignment achieved via precursor hot-drawing”, **Carbon**, 117, 208-219 (2017). *–[cited 21]*
7. Cai J., Chawla S., and Naraghi M., “Microstructural Evolution and Mechanics of Hot-drawn CNT-Reinforced Polymeric Nanofibers”, **Carbon**, 109, 813-822 (2016). *–[cited 24]*
8. Cai J. and Naraghi M., “Computational Analysis of Electrical Conduction in Hybrid Nanomaterials with Embedded Non-penetrating Conductive Particles”, **Modelling Simul. Mater. Sci. Eng.** 24, 065004 (15pp) (2016).
9. Ruaa Yaseen Hammoudi Al-Mezrakchi, Mohammad Naraghi, “Interfused nanofibres network in scalable manufacturing of polymeric fibres via multi-nozzle electrospinning”, *Micro & Nano Letters*, Volume 13, Pages 536-540, 2018

Conference Proceedings

1. Jizhe Cai, Sumit Khatri and Mohammad. Naraghi, “Electrospun Carbon nanofiber with controllable waviness as stretchable conductor”, AIAA SciTech Forum, 8–12 January 2018, Kissimmee, Florida
2. Jizhe Cai and Mohammad. Naraghi, “Effect of Templating Graphitization of Functionalized SWNTs on Mechanical Properties of Hot-drawn Carbon Nanofibers”, AIAA SciTech Forum, 8–12 January 2018, Kissimmee, Florida

2. Patents and Invention Disclosure

There has been two invention disclosures filed by the PI. Their status and titles are listed below:

Title	List of co-inventors	Status	Next steps
Production of Graphene Nanoparticles and single layer graphene from graphite and expanded graphite via rod milling	Ahmad Amiri Mohammad Naraghi	Invention disclosure filed on 05/21/2018	Exclusive licensing privileges is given to an startup company, Carbon Gates Technologies, LLC, founded by the co-inventors. The company has applied for NSF-SBIR to pursue the idea.
Architecture-, geometry- and microstructure-	Mohammad Naraghi	Filed on 07/24/2018 to	The disclosure was the centerpiece for a DOD funded I-Corp project for

controlled processing of carbon fibers and nanofibers via pyrolysis of multicomponent hot-drawn precursors	James G Boyd Jizhe Cai Yijun Chen	TAMU commercialization office, pending the export control check	customer discovery, with the goal of forming a Startup company around it.
--	---	---	---

3. Graduated Students and Degrees Awarded

The following students has been in part supported by this AFOSR award

- Sneha Chawal (PhD, Materials Science and Engineering, 2016)
- Jizhe Cai (PhD, Aerospace Engineering, 2017)
- Sumit Khatri (MSc, Aerospace Engineering, 2019)
- Yijun Chen (PhD, expected to graduate in Spring 2020)

4. Detailed description of the accomplishments

4.1. Mechanics of CNFs with preferentially aligned graphitic domains (Obj 1)

A systematic study on mechanics of carbon nanofibers (CNF) in relation to their microstructure is presented. The CNFs were fabricated via pyrolysis of polymeric nanofibers. In order to develop super-strong and super-tough one-dimensional nanomaterials, processing steps were aimed at reducing defects, e.g., poor graphitic alignment. The degree of graphitization was optimally controlled to benefit from strong sp² C-C bonds while avoiding strength-compromising interactions between graphitic domains. The peculiar feature in CNFs was the discontinuity and rather uniform dispersion of turbostratic domains within the amorphous carbon, an apparent cause of crack pinning, and path deflection, thus strengthening/toughening. Hence, our CNFs exhibited superior strength compared to other emerging high-performance continuous fibers, such as CNT and graphene fibers. The best processing condition led to record high average strength of 6.3±0.8 GPa (7.7 GPa maximum), 66% higher than previous reports. Moreover and contrary to most engineering materials, the high strength was achieved at no cost to ductility. The CNF exhibited significant ductility of 3.0±0.7 %, with energy-to-failure as high as 86 J/g, the highest reported for graphitic fibers. The research on simultaneously strong and tough CNF provides a promising pathway to develop the next generation of nanoscale reinforcements for lightweight and safety-critical structural applications.

Experimental Section

In contrast to the growth synthesis methods which are based on the addition of C atoms to a growing nanomaterial, the pyrolysis-based techniques mainly rely on removal of non-carbonaceous atoms from the

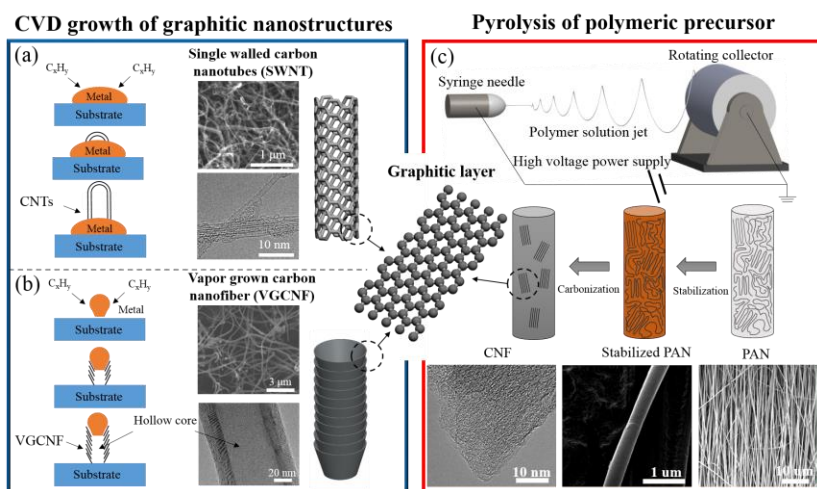


Figure 1. Schematic diagram of fabrication processes, SEM and TEM images of (a) single walled CNTs, (b) VGCNFs and (c) electrospun CNFs.

precursor at elevated temperatures (Figure 1). Relative to CVD approaches, processing of carbon nanofibers (CNF) via carbonization of electrospun PAN nanofibers provides ample opportunities to control the microstructure and defects of the nanofibers, such as degree of graphitization and graphitic domain alignment with ease 15-16. In addition, since the precursor of carbonized fibers is a polymer, often polyacrylonitrile (PAN), the presence of long chains can be utilized to develop nearly continuous strands of precursors and thus CNFs which are highly sought for in structural composites (similar to continuous carbon fibers, CF, used in conventional composites). This is in stark contrast to CVD grown CNTs and VGCNFs with overall length of less than ~10s of microns, limited by the complexities of a growing structure in CVD reactor 17. Although some ultralong CNTs had been developed in recent years 18-19, the problems associated with mass-production of such long CNTs evidently limits their application in developing high performance structural materials.

In an attempt to develop a superstrong and supertough carbon nanomaterial via highly scalable pyrolysis techniques, we studied the mechanical properties of PAN homopolymer-based electro-spun CNFs in relation to their microstructure. Our efforts were motivated by continuum and atomistic models of pyrolyzed nanostructures which predict that the strength of CNFs can reach values in excess of 14 GPa 10-11, 20-21. Despite such promising predictions, the highest experimentally achieved strength of CNFs is ~

4 GPa 15-16 (for gauge length 25 μ m or higher). The efforts to augment the strength of CNFs have relied on enhancing the chain alignment in the precursor as a means to augment graphitic alignment in CNFs 16, controlling the concentration of graphitic domains 15, applying restricting force during carbonization 22 and adding graphitic nanofillers to restrict polymer chain shrinkage during the fabrication process and introduce templating graphitization 23-24. In contrast to the existing literature and complementary to that, our efforts presented here to achieve record high strength CNFs has been aimed at reducing certain defects in CNFs, such as poor graphitic alignment, and also to achieve optimal degree of graphitization, primarily to avoid strength compromising interactions between graphitic domains 15, 25. Our studies shows that through proper engineering of the microstructure of CNFs, strength of CNFs can be significantly enhanced. Interestingly, the remarkable strength of CNFs has come with added benefits in terms of energy to failure and ductility. That is, compared to other pyrolyzed structures such as CFs, our electrospun CNF shows remarkably high failure strain and toughness, which is explained in terms of microcrack arresting mechanisms within amorphous carbon matrix by non-intertwined graphitic domains both present in the CNFs. The presence of such flaw-tolerant mechanisms have led to unprecedented high strength and energy to failure among continuous carbon nanostructures, values as high as 7.7 GPa and 86 J/g, respectively. The proposed failure mechanism of electrospun CNFs with both high strength and toughness provides new pathway for developing high-performance structural fibers in both academia and industry. The processing of CNFs via spinning the precursor (similar to carbon fibers), as opposed to more complex and poorly scalable vapor deposition methods can in principle bring about excellent mechanical performance at an affordable cost.

Fabrication of CNFs: Polyacrylonitrile (PAN) precursor nanofiber ribbon was fabricated via electrospinning. The 10 wt.% homopolymer PAN solution was obtained by dissolving PAN powder ($M_w = 150,000$ g/mol) in Dimethylformamide (DMF) solvent (both from Sigma–Aldrich). The flow rate of electrospinning was set to ~ 0.8 ml/hr to obtain stable jet. Rotating target was used to obtain aligned polymer nanofiber ribbon with ~ 5.7 m/s peak-up velocity, at voltage and distance of 25 kV and 20 cm, as described in our previous work ¹. The PAN nanofiber ribbons were then drawn to different ratios, ranging from $\lambda = 1$ to 3 (hot-drawing ratio = final length/initial length of ribbon) by applying an engineering stress of ~ 19 MPa in an oven at a temperature of 135 $^{\circ}$ C.

Following that, the PAN precursor nanofiber were thermally stabilized at 290 $^{\circ}$ C for 2 hours in air. FT-IR was used to characterize the stabilization reaction extent under different conditions, such as temperature and time. Based on the calculated ring cyclization index RCI (the ratio of intensity of the C=N to the sum of the intensities of C=N and C \equiv N), optimum condition for stabilization was chosen, as described elsewhere ². During the stabilization, an engineering stress of 5 MPa was applied to the hot-drawn ribbons via hanging weights to constrain the shrinkage and maintain the chain alignment during the stabilization reaction. Carbonization was carried out in tube furnace (MTI, GSL-1700x) at 1400 $^{\circ}$ C for 2 hours under inert gas (N₂) environment in a stress free state.

Microstructural characterization: The carbon nanotubes and VGCNFs used for SEM and TEM imaging in Fig. 1 are P3-SWNT from Carbon Solutions, Inc. and PR-24-XT-PS from Applied Science Inc., respectively. The surface morphology of PAN and carbon nanofiber was characterized by using FEI Quanta 600 FE-SEM. The X-ray diffraction spectrums of PAN and CNFs ribbons (XRD) (CuK α , wavelength of 0.154 nm) were obtained using GADDS BRUKER-AXS MWPC 3-thiracle X-ray Diffractometer. The crystallinity of PAN precursor nanofiber was calculated based on the relative area under the deconvoluted crystalline and amorphous peaks by using Lorentzian fitting in Origin 9.0 ^{3,4}. The process for calculating crystallinity within PAN nanofiber was thoroughly discussed in previous literature by other researcher and also in our works ^{2,4,5}. The PAN crystallite size in PAN precursor and CNFs were calculated from PAN (110) and CNFs (002), by using Scherrer's equation ($K = 0.89$) ⁶. The orientation of the PAN chains in the crystalline phase was determined based on the azimuthal scans of the diffraction peak at $2\theta \sim 17^{\circ}$ ⁷. Orientation of CNFs crystallites (turbostratic domains) was determined from the azimuthal scan at $2\theta = 25^{\circ}$

⁸. Herman's orientation factor of PAN crystallite and CNFs crystallite were obtained from the following equations based on WAXD azimuthal curves of PAN (110) and CNFs (002) diffraction peaks:

$$\langle \cos^2\psi \rangle = \frac{\int_{-\frac{\pi}{2}}^{\frac{\pi}{2}} I(\psi) \cos^2(\psi) \sin(\psi) d\psi}{\int_{-\frac{\pi}{2}}^{\frac{\pi}{2}} I(\psi) \sin(\psi) d\psi}, \quad f = \frac{3\langle \cos^2\psi \rangle - 1}{2}$$

where ψ is off axis angel, I is diffraction intensity, and f is the Herman's orientation factor. Graphitic structure within the CNF was characterized by using Horiba Jobin-Yvon LabRam Raman Confocal Microscope with a He-Ne laser (633nm). The averaged I_D/I_G ratio and crystallite size were obtained based on three measurements. Curve fittings were carried out in Origin 9.0 with Lorentzian fitting. CNF ribbon was broken in tension. Then, individual broken CNF in the broken region of the ribbon was dispersed in DI water by ultrasonication. The solution containing individual broken CNF was dropped on the regular TEM grid and left to dry for the following TEM test. FEI Tecnai G2 F20 transmission electron microscope (TEM) was used to characterize the graphitic structure of CNF, and selected area electron diffraction (SAED) was applied to measure the alignment of turbostratic domains within CNFs. The obtained averaged full width at half maximum (FWHM) of (002) arc of CNFs in SAED pattern was reported based on five measurements. The density of CF (1.76 g/cm³) is used to calculate specific properties of CF and CNFs, due to process and structural similarity between the two.

Mechanical testing of individual nanofiber: The mechanical property of individual CNFs was studied by using a MEMS-based nano-mechanical testing platform. After mounting individual CNFs on MEMS device with 3D-manipulator controlled sharpened tungsten tip, Tescan LYRA-3 focused ion beam (FIB) was used to deposit platinum (Pt) block on it to fix it on device. Then, the MEMS device with Pt block fixed nanofiber was mounted on stage with one-dimensional controllable motion ability. While the stage was actuated, optical images of the load cell in the device was captured via an optical microscope. Digital Image Correlation was used to calculate the displacement of different parts in the MEMS device, which combined with the stiffness of the load cell, the stress-strain curve of individual CNF tensile test was obtained. The cross-section area of CNFs used to calculate the stress in CNFs was obtained from the diameter of the failure position. The force and strain resolution of the MEMS device was 4 MPa and 0.1%, which is suitable for characterizing the modulus and strength of individual CNF. More details of the testing apparatus can be found in our previous work ^{2,9}.

Results and Discussion

Microstructure of CNF and CF Precursors: The microstructure and properties of CNFs are highly dependent on factors such as the degree of graphitization and graphitic alignment ^{2,10,11}. Among these parameters, alignment of turbostratic (defective graphitic) domains is strongly dependent on precursor chain alignment. Higher alignment of precursor chains can effectively enhance graphitic alignment in CNFs, and thus, lead to CNFs with improved strength and modulus ². The enhancement in chain alignment can be achieved to some extent via electromechanical drawing forces applied onto electrospinning jet, but more effectively via hot-drawing the as-electrospun nanofibers ². The chain alignment can even lead to orientation-induced crystallization, as has been demonstrate in PAN ^{2,4} and other polymer nanofibers ^{1,12,13}. On the other hand, excessive hot-drawing may induce defects in the precursor, such as chain scissor or voids, which can compromise the strength of the resulting CNFs. For instance, in a prior study, it was demonstrated that increasing the hot-drawing ratio from $\lambda = 2$ to $\lambda = 4$ increased the scatter in the strength of CNFs with no effective improvement in the average strength, suggesting defect accumulations in the precursor ². Therefore, in this work, $\lambda = 3$ is chosen to be the maximum hot-drawing ratio applied to as-electrospun PAN nanofibers to induce chain alignment as a means to develop high strength CNFs.

The microstructure of the PAN nanofibers as a function of the draw ratio, studied via X-ray diffraction method (Experimental section), is presented in Table 1. As shown in the table, hot-drawing of the precursor significantly increases the crystallinity, crystallite size and alignment of chains within the crystalline

domain. For instance, hot-drawing the PAN precursor nanofiber to $\lambda = 3$ (average diameter $\sim 190\text{nm}$) in this work led to an enhancement in crystallinity, crystallite size and Herman's orientation factor of crystallite phase to 31%, 6.7 nm and 0.74, respectively, from a nearly amorphous state in as-electrospun nanofibers ($\lambda = 1$). That is, hot-drawing of the precursor above the glass transition temperature of PAN enhanced the mobility of PAN chains and facilitated chain alignment. It also led to a more densely packed arrangement of polymer chains. These results are in line with our prior findings on the effect of hot-drawing on the microstructure of PAN ^{1,2}.

It is also illustrative to compare the morphology of PAN chains in hot-drawn electrospun nanofibers with the morphology of PAN chains obtained via other fabrication processes. For instance, PAN homopolymer microfibers made from wet-spinning exhibit higher crystallinity and crystallite phase alignment ¹⁴. This is partly due to the swelling caused by the residual solvent which weakens the interactions between chains and allows for significantly higher draw ratios in wet-spun fibers. Drawing-induced chain alignment can continue until the crystalline domains which suppress chain mobility are formed ¹⁴. In addition, gel-spun PAN fibers can achieve larger crystallite domains compared to electrospun PAN nanofibers, due to reduced entanglement of polymer chain ¹⁵. The chain alignment can also be further enhanced by utilizing PAN copolymers such as Polyacrylonitrile-co-Methacrylic Acid (PAN-co-MAA), instead of PAN homopolymers ¹⁶. The reduced polarity of the precursor chains by introducing MAA monomers lowers the interactions and physical entanglement between chains, thus, allowing for higher draw ratios, chain alignment and crystallinity, as shown in Table 1.

Table 1. Structural parameters comparison between electrospun PAN nanofibers and PAN fibers 25,36,37.

Precursor fabrication	Polymer type	Diameter (μm)	Draw ratio	Crystallinity (%)	Crystallite size (nm)	$f_c(\text{PAN})^*$
Hot-drawn electrospun (this work)	PAN homopolymer	0.31	1	N/A	N/A	N/A
		0.28	2	28	5.9	0.65
		0.19	3	31	6.7	0.74
Wet-spun [36]	PAN homopolymer	12	15	67	6.2	0.85
Gel-spun [25]	PAN homopolymer	10.4	13.5	50	9.2	0.89
Gel-spun [37]	PAN copolymer	20-23	38	65	11.3	0.92

* f_c is Herman's orientation factor of PAN crystallite

In addition to the processing conditions which facilitates chain alignment in gel- and wet- spun fibers, the lower degree of crystallinity of PAN chains in electrospun fibers could also be partly rooted in their sub-micron diameter (larger surface to volume ratio) which promotes solvent evaporation and lowers the residual solvent content of the fibers. As discussed earlier in the context of wet-spun fibers ¹⁴, the residual solvent can act as a plasticizer, facilitating chain reorientation in response to hot-drawing.

Microstructure of CNF: The significant effect of the microstructure of CNFs on their physical properties has been alluded to in previous studies ^{2,17-25}. In this section, the microstructure of CNFs, especially their defect density and graphitic alignment, as a function of processing conditions is studied.

Raman spectroscopy was used to analyze the microstructure of CNFs obtained as a function of the carbonization temperature and precursor hot-drawing ratios, Figure 2. After carbonization of the precursor, two major peaks appear at $\sim 1336\text{ cm}^{-1}$ and $\sim 1580\text{ cm}^{-1}$ corresponding to the D- and G-peak of carbon materials. The ratio of peak intensities, I_D/I_G , can be used as a relative indicator of defect density within the materials with graphitic domains ^{19,26}. By increasing the carbonization temperature from $800\text{ }^\circ\text{C}$ to $1400\text{ }^\circ\text{C}$ in as-electrospun CNFs ($\lambda = 1$, no precursor hot-drawing), there is a gradual decrease in the I_D/I_G ratio from

4.7 to 3.8 (~20%), indicating a reduced defect density in CNFs achieved by employing higher carbonization temperature.

The ratio of peaks in Raman spectrum also allows us to calculate the width (in plane dimension of the graphitic structures, L_a) as: ²⁷

$$\frac{I_D}{I_G} = \frac{C(\lambda_L)}{L_a}$$

where λ_L (= 633nm) is the wavelength of the He-Ne laser used to collect Raman spectrum. The value of the coefficient $C(\lambda_L)$ for the He-Ne incident laser is ~8.3 nm ²⁸. According to this analysis, the width of the graphitic crystallites increases from 1.75 nm to 2.05 nm by increasing the carbonization temperature, consistent with previous studies ^{10,29}. The growth of the turbostratic domains in PAN-based CNFs along the basal plane of the domains (in-plane dimensions) during the carbonization process occurs as a result of the merger of the stabilized PAN chains through dehydration and denitrogenation reactions.

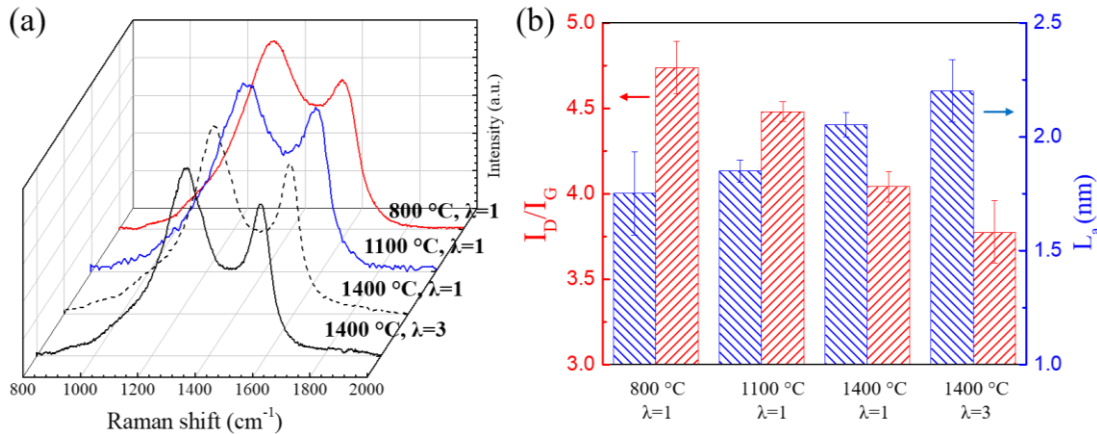


Figure 2. (a) Raman spectrum and (b) I_D/I_G ratios and L_a of CNF with different fabrication conditions.

Increasing the carbonization temperatures, especially from relatively low carbonization temperature can lead to stronger CNFs by promoting the graphitic content of the nanofiber ^{10,30}. However, carbonization at temperatures above 1400 °C may compromise the strength of CNFs ¹⁰ and CF ³¹. Hence, the highest carbonization temperature used in this study was 1400 °C. The loss of strength in CFs fabricated above 1400 °C was observed as early as 1975, ³² but even as recently as 2016 its cause is speculated ³³. A survey of literature suggests that it can be induced by stress concentration along interfaces of partially misaligned turbostratic domains ^{10,31,34}, generation of atomic scale voids due to denitrogenation, ³² or the reduction in the density of covalent crosslinks (sp³ bonds) within turbostratic domains ³³.

Apart from carbonization temperature, the Raman spectrum of the CNFs also shows that the hot-drawing of precursor nanofibers can effectively enhance the graphitic structure within CNFs, Figure 2 (b). For instance, as shown in the figure, the CNFs fabricated by carbonizing the hot-drawn precursor ($\lambda = 3$) have a lower I_D/I_G and thus defect density compared to the CNFs obtained from undrawn precursors ($\lambda = 1$) both fabricated at 1400 °C. Moreover, as shown in Figure 2(b), the reduction in defect density is also accompanied with a widening of the graphitic domains from ~2.05 nm to ~2.2 nm. In other words, denser packing, higher chain alignment, higher degree of crystallinity and larger PAN crystallites in hot-drawn precursors (discussed in previous section and presented in Table 1) which is partly preserved in the following stabilization and carbonization processes, facilitate the merger (zipping) of the cyclized PAN chains during the carbonization, leading to lower defect density of graphitic structure.

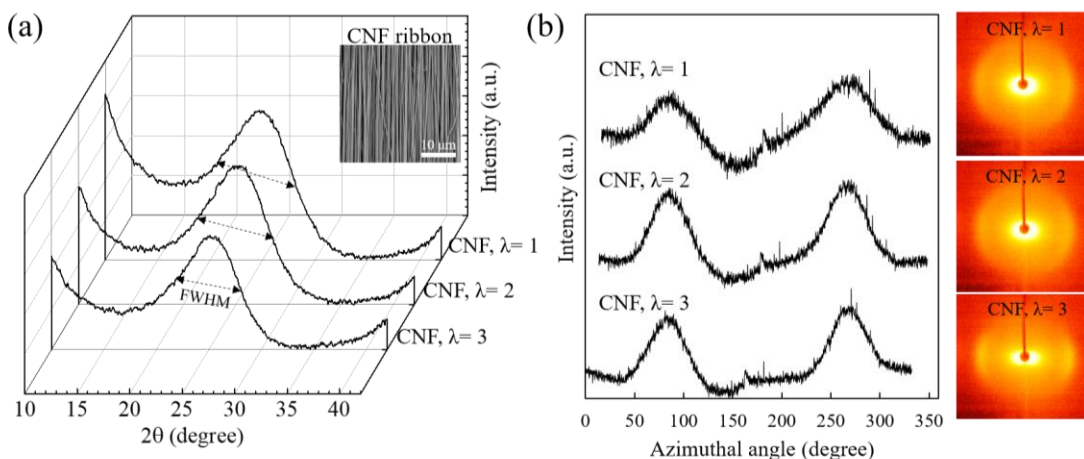


Figure 3. (a) WAXD curve and (b) 2D azimuthal scan of CNFs with different hot-drawing ratios. The SEM image of CNF ribbon in (a) shows good alignment of individual nanofiber along ribbon direction.

Therefore, based on the Raman spectrum of CNFs obtained at various carbonization temperatures, carbonization at 1400 °C resulted in the lowest defect density and widest graphitic domains. The crystalline structure and mechanical properties of CNFs obtained at this temperature was further analyzed. The crystalline structure of CNFs obtained by carbonizing hot-drawn precursors to various hot-drawing ratios at 1400 °C was characterized by WAXD. The appearance of peak at $2\theta \sim 25^\circ$ - 26° , corresponding to (002) plane of the graphitic structure, indicates the formation of graphitic domains in the CNFs, Figure 3, in line with the emergence of the G peak in the Raman spectrum (Figure 2). By increasing the hot-drawing ratio of precursor nanofiber, there is a continuous increase in crystallite thickness (normal to the basal plane of graphitic domains, as measured by using Scherrer's equation with $K = 0.89$) from 1.15 nm in CNFs of undrawn precursors to 1.27 nm in CNFs of hot-drawn precursors with $\lambda = 3$. The increase in crystallite thickness in CNFs via precursor hot-drawing is accompanied with an improvement in the alignment of the crystalline domains within the CNF as indicated by the Herman's orientation factor. For instance, increasing the precursor hot-drawing ratio from $\lambda = 1$ to $\lambda = 3$ led to an increase in the Herman's orientation factor of graphitic domains within CNFs from 0.44 to 0.52. This result reaffirms the direct correlation between chain alignment in the precursor and graphitic alignment in carbonized structures.

The alignment of crystalline domains within CNFs was also studied via SAED, Figure 4. By increasing the hot-drawing ratio of precursors, there is a continuous increase in the alignment of crystalline domains, indicated by a reduction in the full width half maximum (FWHM) of the integrated intensity of (002) arc in SAED pattern. The FWHM of CNFs with $\lambda = 1$ decreases drastically from 86° to 50° for CNFs with $\lambda = 3$, indicating a narrower distribution of crystalline domains in CNFs with hot-drawn precursors.

The SAED is commonly used to characterize the alignment of graphitic domains in CNFs, thus, the FWHM measurements of SAED can be used to compare the graphitic alignments in our work with existing studies. For instance, as shown in Figure 4(b), increasing the carbonization temperature from 1100 °C (the work by Chawla, *et al.*)² to 1400 °C (this work) in CNFs both obtained from undrawn precursors does not lead to any evident change in graphitic structural alignment. This is expected, as increasing the carbonization temperature can only facilitate the growth of the graphitic content, and it offers no effective mechanism to improve alignment. Compared to CNFs from another study (no precursor hot-drawing)¹¹ which were carbonized at 800 °C, our CNFs which were obtained from undrawn precursors have slightly higher graphitic alignment (lower FWHM) likely due to the different electrospinning parameters used which affects the microstructure of the precursor, thereby properties of CNFs, while precursor hot-drawing in this work leads to significantly narrower (002) arc, Figure 4(b).

Moreover, Ramachandramoorthy, *et al*¹⁷ successfully improved the alignment of graphitic structure by applying constraining forces during carbonization at 800 °C, which effectively improved mechanical performance of CNF. However, ladder structure of stabilized cyclic PAN chains are relatively rigid. In comparison, engineering the microstructure of precursor polymer nanofibers in its rubbery state (above T_g - the present study) is likely a more convenient path to align the polymer chain due to the much higher mobility of polymer chains.

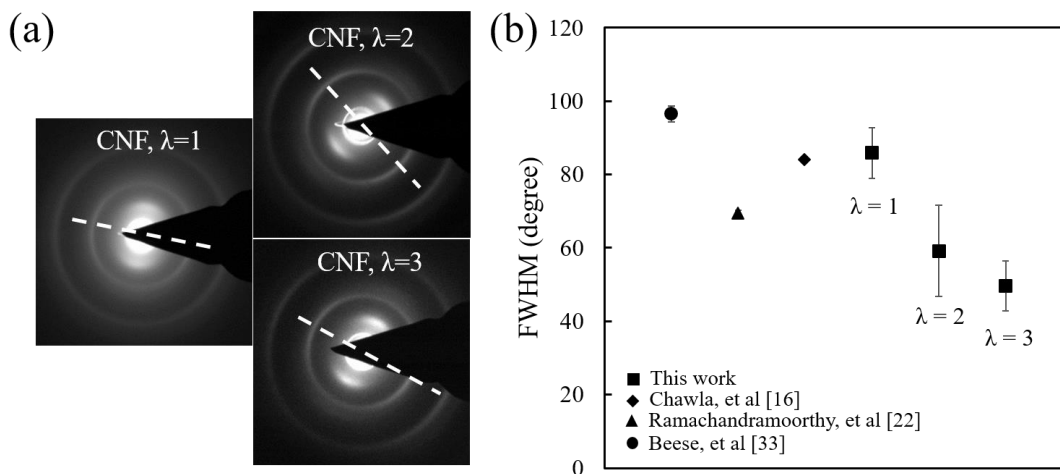


Figure 4. (a) SAED pattern of CNFs with different hot-drawing ratios with dash line showing direction of CNF and (b) FWHM of (002) arc in SAED pattern of CNFs in this work comparing with CNFs from other researches^{16,22,33}.

Mechanical properties of individual CNF: The mechanical properties of individual CNF with different hot-drawing ratios, carbonized at 1400 °C, were characterized by nano-mechanical tension tests under optical microscope. The testing method has been thoroughly discussed in a previous paper². The failure position of individual CNF fixed on MEMS device after testing is shown in Fig.7(a,b), which shows a near circular shape cross-section. As shown in Fig.5(a,c), the strength and modulus of as-electrospun CNFs ($\lambda = 1$) obtained at a carbonization temperature of 1400 °C is 3.7 ± 0.6 GPa and 138 ± 28 GPa, respectively, which are consistent with the previous result from Arshad's work¹⁰. By comparing the mechanical properties of CNFs carbonized at 1400 °C with those fabricated at 1100 °C² it becomes evident that increasing the carbonization temperature effectively improve the mechanical properties of CNF¹⁰. The increased carbonization temperature leads to about 100% and 13% improvement in strength and modulus, respectively, in as-electrospun CNFs (no precursor hot-drawing). The improved mechanical performance is due to reduced defect density (more graphitization) and enlarged crystalline size (both width and thickness) in CNFs formed at higher carbonization temperature.

Moreover, by increasing the precursor hot-drawing ratio, there is an evident and nearly monotonic increase in strength and modulus of CNFs, Figure 5(a) and (b). This is in line with the microstructural analysis of CNFs presented in the previous sections which pointed to a reduced defect density and increased alignment of graphitic structures in CNFs as a result of precursor hot-drawing.

The strength and modulus of CNFs obtained with $\lambda=3$ is on average 6.3 ± 0.8 GPa and 217 ± 44 GPa, which is 70% and 57% higher than the as-electrospun CNFs (no precursor hot-drawing)¹⁰. Our measured strength and modulus of electrospun CNFs is the highest reported for CNFs which are fabricated by carbonizing PAN homopolymers, Figure 5(c) and (d). The strength of CNFs developed in this work is ~55% higher than CFs based on gel-spun PAN homo-polymer³¹. Here we have excluded the reports which are based on PAN copolymers to better elucidate the effect of precursor hot-drawing combined with

carbonization at 1400°C on mechanics of CNFs. However, we would like to note that the inclusion of comonomers which are less polar than acrylonitrile (such as MAA) can facilitate hot-drawing induced chain alignment and thus graphitic alignment. Interested readers may refer to, for instance ^{8,35}.

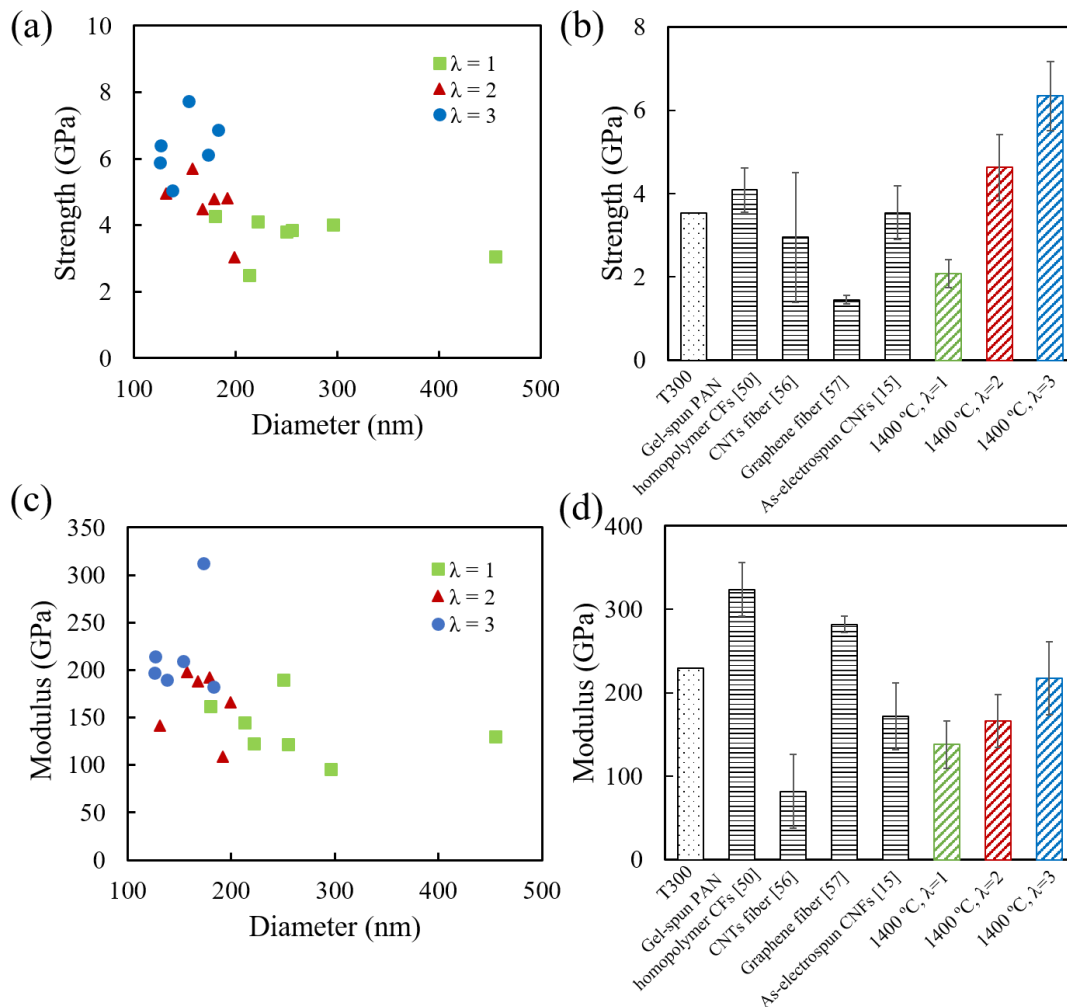


Figure 5. ((a) Tensile strength and (b) modulus of CNFs with different hot-drawings with different diameters obtained in this study. The average values of strength and modulus of our CNFs is compared with (c) modulus and (d) strength of representative high-performance continuous nanofibers based graphitic materials ^{15,50,56,57} and one commonly used commercial CF (T300).

The mechanical properties of CNF in this work are also compares favorably with those of other high performance fibers which are based on graphitic materials, such as VGCNF ³⁶, CNTs fiber ³⁷ and graphene fiber ^{38,39}. The average tensile strength of CNF with $\lambda=3$ is more than double and three times the highest reported values for the strength of CNTs and graphene fiber/yarns, respectively.

In addition to remarkable strength, the rather large ductility in our CNFs is also interesting. The averaged failure strain of hot-drawn CNF with $\lambda=3$ is $3.0\pm 0.7\%$. Compared with CFs made of PAN homopolymer ($1.25\pm 0.15\%$) ³¹, there is a 140% increase in the failure strain. This large failure strain of electrospun CNFs has also been observed by other researchers ^{2,11}.

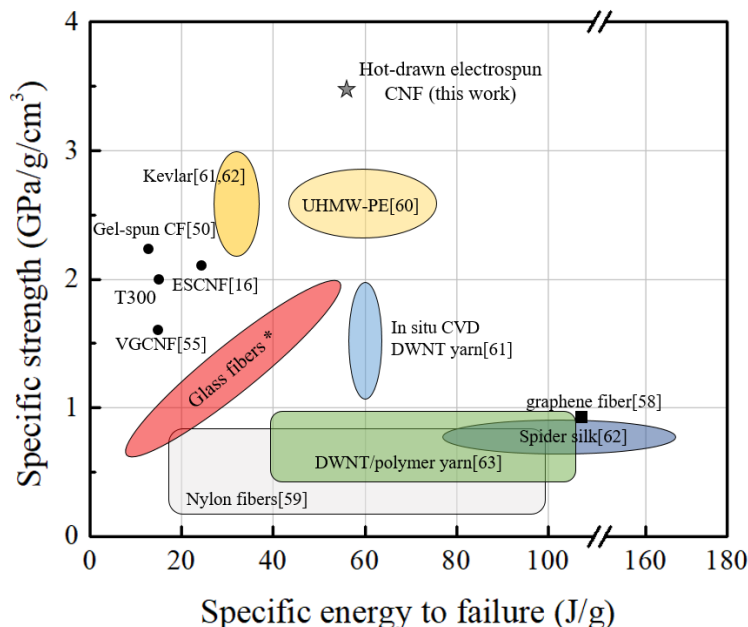


Figure 6. Comparison between CNFs and other high-performance engineering materials or fibers for their specific strength and specific energy to failure, with the star showing properties of hot-drawn CNFs obtained in this work (* The data for glass fibers is obtained from www.AGY.com.)^{16,50,55,58-63}

The combination of high specific strength and ductility leads to remarkably high energy to failure (per unit mass), as shown in Figure 6. The combination of high specific strength and energy to failure is an essential requirement for advanced fibers. As shown in Fig.6, the combination of high specific strength and energy to failure is the highest of all CF/CNF developed up to date based on PAN homopolymer. Comparing with popular commercial CFs (such as T-300), there is 80% increase in the specific strength and 267% improvement in specific energy to failure. Moreover, while the obtained specific energy to failure (55 ± 20 J/g) of CNF is comparable to some super tough fibers^{40,41}, such as Kevlar (36-78 J/g)^{42,43}, DWNTs/polymer fiber (100 J/g)⁴⁴, spider silk (165 J/g)⁴³, the specific strength of hot-drawn electrospun CNF is much higher than all these materials, making them a suitable candidate for applications which call for high strength and flaw-tolerance, such as aerospace fields.

Active failure mechanism of hot-drawn CNF and potential cause of large ductility: Since the ductility of CNFs in the present study and a few others^{2,11} is significantly larger than most of carbonized polymers such as carbon fibers, the high toughness and ductility of CNFs is explained in this section by considering the peculiar microstructural features of CNFs, as studied via TEM imaging.

A TEM image of the fracture surface of an electrospun CNF is shown in Figure 7(d). As shown in the figure, the turbostratic domains are partially aligned, but more importantly they appear to be surrounded and dispersed within a *matrix* of amorphous carbon. Moreover, there is no apparent variation of the alignment or concentration of TB domains in the radial direction. A similar microstructure was also observed by other researcher¹⁰. While the external loading acting along the axis of the CNF favors a crack propagation in the radial direction, *i.e.*, normal to the plane of the maximum tensile stress, the locally heterogeneous microstructure of CNFs offers alternative and more energetically favorable paths within the weaker phase (amorphous matrix) and/or along the matrix interface with the *fillers* (turbostratic domains), as evident in the TEM images. For instance, zone I in Figure 7(d) shows an instance in which the crack has propagated along the basal plane of a misoriented turbostratic domains. The graphene layers are overdrawn by white line for enhanced visibility. The TEM image of the fracture surface alone does not reveal whether the crack has propagated through the domain by exfoliating the domain in the *c*-direction (“opening” the

domain), or has simply moved along the interface of the turbostratic domains with the amorphous matrix surrounding it. Another interesting fracture site is shown in zone II, which is a turbostratic domain aligned with the fiber axis. The length of this domain is comparable to the interior domains observed in the same image. Therefore, the crack has likely propagated around the domain instead of breaking it into smaller domains. The tendency of the crack to move around the rather uniformly distributed turbostratic domains, instead of breaking through them, reflects the strength of the domains.

As a result of that, the crack is forced to follow the orientation of the turbostratic domains. Thus, a highly tortuous crack path will form, increasing the energy required to completely fail the CNFs. The formation of noncritical microcracks (i.e., microcracks that were arrested) within CNF during tensile testing has also been alluded to in an earlier publication²⁵ in which the electrical resistivity of CNFs were monitored in response to cyclic loading with an increasing amplitude. There, we observed a permanent increase in the resistance of CNFs and the by the appearance of ‘fictitious piezoresistivity’⁴⁵ in them after the peak of the strain passed ~1%. This result further confirms the previous analysis that the special heterogeneous microstructure of CNF effectively prevents the crack propagation, therefore considerably improve the energy-to-failure of the CNF.

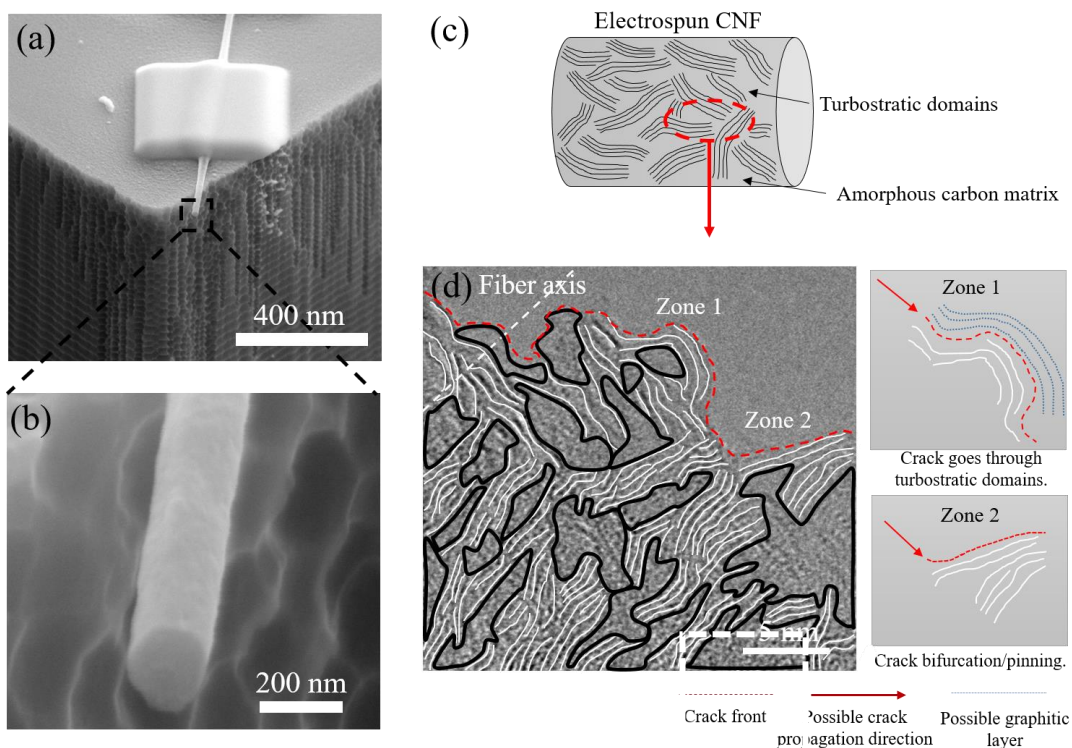


Figure 7. (a, b) SEM image of the failure position in single CNF after testing, (c) schematic diagram of microstructure in CNF showing randomly distributed graphitic domains in amorphous carbon matrix, and (d) TEM image of CNF fracture surface and schematic diagrams describing the possible failure mechanism in electrospun CNF with white lines indicating the graphitic layer in turbostratic domains and black lines showing interface between turbostratic domain and amorphous carbon matrix. (The schematic diagram is not to scale).

The aforementioned mechanism of toughening in a heterogeneous structure of CNF resembles the toughening mechanisms in nanocomposites, such as graphite nano-platelets (GNP) or thermally reduced graphene oxide (TRGO) within epoxy matrix nanocomposite⁴⁶⁻⁴⁹. The major toughening mechanism in all these cases are crack pinning and deflection.

The microstructure of CNFs can be contrasted with that of CFs. While the CNFs can be described as a composite of partially aligned turbostratic domains within an amorphous matrix, the microstructure of CFs is often described as an intertwined network of “interlinked layer planes” of turbostratic domains^{50,51}. The classical Reynolds and Sharp mechanism of tensile failure in CFs suggests that the shear strain energy is sufficient to induce basal-plane rupture in the misorientated crystallite, and the crack will propagate through the adjacent layer planes in CFs³⁴. This fracture mechanism is promoted by the nearly continuous turbostratic domains, or significantly longer domains (along their basal planes) in CFs compared to CNFs. This is in contrast to the fracture mechanism observed in CNFs in which the crack will not break the turbostratic domains, but instead the crack will propagate around them. Therefore, CFs with nearly continuous turbostratic domains can absorb less energy per unit volume and will fail at lower strains compared to CNFs.

The formation of the nearly continuous, interconnected and interlinked turbostratic domains in CFs requires a considerable degree of domain alignment and packing, which is more readily achievable in CFs (compared to CNFs) due to the higher chain alignment in their precursors (for instance, see Table 1). As such, in CNFs with hot-drawing ratio of $\lambda = 3$, the crystallite size is about 1.3 nm, which is comparable to the commercial CFs (T300 with 1300-1400°C carbonization), gel-spun CFs based on PAN homopolymer (1200 °C carbonization)⁵² and copolymer (1450 °C carbonization)⁸, while the CNFs have significantly lower Herman orientation factor of the graphitic domains.

Table 2. Structural parameters comparison of CNFs with different hot-drawing ratios and CFs in micro-size^{31,71}.

Fiber types	Diameter(μm)	f_{002} *	FWHM ₀₀₂ (degree)	L_{002} (nm)**
CNF, $\lambda = 1$ (this work)	0.27	0.44	71.5	1.15
CNF, $\lambda = 2$ (this work)	0.17	0.50	52.8	1.20
CNF, $\lambda = 3$ (this work)	0.15	0.52	47.5	1.27

CFs from gel-spun PAN homopolymer [71]	1	0.73	37.3	1.3
CFs from gel-spun PAN copolymer [31]	5	N/A	23.1	1.9
T300	7	N/A	31.9	1.5

* f_{002} is Herman’s orientation factor of graphitic crystallite in CNF/CF

** L_{002} is crystallite size perpendicular to (002) plane in CNF/CF

Other factors may also contribute to the lower ductility of CFs compared to CNFs. For instance, the microstructure of PAN-based CFs is typically described as a skin-core structure, originated from the insufficient stabilization reaction in core zone. Comparing to the more randomly orientated turbostratic domains in the core, highly aligned and less defective graphitic structure form in the skin of CF during the fabrication process⁵⁰. This is in contrast to CNFs in which by downsizing the precursor fiber diameter to sub-micron scale, the radial inhomogeneity is effectively eliminated^{53,54}. The radial inhomogeneity in CFs can lead to the formation of microcracks along the interface between skin and core due to thermal strains developed during processing, further lowering the ductility of the fibers. Moreover, the relatively smooth surface of electrospun CNFs is also considered as one of the reason for its high potential strength and failure strain⁵⁴.

Conclusions of this section

We studied the mechanical properties of CNFs obtained by carbonization of electrospun polyacrylonitrile (PAN) precursors. The main microstructural parameters studied were precursor chain alignment achieved via hot-drawing and degree of graphitization controlled by adjusting the carbonization temperature. We limited the draw ratio to 3 to avoid drawing induced defects in the precursors. Moreover, the carbonization temperature was limited to 1400°C to limit the size of the turbostratic domains and strength compromising interactions between fully grown domains. The combination of Raman spectrum and WAXD studies on CNFs demonstrates the effective improvement of graphitic structure within CNF, including the in plane and out of plane growth of the graphitic domains, increased graphitic domains alignment along the fiber axis with both increased precursor chain alignment and carbonization temperature.

Based on the nano-mechanical tests of individual CNF, hot-drawing the precursors to draw ratio of ~3 led to considerable increase in strength and modulus of CNFs respectively by ~70% and 57% to 6.3 ± 0.8 GPa and 217 ± 44 GPa. The strength of the hot-drawn electrospun CNF is the largest value achieved among similar materials. Apart from the high strength, the combination of high specific strength and energy-to-failure of CNF is higher than all CNF/CF developed up to now. The energy-to-failure of the CNFs and their ductility is more than twice the corresponding value of the CFs. This was attributed to the peculiar microstructure of the CNFs, a nearly homogenous composite of partially aligned turbostratic domains within the matrix of amorphous carbon, in contrast to CFs with nearly continuous turbostratic domains. The distributed domains in CNFs allow for significant crack deflection and pinning as a means to enhance energy-to-failure.

4.2. Effect of graphitic templating on Mechanics of carbon nanofibers

Graphitic nanoparticles such as CNTs can act as templates within carbonized structures promoting the formation of highly-ordered graphitic (HOG) microstructures. However, to this day, the mechanics of HOG in carbonized structures has been elusive. Moreover, it is not clear whether the formation of HOG can be used to develop stronger nanostructures, or on the contrary, factors such as elastic mismatch between HOG and the rest of the carbonized structures can lead to premature failure due to stress concentration. In this work, the templating effect of functionalized single-walled CNTs in carbon nanofibers (CNFs) and its influence on the microstructure and mechanical properties of hybrid CNFs are studied. To improve the alignment of CNTs and polymer chains, and packing density of chain on surface of CNTs, the as-fabricated precursor nanofibers were subjected to hot-drawing. The correlation between the microstructure of precursor nanofibers and CNFs revealed the crucial effect of chain alignment in the precursor on defect density in CNFs, and thus their mechanical properties. The average tensile strength and modulus of hybrid CNFs with properly engineered HOG microstructure was measured to be 7.63 and 268 GPa, respectively, which are the highest value reported up to date, among similar types of materials. Through continuum models describing the mechanics of CNFs and indirect comparison with experiments, the existence and evolution of the high-performance HOG around the CNTs and its reinforcing effect on the overall mechanical property of CNF were thoroughly discussed, revealing the significance of factors which affect strength of CNFs when HOG is formed. This work for the first time sheds light on the mechanics of the HOG layers in carbonized nanostructures, which is crucial to develop high-performance 1-D hybrid graphitic nanostructure.

Experimental Section

Fabrication of hot-drawn CNF/f-SWNTs nanofiber: Polyacrylonitrile (PAN)/f-SWNTs precursor nanofiber ribbon was fabricated via electrospinning on a rotary target as discussed in previous publication¹. Templating graphitization was pursued by adding functionalized single-walled carbon nanotubes (f-SWNTs) to precursor nanofibers. The f-SWNTs, from Carbon Solutions Inc., contained 1-3 atomic% carboxylic acid groups on surface to facilitate the dispersion of CNTs within PAN nanofibers. To process CNF precursors, f-SWNTs were first dispersed in dimethylformamide (DMF) solvent (from Sigma–Aldrich) via ultrasonication for 4 hours to achieve visually homogeneous solution. Then, polyacrylonitrile (PAN) powder ($M_w = 150,000$ g/mol, from Sigma–Aldrich) was dissolved in f-SWNTs/DMF solution to obtain 10 wt.% PAN/f-SWNTs/DMF solution. The concentration of f-SWNTs was controlled to be 0.5 wt.% of PAN, which roughly corresponds to 1 wt.% of CNTs in CNFs. Electrospinning process was performed at a voltage and distance of 16 kV and 20 cm, and the flow rate of polymer solution was set to ~0.5 ml/hr to obtain a stable jet with a rotating target at ~5.7 m/s peak-up velocity. The PAN/f-SWNTs nanofiber ribbons then were drawn to $\lambda = 3$ (λ , hot-drawing ratio = final length/initial length of ribbon) by applying an engineering stress of ~19 MPa in an oven at a temperature of 135°C to induce chain alignment². The hot-drawn nanofiber ribbons were stabilized at 290 °C for 2 hours in air with 5 MPa constraint stress. Carbonization of stabilized PAN/f-SWNTs nanofibers was carried out in tube furnace (MTI, GSL-1700x) at 1400 °C for 2 hours under inert gas (N_2) environment. In addition, CNFs without CNTs and/or without any precursor hot-drawing was synthesized as benchmarks.

Microstructural characterization and mechanical testing of nanofibers: FEI Quanta 600 FE-SEM was used to study the surface of PAN nanofibers and CNFs. The semi-crystalline structure of PAN nanofibers and CNFs were also studied by collecting X-ray diffraction spectra of nanofiber ribbons via GADDS BRUKER-AXS MWPC 3-third circle X-ray Diffractometer ($CuK\alpha$, wavelength of 0.154 nm). Scherrer's equation ($K = 0.89$) was used to estimate the crystallite size within PAN and CNFs nanofiber⁶. The PAN nanofiber crystallinity was calculated by dividing the area under deconvoluted crystalline peaks by the total area, including both crystalline and amorphous peaks by using Lorentzian fitting in Origin 9.0³. The PAN crystallite orientation within the nanofiber was obtained based on the wide-angle X-ray diffraction (WAXD) pattern and azimuthal scan of the diffraction peak at $2\theta \sim 17^\circ$ ⁷. Graphitic crystallite orientation of CNFs was obtained from the azimuthal scan at $2\theta = 25^\circ$ ⁵⁵. Herman's orientation factor was also

calculated as described elsewhere⁵⁶. Horiba Jobin-Yvon LabRam Raman Confocal Microscope with a He-Ne laser (633nm) was used to analyze the graphitic structure of CNFs. The width (L_a) of the graphitic crystallites (along their basal planes) in CNFs was calculated based on the deconvoluted D- and G- peak area intensity ratio (I_D/I_G)^{27,28}. The measurements were repeated a minimum of three times to ensure repeatability, and the average value of the peak ratios were used to calculate the crystallite width. FEI Tecnai G2 F20 transmission electron microscope (TEM) was used to characterize CNF graphitic structure.

MEMS-based nano-mechanical testing platform was used to measure the mechanical performance of individual CNF/f-SWNTs in tension. The MEMS device used in this work and the whole testing process were thoroughly discussed in our previous work². A minimum of six tests were performed for each fabrication condition and the average mechanical properties and standard deviations were reported.

Results and Discussion

As shown in our previous work¹, adding pristine (*i.e.*, unfunctionalized with low defect density) SWNTs to electrospun PAN nanofibers especially after the nanofibers are drawn at temperature above its glass transition temperature to draw ratio of as high as 4 leads to the formation of extended chain structure of polymer chains, *i.e.*, polymer interphase, on the surface of SWNTs²⁰. Moreover, Prior studies also show that the carbonization of PAN with CNT inclusions can lead to the formation of highly ordered graphitic (HOG) regions around CNTs^{51,57}. However, the relatively low concentration of pristine SWNTs (0.1-0.2 wt.%) that can be well-dispersed in electrospun PAN nanofiber without considerable agglomeration, significantly restricts performance improvement in PAN nanofibers and CNFs. For instance, the highest mechanical strength and modulus in PAN/CNTs (pristine CNTs) hybrid nanofibers is achieved at 0.1 wt.% SWNTs, and further increasing the concentration leads to CNTs agglomerations, serving as defects in precursors and CNFs¹. Therefore, to overcome this problem, functionalized SWNTs with carboxylic acid groups were used in this work to better disperse CNTs within PAN-DMF solution and to fabricate hybrid nanofibers with higher CNT content. The carboxyl groups significantly enhanced the dispersion of f-SWNTs in DMF and also PAN/f-SWNTs/DMF solution, demanding significantly shorter ultrasonication times (~4 hours), compared to pristine SWNTs (24 hours), to achieve visually homogeneous solution.

To evaluate the quality of dispersion of CNTs within the PAN nanofibers, we studied the mechanical properties of hybrid precursor nanofiber ribbons. While adding 0.5 wt.% of pristine SWNTs to PAN in a previous work¹ reduced the strength and modulus of the polymer nanofibers compared to the neat polymer nanofiber due to CNTs agglomeration, the mechanical testing of polymer nanofiber ribbons with $\lambda = 1$ and 3 in this work, shows that adding 0.5 wt.% f-SWNTs effectively improves the strength and modulus of hybrid nanofiber ribbons. Direct evidence of the formation of HO polymer interphase wrapped protruded f-SWNTs, likely in the form of extended chains, are also found at the broken surfaces of hot-drawn PAN/f-SWNTs nanofiber. In the following sections, the microstructure of PAN/f-SWNTs with different hot-drawing ratios are analyzed.

Microstructure of PAN/f-SWNTs nanofiber: The semi-crystalline structure of as-electrospun and hot-drawn PAN nanofibers were studied via X-ray diffraction. There is no evident crystalline peak in X-ray diffraction patterns of as-electrospun PAN and PAN/f-SWNTs nanofibers prior to hot-drawing (results not shown in the figure). That is due to the fast evaporation of solvent during electrospinning, which “freezes” the chains prior to considerable chain alignment is achieved¹. However, as a result of the hot-drawing to $\lambda = 3$, a crystalline peak of PAN emerges at a diffraction angle of 17° in both pure PAN and PAN/f-SWNTs precursors, Figure 8 (a). The degree of crystallinity in pure PAN reaches ~31% (orientation-induced crystallization facilitated via hot-drawing). The degree of crystallinity of hot-drawn PAN/f-SWNTs nanofibers is considerably higher, ~38%, indicating the role of CNTs as crystallization nucleating agent of PAN, which is consistent with previous results with PAN^{1,16,58} and other polymer matrix^{59,60}. However, despite higher degree of crystallinity in PAN nanofibers with CNTs inclusions, PAN crystallites formed in hot-drawn PAN/f-SWNTs, are slightly smaller than the ones formed in pure PAN. It is likely that the growth

of PAN crystallites around each CNT is partly suppressed by the neighboring CNTs, thus, preventing the growth of a longer range order that can grow around an isolated CNTs surrounded by PAN chains.

More information about the crystalline structure of PAN was obtained by investigating their WAXD 2D patterns, shown in Figure 9. As mentioned earlier in this section, both the as-electrospun PAN and PAN/f-SWNTs nanofibers (prior to hot-drawing) are nearly completely amorphous. However, the symmetric arcs that appear in the WAXD of both samples is a clear indication of not only the formation of crystallites, but also the preferential alignment of PAN chains within the crystallites along the fiber axis. The preferential orientation of PAN crystallites in both types of samples after hot-drawing is the same within the experimental error, evident in the measured Herman's orientation factors, 0.70 and 0.69, for pure PAN and PAN/f-SWNTs, respectively.

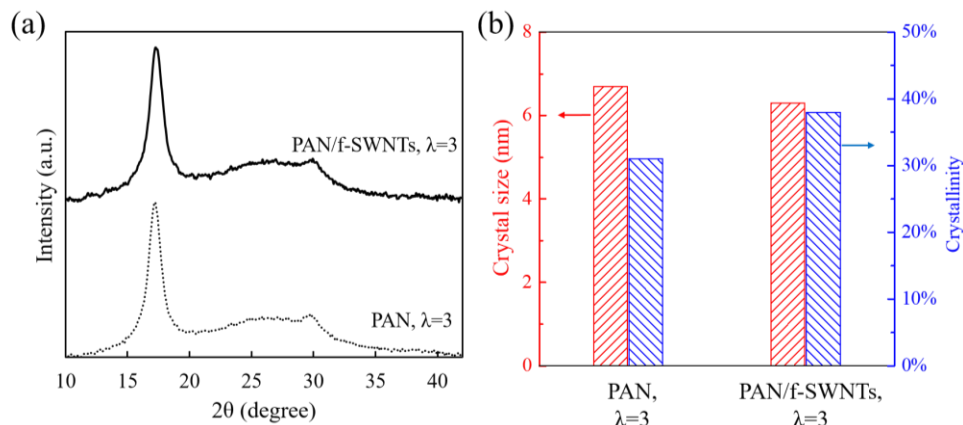


Figure 8. (a) WAXD patterns and (b) calculated crystallinity and crystal size of PAN and PAN/f-SWNTs nanofibers with $\lambda=3$.

Microstructure of CNF/f-SWNTs nanofiber: The as-electrospun and hot-drawn PAN and hybrid nanofibers were stabilized under 5 MPa constraint stress to maintain chain alignment, and carbonized to fabricate CNF/f-SWNTs nanofiber. The I_D/I_G ratio of samples and average width of the graphitic crystallites (L_a) were obtained from Raman spectrum, as shown in Figure 10. For comparison, the Raman spectra of pure CNFs (obtained by carbonizing pure PAN with no CNTs) are also presented in Figure 10.

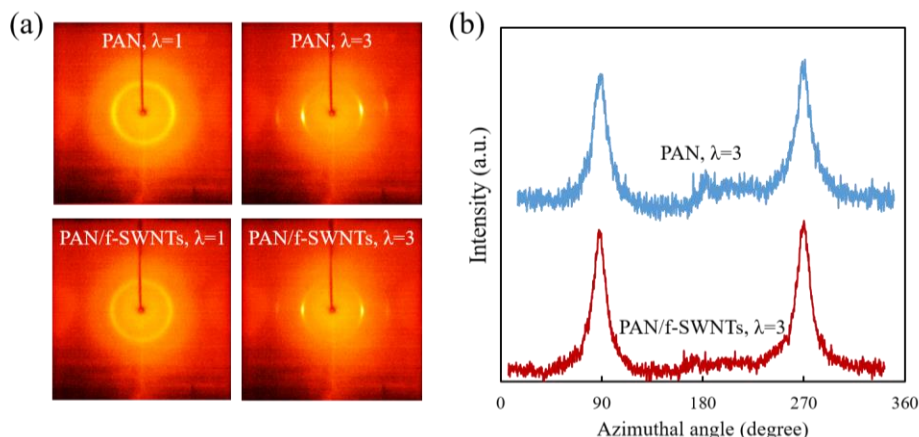


Figure 9. (a) WAXD 2D pattern and (b) azimuthal intensity scan of PAN and PAN/f-SWNTs nanofibers with different hot-drawing ratios.

In both cases, pure PAN and PAN/f-SWNTs precursors, hot-drawing leads to a slight reduction in I_D/I_G by ~10%. Thus, it is clear that the chains in hot-drawn precursors can more readily form graphitic domains upon carbonization. This is expected since the hot-drawing will enhance the chain packing, thus, it will facilitate the merger of the chains during thermal stabilization and carbonization. Moreover, the SWNTs can act as templates for the graphitic structures as they emerge out of carbonizing PAN. The major change in the I_D/I_G ratio, however, comes as a result of adding CNTs to the precursor. The investigation of the I_D/I_G in samples with similar precursor hot-drawing ratio can further allude to the contribution of CNTs in inducing/mitigating defects in CNFs. It is to be noted that part of the G- and D-peak intensities in Raman spectrum of CNF/CNTs comes directly from the embedded CNTs, which has much lower I_D/I_G ratio (~0.13) than pure CNFs (~4). Therefore, the decrease in I_D/I_G ratio from as-electrospun CNFs to CNF/f-SWNTs should not exclusively be attributed to the improvement in graphitic structure from templating effect, although the low concentration of CNTs (~ 1 wt.%) lowers the significance of this effect.

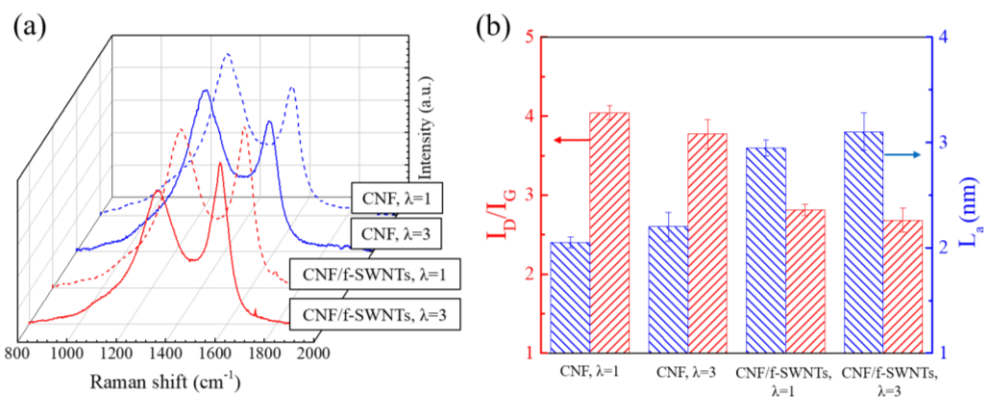


Figure 10. (a) Raman spectrum and (b) calculated I_D/I_G ratio and crystal size (L_a) of CNF and CNF/f-SWNTs with different hot-drawing ratios.

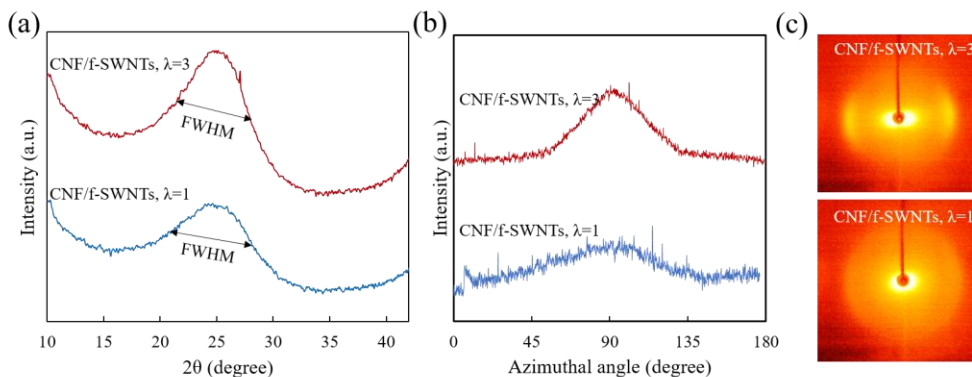


Figure 11. (a) WAXD patterns, (b) intensity azimuthal scan and (c) 2D patterns of CNF/f-SWNTs with different hot-drawing ratios.

The graphitic structure of CNF/f-SWNTs was further analyzed by using WAXD, as shown in Figure 11. From the WAXD patterns, the Herman's orientation factor and crystalline thickness (L_c) can be estimated as discussed in the Experimental section. These structural parameters are calculated for CNFs as a function of the precursor hot-drawing ratio and CNTs content, and listed in Table 1. Prior to precursor hot-drawing, the thickness of the graphitic crystallites in as-electrospun CNF/f-SWNTs is slightly smaller than the crystallite thickness in pure CNFs (1.15 nm vs 1.21 nm.). Moreover, the graphitic structure in pure CNFs has slightly more aligned graphitic structure than CNF/f-SWNTs. The Herman's orientation factor of the

former is $f_{002} = 0.440$ compared to $f_{002} = 0.411$ for the latter. This can be traced back to the adverse effect of CNTs on chain alignment in as-electrospun PAN nanofibers. During the electrospinning process, by adding SWNTs into PAN solution, the increased solution viscosity presents a barrier to jet drawing. Therefore, less molecular alignment is achieved in as-electrospun PAN nanofibers with CNT inclusions¹, leading to reduced graphitic alignment in CNFs.

While in CNFs that are obtained without precursor hot-drawing, the addition of CNTs can adversely affect the graphitic structure, it is interesting to note that the hot-drawing reverses this effect, such that the hot-drawn CNF/f-SWNTs have slightly higher Herman's orientation factor and thicker crystallites compared to hot-drawn pure CNFs. This is in line with the WAXD results on precursors, and it further reinforces the notion that the chain packing and alignment which can be achieved via hot-drawing is required to effectively benefit from the templating effect of CNTs to enhance the graphitic structure of CNFs.

Table 2. Structural parameters of CNF and CNF/f-SWNTs with different hot-drawing ratios.

Nanofiber types	f_{002} *	FWHM ₀₀₂ (degree)	$L_{(002)}$ (nm)**
Pure CNF, $\lambda = 1$	0.440	71.5	1.15
Pure CNF, $\lambda = 3$	0.517	47.3	1.27

CNF/f-SWNTs, $\lambda = 1$	0.411	83.7	1.12
CNF/f-SWNTs, $\lambda = 3$	0.523	45.9	1.33

* f_{002} is Herman's orientation factor of graphitic crystallite in CNFs

** L_{002} is crystallite size perpendicular to (002) plane in CNFs

Mechanical properties of individual CNF/CNTs: Mechanical properties of individual CNF/f-SWNTs hybrid nanofiber were characterized by using the MEMS-based nano-mechanical testing platform, Figure 12 (a). SEM image of a CNF broken in tension using the device and a close-up image of the broken end of a CNF is shown in Figure 12 (b) and (c), respectively. As shown in part (c), protruded f-SWNTs are present at the broken surface of an individual CNF/f-SWNTs nanofiber. The image of the protruded SWNT from the broken ends of CNFs confirms the presence of the CNTs within the gage length of the tested CNFs.

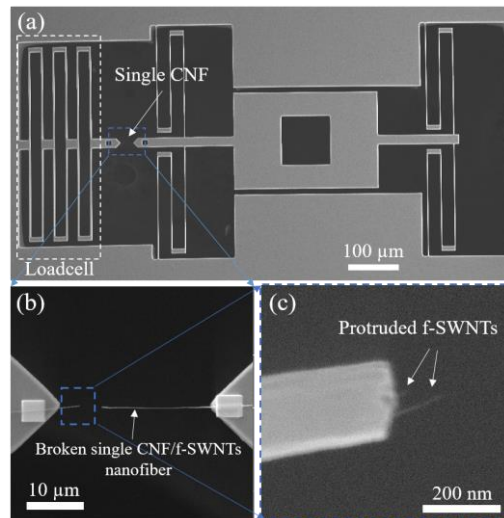


Figure 12. (a) MEMS device used for testing mechanical properties of single CNF/f-SWNTs nanofiber and (b-c) broken surface of CNF/CNTs after testing showing protruded f-SWNTs.

The tensile strength and modulus of CNF/f-SWNTs as a function of the nanofiber diameter are presented in Figure 13 (a,b). Similar to CNFs obtained from monolithic precursors (no CNTs inclusions) ⁶¹, a major improvement in mechanical properties of CNF/f-SWNTs was observed as a result of precursor hot-drawing. The tensile strength of CNF/f-SWNTs increased from 2.41 ± 0.57 GPa for $\lambda=1$ to 7.63 ± 1.72 GPa for $\lambda=3$, *i.e.*, 217% improvement of the average values; meanwhile, the modulus increases from 109 ± 49 GPa to 268 ± 29 GPa, corresponding to 146% improvement in the average value. This outstanding mechanical properties improvement stems from the evident microstructure evolution in the hot-drawn CNF/f-SWNTs hybrid nanofiber, including improved graphitic domains alignment and size and decreased defect density.

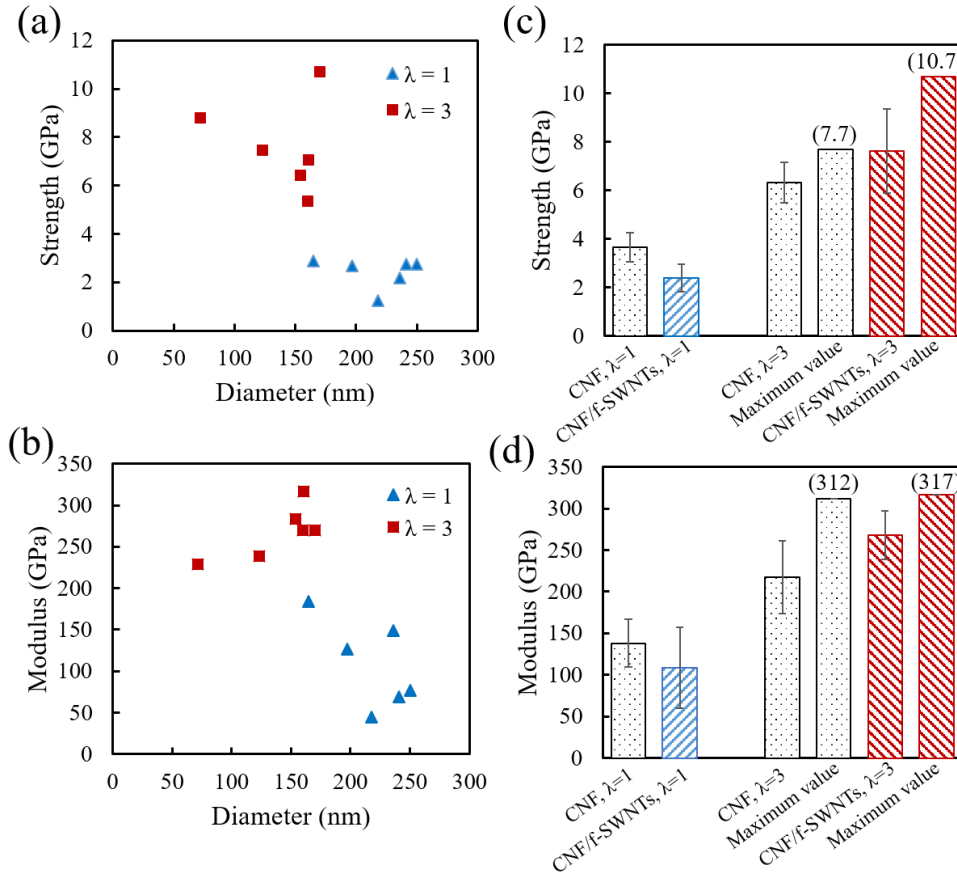


Figure 13. (a) Tensile strength, (b) modulus data versus nanofiber diameter of CNF/f-SWNTs with different hot-drawing ratios, (c) average and maximum strength and (d) modulus data comparison between pure CNF and CNF/f-SWNTs with different hot-drawing ratios.

It is highly illustrative to compare the mechanical properties of CNF/f-SWNTs with those of pure CNFs, especially when considering various cases of precursor hot-drawing. In CNFs obtained without precursor hot-drawing ($\lambda=1$), the addition of CNTs to the precursor results in a meaningful loss in mechanical properties: The strength and modulus of pure CNFs obtained from monolithic precursors with no CNTs is respectively 52% and 27% higher than the CNFs with CNTs inclusions, Figure 13 (c,d). The loss in tensile strength and modulus, by adding CNTs to CNFs, which is only observed in samples with no precursor hot-drawing, is consistent with the microstructure analysis in previous section. That is, in as-electrospun CNFs, adding CNTs lowers the graphitic crystallite alignment and decrease its size due to increased viscosity during electrospinning process. The reduced chain alignment in as-electrospun PAN/f-SWNTs nanofibers

will lead to a reduced graphitic domains alignment in CNFs and thus decreased tensile strength and modulus.

On the other hand, the presence of CNTs in CNFs that are obtained from precursor hot-drawing ($\lambda=3$) leads to a considerable enhancement in both strength and modulus. The strength of CNFs increases from 6.34 ± 0.83 GPa to 7.63 ± 1.72 GPa and modulus increases from 217 ± 44 GPa to 268 ± 29 GPa, by adding f-SWNTs, corresponding to $\sim 20\%$ and 24% improvement in properties, respectively. This obtained mechanical performance is the largest combination of strength and modulus experimentally realized for CNFs ^{2,10,62} (gauge length $> 25\mu\text{m}$).

Moreover, the difference between the mechanical properties of CNFs obtained from hot-drawn precursors with and without f-SWNTs clearly reflects the contribution of the HOG. In other words, one may estimate the improvement expected in the modulus of CNFs by adding f-SWNTs, if no HOG was formed, based on rule of mixture to be 222 GPa, which is considerably lower than the measured modulus of CNF/f-SWNTs (268 GPa). However, as pointed out earlier, this effect is limited to hybrid CNFs from hot-drawn precursors. Therefore, applying precursor hot-drawing is not only important for aligning the graphitic domains within pure CNFs therefore improving its mechanical performance ², but also crucial to exert the templating effect of CNTs to facilitate the formation of HOG phase in CNFs matrix to further improve its properties. In other words, improvement in chain alignment in both pure PAN and PAN/f-SWNTs will promote the formation of graphitic structures as shown by WAXD on CNFs. The lower relative improvement in strength can partly be explained by the stress concentration that can develop in CNFs around embedded CNTs, especially CNTs agglomerations, due to elastic mismatch between the CNTs and its surrounding, which will be thoroughly discussed in the next section.

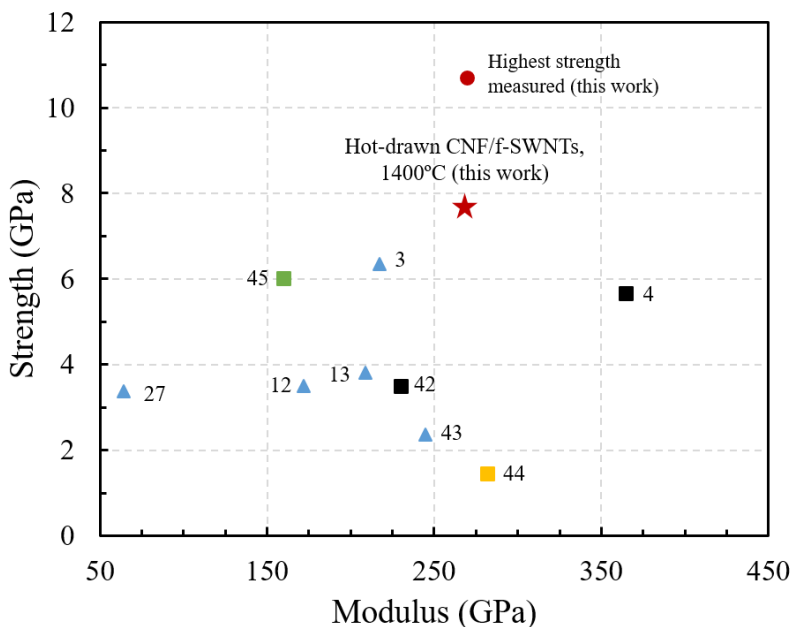


Figure 14. Mechanical properties comparison between CNFs and other high-performance fibers based on graphitic materials (gauge length $> 25\mu\text{m}$) including, electrospun CNFs^{3,12,13}, GT CFs 4, CNF/GNR²⁷, T300 CFs⁴², VGCNFs⁴³, graphene fiber⁴⁴ and CNTs fiber (high strength peak)⁴⁵, with the star mark indicates the average tensile strength and modulus of CNF/f-SWNTs with $\lambda=3$.

The CNFs obtained from pyrolyzing electrospun polymeric precursors belong to a large category of graphitic nanomaterials and strands some of which are shown in Figure 14. Thus, it is illustrative to compare the results obtained here with those of existing literature. For instance, the hot-drawn CNF/f-SWNTs

outperform many other types of high-performance nanofiber/fibers based on graphitic structures, such as GT CFs⁵⁵, T300 CFs⁶³, VGCNFs³⁶, CNF/GNR⁶², graphene fiber⁶⁴, CNTs fiber³⁷ and, in terms of strength and modulus. Moreover, compared to ultra-stiff graphene fibers based on ultra-high temperature annealing (3000 °C)⁶⁴, the strength of CNF/f-SWNTs is 426% higher with similar modulus. Even comparing to the strongest CNTs fibers up to date³⁷, the average strength and modulus of CNF/f-SWNTs are 27% and 68% higher than the high strength peak cases. Moreover, the tensile strength of CNF/f-SWNTs is 70% larger than the gel-spun CFs based on PAN homopolymer (4.09 GPa)³¹. As shown in the previous works², hot-drawn CNFs shows better radial structural homogeneity and lower defect density than the other types of high-performance fibers such as carbon fibers.

The schematic diagrams in Figure 15 (a) shows the microstructures modification of CNFs through applying different processing approaches. For the as-electrospun CNFs, the randomly orientated turbostratic domains (defective graphitic structures) distribute within the amorphous carbon matrix. The relatively low graphitic alignment in it evidently limits its achievable mechanical property¹⁰. Introducing CNTs to promote the formation of HOG and applying precursor hot-drawing to increase graphitic alignment can on the other hand improve mechanical properties such as strength and modulus.

In as-electrospun CNFs, the effects of microstructure evolution including the formation of HOG on mechanics improvement is compromised by the reduced chain due to increased viscosity of the solution. Moreover, the misalignment of CNTs within the CNFs restricted their reinforcing effect on the hybrid nanofiber. On the other hand, when f-SWNTs are added to the precursor nanofiber and they are hot-drawn, during the hot-drawing process, the external applied stress include the aligning of polymer chain, with high chain mobility along the fiber axis. In this process, the CNTs also get aligned along the fiber axis with polymer chain tightly packing around its surface. Then, after the stabilization and carbonization process, highly ordered graphitic interphase is obtained on the surface of CNTs. The existence of HOG on the surface of SWNTs is demonstrated by the direct TEM observation, shown in Figure 15 (b). The measured thickness of HOG interphase is about 3 nm from the TEM image is in the same range of the thickness of HO polymer interphase, about 4 nm in PAN/SWNTs from previous work¹. Moreover, the obtained interphase in hot-drawn samples is thicker, demonstrated by the enlarged crystallite size in WAXD results, suggesting that the templating effect was promoted by the hot-drawing. All these effects contribute to the overall mechanical property improvement of CNFs, which makes the CNF/f-SWNTs to achieve the highest combination of tensile strength and modulus.

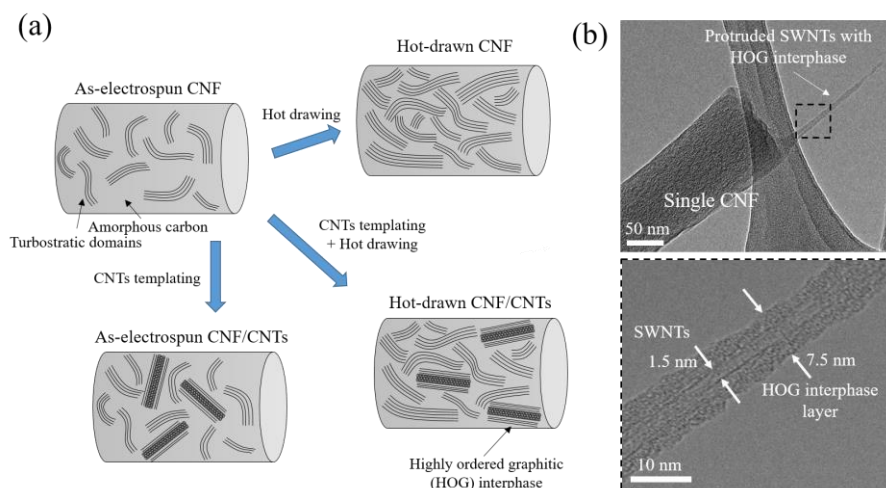


Figure 15. (a) Schematic diagrams of different microstructure of CNF and CNF/f-SWNTs from different fabrication methods and (b) TEM image showing HOG interphase wrapped protruded f-SWNTs at broken surface of CNFs.

FEA modeling of CNF/SWNTs hybrid nanofiber: Although applying the simple rule of mixture could effectively predict the reinforcement effect of SWNTs and HOG interphase on the modulus of obtained hybrid nanofiber^{52,65,66}, it does not provide any detail about the local stress fields around CNTs which can affect the strength of the CNFs especially in light of the formation of the HOG. To better understand the reinforcing effect of HOG interphase and its influence on the mechanical properties of the whole hybrid nanofiber, finite element analysis (FEA) was employed to simulate the microstructure of the hybrid CNF/SWNT.

The stress distribution within the hybrid nanofiber is studied by using the commercial finite element software package, ABAQUS. The mesh sensitivity analysis was performed to determine the appropriate size of the elements used in FEA. The FEA model considered a building block of the CNF consisting of a CNT surrounded by HOG and carbonized PAN. The size of the building block was adjusted based on the experimental volume fraction of the CNTs inside the CNF. As shown in Figure 16 (a), the microstructure of the nanofiber was simplified as aligned SWNTs wrapped with HOG interphase. Base on the experimentally obtained modulus of pure CNF with the same fabrication conditions, the modulus of matrix CNF is set to be 217 GPa with 0.27 as the Poisson's ratio, the same as CF⁶⁷. For the f-SWNTs, considering the concentration of the carboxylic acid groups on surface of the SWNTs, its modulus is assumed to be 90% of the theoretical modulus, 1 TPa to be 900 GPa⁶⁸. The effect modulus of the hollow cylinder, representing SWNT, was adjusted based on its cross-section area. The diameter of SWNT and approximate thickness of HOG interphase was obtained from TEM image in Figure 15(b), which are 1.5 nm and 3 nm, respectively. The stress distribution within the hybrid nanofiber was obtained after applying 1% strain to the system.

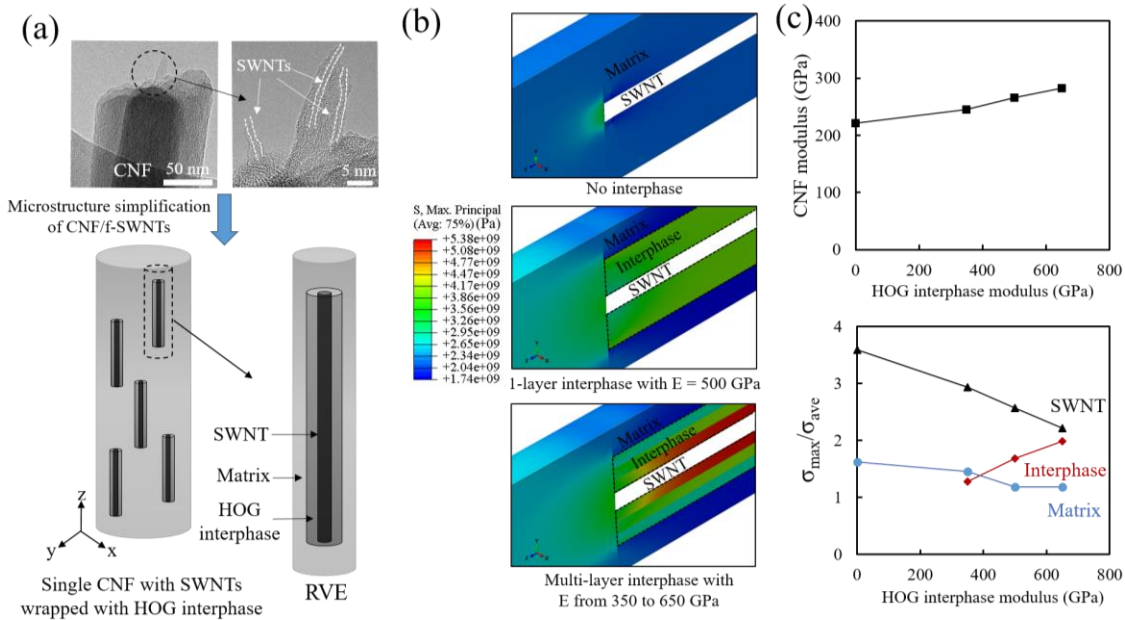


Figure 16. (a) TEM image shows the protruded SWNTs (labelled with white dash line) wrapped with HOG interphase and schematic diagram of CNF hybrid nanofiber showing a CNF embedded in a matrix as a representative volume element (RVE), (b) FEA results showing matrix principal stress distribution within CNF matrix and interphase areas, (c) obtained modulus of CNF and $\sigma_{max}/\sigma_{ave}$ in different phases within CNF with different interphase modulus.

The maximum principle stresses within the matrix and interphase zones in the hybrid nanofiber and the obtained effective modulus and stress concentration in different phases of the hybrid nanofiber with

increasing interphase modulus are shown in Figure 16 (b, c). As shown in Figure 16 (c), by increasing the modulus of HOG interphase, there is a continuous increase in effective modulus of the whole hybrid nanofiber, and the obtained value is consistent with the results from rule of mixture calculation. This analysis can be used to estimate the effective modulus of the interphase. Based on the experimentally obtained modulus of CNFs, which is 268 GPa, the modulus of HOG interphase is approximately to be 500 GPa, which is much higher than the rest of the CNF (the experimentally measured modulus of the pure CNFs, a value of 217 GPa).

To shed light on the reinforcement effect of HOG interphase on strength of CNFs, the maximum principal stress induced stress concentration is used as the indication of the failure stress for whole hybrid nanofiber. When no HOG interphase is considered in the nanofiber, evident stress concentration sites develop at the matrix phase near to the tip of CNTs due to the large modulus mismatch. These stress concentration sites can act as microcrack in CNF, which determines its failure stress. After introducing the strong HOG interphase, the stress concentration within the matrix is effectively reduced, due to the reduced elastic mismatch along all surfaces in the CNF and the largely increased load bearing ability of the HOG interphase. By increasing the modulus of HOG interphase and therefore its load bearing ability, there is an evident decrease in the stress concentration in CNTs and matrix phases. Considering that the strength and modulus of HOG interphase is higher than the matrix CNF, the increased stress concentration factor, from 1.28 to 1.99, within it is unlikely to initiate the failure of the fiber; On the other hand, the stress concentration within matrix is evidently lowered, both of which contribute to the overall tensile strength increase in CNF/f-SWNTs, observed in the previous nano-mechanical tests.

Considering an effective elastic modulus of HOG of 500 GPa, which leads to a favorable matching between the experimentally measured modulus of CNFs and the theoretical values, the stress concentration factor in the HOG interphase with modulus of 500 GPa, is 1.69. Therefore, the failure stress of the unfailed HOG phase attached to CNTs surface has to be on average larger than the product of stress concentration and the average strength of the hybrid CNFs (1.69 times 7.6 GPa, 13 GPa). Therefore, the formation of HOG interphase, possessing superior mechanical properties with modulus of about 500 GPa and strength larger than 13 GPa, effectively improves the mechanical performance of the CNF/f-SWNTs hybrid nanofiber. However, this model is still over-simplified by assuming the interphase layer with homogeneous mechanical properties. In a more realistic interphase, there has to be a nearly continuous property transition from matrix CNF to CNTs, which further lowers the stress concentration factor within the interphase region with lower properties. Figure 16 (b) shows the max principal stress distribution in matrix and interphase regions in CNF with 3-layer interphase condition. It is to be noted that in the actual hybrid nanofiber, there is still some bundles of SWNTs formed, which evidently lowers the overall HOG interphase area, therefore lowers the reinforcing effect of CNTs templating on mechanical properties of the whole CNFs.

Conclusion of this section

In this work, for developing high-mechanical performance 1-D graphitic nanostructure, CNFs reinforced with functionalized single-walled carbon nanotubes (f-SWNTs) were fabricated by applying electrospinning process. The microstructure analysis and mechanical testing of PAN/f-SWNTs indicates relatively homogeneous distribution of CNTs in PAN nanofiber has been achieved, which brings effectively precursor microstructure evolution. Then, the CNF/f-SWNTs were fabricated through applying 1400 °C carbonization, the optimum carbonization temperature for achieving high strength CNFs identified in previous work. The mechanical properties of individual CNF/f-SWNTs were improved to 7.63 and 268 GPa for tensile strength and modulus, respectively, through effectively microstructure evolution, including increased graphitic structure alignment and size and decreased defect density, demonstrated by various characterization methods. The strength and modulus combination of CNF/f-SWNTs is the largest value comparing to all CNFs/CFs developed up to date. Through combining with the experimental results, FEA results demonstrate the effective reinforcement effect of HOG interphase formation on both modulus and strength of the hybrid nanofiber. Based on this study, a facile approach has been developed to effectively

modify the microstructure of the 1-D graphitic nanomaterials, which brings in outstanding mechanical performances improvement and make the CNF/f-SWNTs to be a promising candidate for next-generation high-mechanical performance reinforcement materials in weight-sensitive structural applications.

4.3. Numerical Analysis of Electrical Conduction in Hybrid Nanomaterials

In this section, a comprehensive multi-resolution two-dimensional (2D) resistor network model is developed to analyze the electrical conductivity of hybrid nanomaterials made of insulating matrix with conductive particles such as CNT reinforced nanocomposites and thick film resistors. Unlike existing approaches, our model takes into account the impenetrability of the particles and their random placement within the matrix. Moreover, our model presents a detailed description of intra-particle conductivity via finite element analysis, while the inter-particle conductivity is assumed to be primarily due to electron tunneling. The model is then used to predict the electrical conductivity of electrospun carbon nanofibers as a function of microstructural parameters such as turbostratic domain alignment and aspect ratio.

Model Development

Electrospun CNFs are fabricated via thermal stabilization and carbonization of electrospun polyacrylonitrile (PAN) nanofibers. In this process, PAN chains will first be converted to a ladder-like cyclic structure. Moreover, atoms other than carbon will gradually form volatile species such as ammonia gas which will leave the sample⁶⁹. During carbonization process, turbostratic domains will form in a nucleation and growth process. An example of the turbostratic domains in a CNF is shown in Figure 17(A). These particles will be surrounded by sp^3 carbon matrix and partially carbonized PAN. The turbostratic domains become more and more graphitic as the carbonization time and temperature is increased¹⁰.

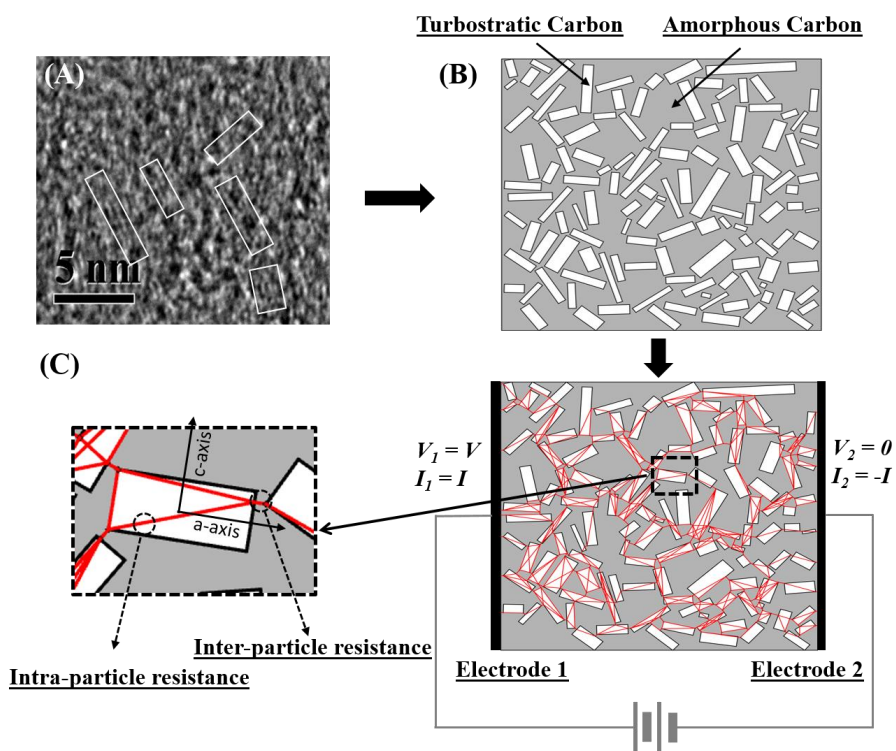


Figure 17. (A) TEM image of CNF with turbostratic carbon outlined in white (B) Simulated structure of the CNF (C) Boundary conditions for calculating CNF conductivity and obtained resistor network with inter-particle and intra-particle resistances.

To estimate the electrical conductivity of CNFs, we modeled the microstructure of CNFs in 2D. Inspired by the fabrication process of CNFs, the microstructure was modeled as conductive particles (turbostratic domains) surrounded by a medium such as amorphous carbon or partially carbonized PAN which was assumed to be nonconductive, Figure 17(A). The particles were considered to be rectangular in 2D, with

the longer dimension representing the in-plane graphitic direction in turbostratic domains (a-axis), and the shorter direction represented the c-axis. The orientation of particles were defined as the angle between the a-axis of each particle and the CNF axis. Particles were grown in steps and in random direction from their randomly positioned nucleation sites. The relative growth rate in the a- and c-axis was controlled to achieve average aspect ratios that are consistent with experimental data. Higher and lower aspect ratio particles were also studied to provide more insight into conductivity in CNFs. The particles were grown until the percolation threshold was reached, at which a conductive path formed within the nanofiber. A comprehensive resistor network model, with both intra- and inter-particles resistance, was thus generated to analyze electrical conductivity of CNF. The conductivity of the whole CNF was then calculated by solving the linear system of equations of Kirchhoff's circuit laws based on the formed resistor network. Two types of resistances are incorporated in the obtained conductive network, intra-particle and inter-particle resistances. Complementary methods, including parallel resistor calculation and finite element analysis, were applied to calculate these two kinds of different resistances, as discussed in following parts. The microstructural generation, calculation of the equivalent resistor values and solving the Kirchhoff's circuit laws were all performed in MATLAB.

Microstructure generation: As is shown in Figure 17(B), the microstructure of CNFs in 2 dimensions is approximated with a hybrid structure, in which the rectangles representing the turbostratic domain randomly distributed in the amorphous carbon matrix (grey background). To generate the model, about 150 turbostratic particle nucleation sites were randomly generated within the matrix with dimension of 20 nm×20 nm. The density of the particles were chosen to represent the experimentally measured values from TEM images^{10,53}. The square matrix is chosen based on previous modeling works on nanocomposite, which used 2D square⁷⁰ or 3D cubic matrix⁷¹. Larger aspect ratios increased the scatter in the conductivity measurements.

The particles were then grown from nucleation sites in two directions, representing the a-axis and c-axis in graphitic (turbostratic) particles, as shown in Figure 17(C). The orientation angle of each particle, defined as the angle of the a-axis with the CNF axial direction (along which electrical conductivity of CNF model was calculated), was chosen randomly to be below a maximum orientation angles (θ_{max}). A value of θ_{max} of 90° corresponds to a completely randomly oriented particles (particles can have any orientation randomly selected between 0° and +90°). Reducing θ_{max} will generate a cell with particles inclined towards the CNF axis. A θ_{max} of zero corresponds to perfect alignment (not studied in this work). The growth rate in c-axis of turbostratic carbon is defined as 0.005nm/step, which is 0.286 times the a-axis growth rate, intended to replicate the average aspect ratio of turbostratic domains structures from experimental TEM images. The electrical conductivity of turbostratic carbon is assumed to be the same as the deposited pyrolytic graphite⁷², due to its structural similarity to high defect density graphite. To avoid inter-particle penetration, when the minimum distance between two particles became smaller than some critical distance (growth prohibition distance, GPD), the growth of particle in that direction was stopped. The minimum distance between neighboring particles (the same as GPD) was determined based on experimental electrical conductivity of CNF with different carbonization temperature, explained in section 2.2. This growth mechanism effectively simulates the random size and distribution of turbostratic carbon in practical CNF sample. As the particles grow, the volume fraction of conductive turbostratic particles will increase and reach its percolation threshold. Regardless of the resemblance of our employed growth particle growth approach to experiments, this method can be used to replicate nonpenetrating particles in other types of composites, such as CNT reinforced polymers and TFR.

The electrical path within a percolated network of particles includes two types of resistances, inter- and intra-particle participate, which were calculated as discussed in the following sections.

Inter-particle resistance: The inter-particle resistance is assumed to be generated from the electron tunneling effect between two conductive particles. The tunneling resistivity between two adjacent turbostratic particles can be estimated as⁷³:

$$\rho_{tunnel} = \frac{h^2}{e^2 \sqrt{2m\lambda}} \exp\left(\frac{4\pi d}{h} \sqrt{2m\lambda}\right) \quad (1)$$

where e is electron charge, m is the mass of electron, h is Plank's constant, λ is the barrier height of matrix amorphous carbon and d is the tunneling distance. From experimental results⁷⁴, two resistivity bounds are considered for the tunneling resistivity in CNF. The upper bound corresponds to the resistivity of the matrix (amorphous matrix) which is $4.56 \times 10^{-3} \Omega \cdot m$. The lower bound, $1.81 \times 10^{-4} \Omega \cdot m$, is the lowest resistivity measured in CNFs, assuming to represent the case of full growth of turbostratic domains and a completely percolated network between them, as shown in Figure 18 (A).

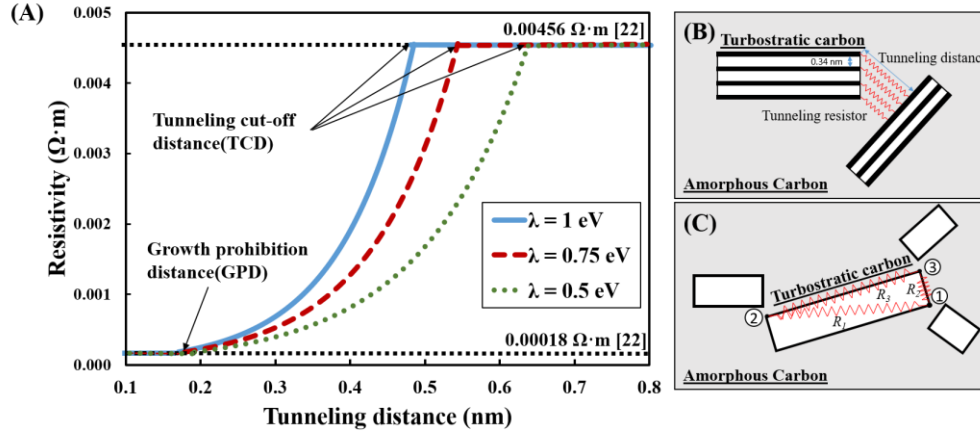


Figure 18. (A) Tunneling resistivity between two particles with different tunneling distances (B) Inter-particle conductance calculation (C) Intra-particle conductance calculation.

When the minimum distance between two particles are smaller than the tunneling cut-off distance (TCD) for certain barrier height, the tunneling resistance will be calculated. The tunneling resistance between adjacent two particles can be calculated from the parallel tunneling resistors method, as shown in Figure 18(B). To this end, each turbostratic particle will be assumed to consist of parallel graphene layers (along the a-axis) spaced apart by 0.34 nm. Each graphene layer will then be connected to the neighboring particle via a tunneling resistor, which is parallel to the rest of tunneling resistors at that specific contact site (Figure 18(B)). To calculate the resistance of each tunneling resistor, the conducting length was considered to be the distance from end point of each graphene layer in turbostratic carbon to the edge of the other particle. Moreover, the projection of 0.34 nm, which is the interlayer distance in turbostratic carbon on the other contacting plane is used as conducting width. The tunneling resistivity is obtained from Figure 18(A) with different barrier height and tunneling distance.

Intra-particle resistance: In existing models to predict electrical conductivity of hybrid nanocomposite, such as CNTs/Polymer nanocomposite, the intra-particle conductivity is mainly assumed to be along the axis of the filler and is calculated simply by applying Ohm's law to 1D geometries^{71,75}. This is a reasonable assumption in calculating the overall electrical conductivity of the nanocomposite, mainly due to high aspect ratio (up to several hundreds) of fillers. However, the ratio of the conductivities of turbostratic domains to amorphous carbon is significantly lower, in the order of 10^2 - 10^4 times, and with aspect ratio to about 3.5. Therefore, proposed approaches in the literature to estimate intra-particle conductivity needs to be revisited. Given the random distribution of the size of each turbostratic carbon and location of contact points, FEA is used here to calculate the resistance within each particle.

Given the anisotropic atomic structure of turbostratic domains along the a- and c-axis in CNF, each particle is assumed to be electrically anisotropic with $\sigma_a = 4.25 \times 10^4 \text{ S/m}$ and $\sigma_c = 1.39 \times 10^3 \text{ S/m}$ ⁷². Considering electrical anisotropy of particles, each particle which is in contact with n other particles (at n

contact nodes), can be replaced with $n(n-1)/2$ equivalent internal resistors, each connecting two contact points from within the particle (Appendix A). The following algorithm was then used to calculate these equivalent internal resistors of a particle. We first applied a potential of $V = 1\text{V}$ to node 1 (here node 1 is considered to be the primary node) while all other nodes were at $V = 0\text{V}$. This boundary value problem was solved via FEA (Details of FEA is in Appendix B). To this end, we meshed the rectangle particle with about 50,000 elements. The elements were triangular shaped with three nodes at the apexes. Dirichlet boundary condition was applied at all the contact points. By applying $V = 1$ at one contact point and $V = 0$ at all other points, the potential distribution for this boundary condition inside the particle is obtained by solving the steady state electrical conduction Laplace equation in orthotropic medium without internal current source ⁷⁶,

$$\sigma_x \frac{\partial^2 \phi}{\partial x^2} + \sigma_y \frac{\partial^2 \phi}{\partial y^2} = 0 \quad (2)$$

From the FEA, the input current to each node was calculated. Since all the nodes except node 1 are at zero potential, the input current from all the nodes should output from node 1. Therefore, the resistance of the equivalent internal resistor connecting any arbitrary node i ($i \neq 1$) to node 1 is equal to the inverse of the input current at node i (note that the voltage difference between node i and 1 is 1 V). Through iteration of the primary node (the node at $V = 1\text{V}$ while others are at $V = 0\text{V}$), all the internal resistors can be calculated for each particle.

Calculation of the electrical resistance of the network: The resistance of the conduction path composed of internal resistances of conductive particles connected via tunneling resistance within them was calculated as follows. The current for each contact node i within the network was calculated by using Kirchhoff's current law as follows,

$$I_i = \sum_{j=1}^n \frac{V_i - V_j}{R_{ij}} \quad (3)$$

where j is the node number connected to node i , V_i and V_j are the potential at node i and j , and R_{ij} is the resistance between node i and j . It is to be noted that R_{ij} is either the internal resistance of particles (when i and j are on the same particle) or the tunneling resistance between two particles (when a particle is connected at its contact node i to contact node j of another particle). Moreover, the left and right sides of the CNF box were considered electrodes 1 and 2, respectively, each to represent an isopotential line. By setting the electric potential of nodes at electrode 1 to be 1V and at electrode 2 to be 0 V, the potential of all nodes within the network can be calculated by solving a system of linear equations ⁷⁷. The electrical conductivity of CNF is evaluated by using Ohm's law based on the net current flow between the two electrodes.

Results and Discussion

An example of the calculations of the internal resistances in a turbostratic domain with three contact nodes is shown in Figure 19. For a particle with 3 contacts ($n = 3$), the number of internal resistances is 3. The boundary conditions required to capture the internal resistance were applied at contact nodes ⁷⁸, and the electrical potential distribution of the turbostratic particle was obtained, as shown in Figure 19(B). In this example, size of turbostratic particle is $1.23\text{nm}(L) \times 0.46\text{nm}(W)$, which is a typical size for turbostratic carbon in CNF from experiment. To calculate the internal resistors of the particle, first we applied $V = 1\text{V}$ at node 1 while other nodes were at 0V (in B.C.1, node 1 is the primary node). Therefore, the values of R_2 and R_3 were calculated in unit of ohms as $1/i_2$ and $1/i_3$, where i_2 and i_3 were the calculated input currents in units of Amps at nodes 2 and 3, respectively, based on FEA analysis of the particle (described in section 2.3). Similarly, by applying $V = 1\text{V}$ to node 2 and keeping the other two nodes at 0V (B.C.2 where node 2 is the primary node), R_1 and R_3 were calculated, and by applying $V = 1\text{V}$ to node 3 and keeping the other two nodes at 0V (B.C.3 where node 3 is the primary node), R_1 and R_2 were calculated.

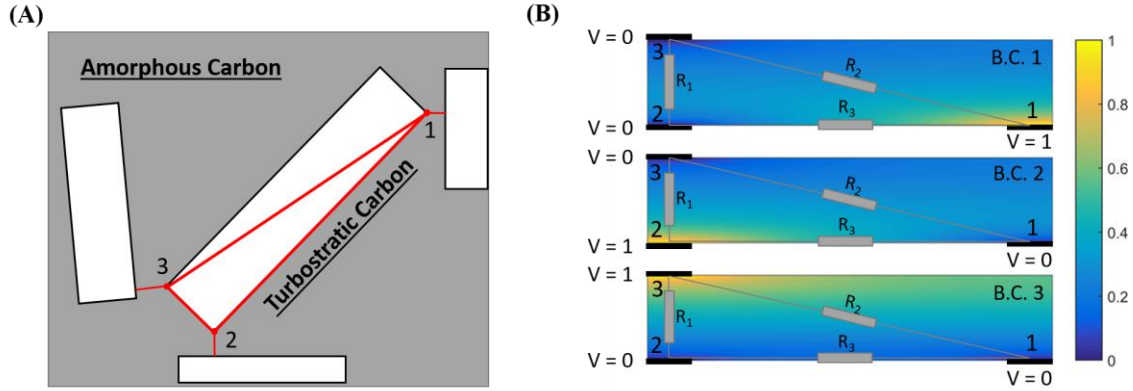


Figure 19. (A) Conductive particle with three contact points and (B) Equipotential line result for a typical sized particle based on FEA.

As noted in this example, each resistor can be calculated by applying $V = 1V$ to either of its two ends, while keeping the rest of the nodes at $0V$. That is, each resistor can be calculated from two sets of calculations. This redundancy is simply because of the fact that $R_{ij} = R_{ji}$ (shown in Appendix A). In our analysis, the two calculated values of each resistors were the same within a margin of 2%, believed to be caused by numerical errors. In the example shown in Figure 19(B), the calculated resistance values are $R_1 = 8.70 \times 10^5 \Omega\cdot m$, $R_2 = 8.74 \times 10^5 \Omega\cdot m$ and $R_3 = 4.86 \times 10^5 \Omega\cdot m$.

It is to be noted that if the simplified Ohm's law method used in previous modeling work⁷¹ for traditional nanocomposite was used, the resistance calculation results would have been $R_1 = R_2 = \rho_c \frac{L}{W \cdot T} = 2.69 \times 10^5 \Omega\cdot m$ and $R_3 = \rho_a \frac{W}{L \cdot T} = 6.29 \times 10^4 \Omega\cdot m$ which will generate a relatively large error ($\sim 70\%$) compared to the FEA results. Moreover, corresponding inter-particle resistances from these three contact points to other particles (Figure 19(A)) are $1.91 \times 10^5 \Omega\cdot m$, $7.98 \times 10^4 \Omega\cdot m$ and $1.90 \times 10^6 \Omega\cdot m$, which are comparable to the intra-particle resistances. Therefore, for this particle, using FEA to calculate accurate intra-resistance is critical to predict electrical conductivity of the whole CNF.

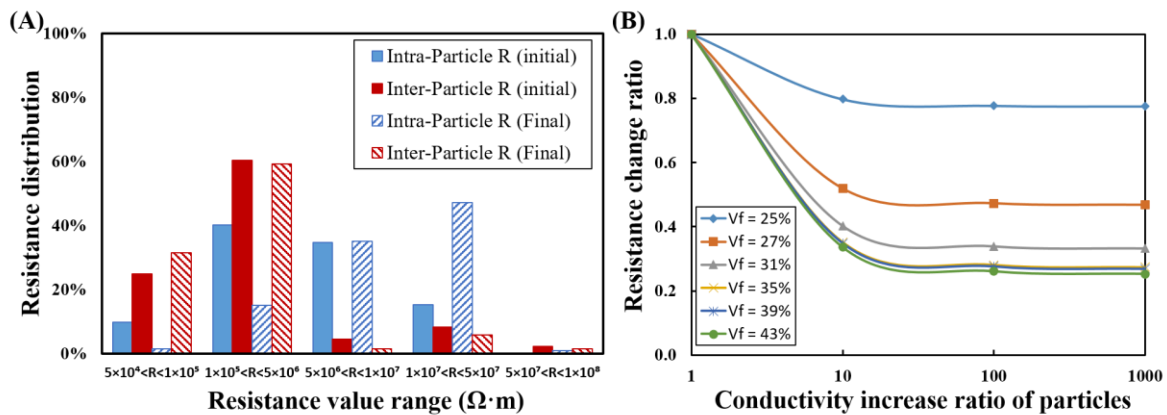


Figure 20. (A) Intra-particle and inter-particle resistances distribution for initial and final CNF structure and (B) Electrical resistance change ratio of CNF with increasing particle conductivities.

The comparison between intra- and inter-particle resistances distribution in CNF on percolation (initial) and saturation (final) state, where the growth of all particles is stopped by the neighboring particles or the

boundaries of the CNF, is shown in Figure 20(A). As seen in the figure, all the inter-particle and intra-particle resistances at any volume fraction larger than percolation threshold are within the $5 \times 10^4 \Omega \cdot m$ to $1 \times 10^8 \Omega \cdot m$ range, indicating that both of these two types of resistances play an important role in determining the overall conductivity of the CNF. By growing the particle from the percolation state to a saturation state, the intra-particle resistance values increase and the distribution of intra-particle resistance moves to the right (higher resistance values). This trend is expected since larger particle size is equivalent to longer conduction path within each particle. In contrast, as the particles grow, the inter-particle resistance values will decrease due to the decrease in tunneling distances between particles. Hence, by growing the turbostratic structure particles the contribution of the intra-particle resistances to the overall electrical conductivity of CNF will increase.

In order to show the significance of particle conductivity to overall conductivity of CNF, we considered hypothetical cases where the conductivity of particles was significantly above the expected values, where σ_a and σ_c were 10, 100 and 1000 times their expected value of 4.25×10^4 and 1.39×10^3 S/m, respectively. In all cases, the ratio of σ_a and σ_c remained the same (~ 30). The results are presented in Figure 20 (B). The y axis in the figure is the calculated electrical resistance of the whole CNFs normalized by the electrical resistance of CNFs corresponding to the most expected values of particle conductivities along the a- and c-axis at percolation threshold ($V_f = 25\%$). The normalized electrical resistance of CNFs is plotted as a function of volume fractions and electrical conductivity of particles (relative to the most expected values of electrical conductivity of particles).

As expected, for all volume fractions of particles, by increasing electrical conductivity of turbostratic particles, the resistance of CNFs initially drops and reaches a plateau. The plateau corresponds to a hypothetical case when the electrical conduction within CNF is mainly controlled by tunneling resistance simply due to unrealistically high conductivities of particles. Hence, this analysis suggests that at low volume fractions (near the percolation threshold), the conduction within particles may constitute only $\sim 20\%$ of the electrical resistance of CNFs (only a 20% drop in resistivity is observed by increasing the particle conductivity 100 and 1000 times). This ratio will increase with volume fraction. It is such that near the saturation point ($V_f = 43\%$), the electrical resistance of CNFs is mostly ($\sim 75\%$) due to conduction within particles (a nearly 75% drop in resistivity by increasing the particle conductivity 100 and 1000 times). Therefore, the consideration of both inter- and intra-particle conduction are critical in reliably predicting the electrical properties of CNFs.

To develop a better understanding of the parameters which influence overall electrical resistivity of CNF, the effect of particle alignment, anisotropic growth rate and volume fraction on the percolation threshold and conductivity is analyzed in the following parts. Moreover, the effect of the matrix tunneling barrier height on the macroscopic conductivity is discussed.

Electrical conductivity of CNFs vs. particle volume fraction and conductivity: Guided by the growth of turbostratic particle size with carbonization time and temperature¹⁰, we grew the turbostratic domains in steps in the model. As shown in Figure 21, the electrical conductivity of the model can be calculated after reaching the percolation threshold (81 ± 68 S/m). The reported value is an average of 10 measurements and the uncertainty is their standard deviation. By increasing the size of the particle and therefore the particle volume fraction, the electrical conductivity of CNF increases, reaching a plateau of 1303 ± 119 S/m, corresponding to the saturation volume fraction of particles ($\sim 43\%$). At low volume fraction, at or near the percolation threshold, the standard deviation in the predicted electrical measurements can be a significant portion of the predicted values. However, the absolute value of the standard deviation of electrical conductivities will decrease with volume fraction, and will reach $\sim 10\%$ at the saturation volume fraction, which is smaller than the experimental error ($\sim 15\%$)²⁵. The reported experimental electrical conductivity⁷⁴ of CNF with different carbonization temperature (1100°C and 1500°C) is shown in Figure 21 with dashed lines. The predicted electrical conductivity with different particle volume fraction is within the experimental conductivity range. The relatively high standard deviation near the percolation threshold is due to the high sensitivity of conductivity to volume fraction near the percolation threshold. While more

experiments are needed to validate the modeling results, current 2-D model indeed effectively describes the microstructure of CNF in relation to its electrical conductivity. Moreover, the matching between experimental and modeling results is likely an indication of the proper values chosen for the particle conductivities in our analysis (σ_a and σ_c).

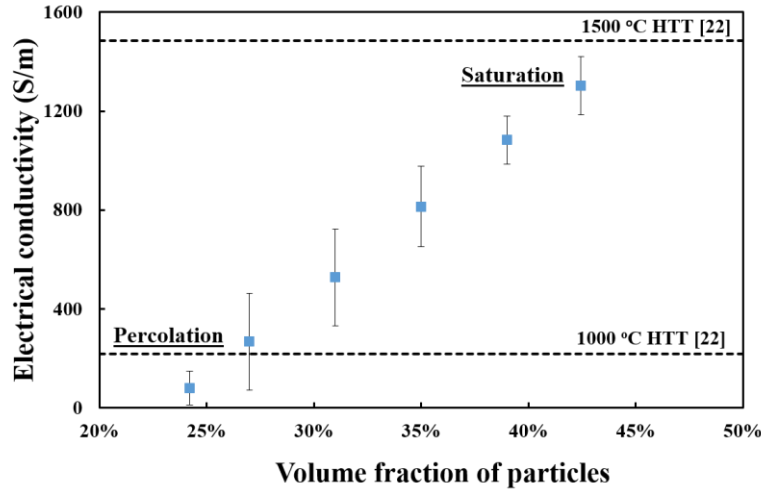


Figure 21. Electrical conductivity of CNF with increasing particle volume fraction.

Effect of particle alignment and anisotropic growth rate on percolation probability: Apart from the physical properties of individual turbostratic particles, their geometry and alignment will also influence the formation of a conduction path within CNFs and their electrical property. The formation of the conduction path can be best described by the Percolation probability of turbostratic particles, P , as a function of particle alignment and anisotropic growth rate within CNF. As shown in Figure 22(A), for very low particle volume fractions (16%), the percolation probability is very low for all alignment conditions. By increasing the volume fraction of particles, the difference in percolation probability for different alignment conditions becomes more clear. For instance, for CNF with $V_f = 24\%$, by decreasing the maximum orientation angle of particle from 90° (corresponding to totally random orientation) to 60° , there is a slight increase in the percolation probability, indicating the contribution of particles that are more aligned with CNF axis in bridging the gap between the two ends (electrodes) of CNFs⁷⁰. Further increase in the particle alignment by reducing θ_{max} to 30° and 10° , leads to a slight drop in P .

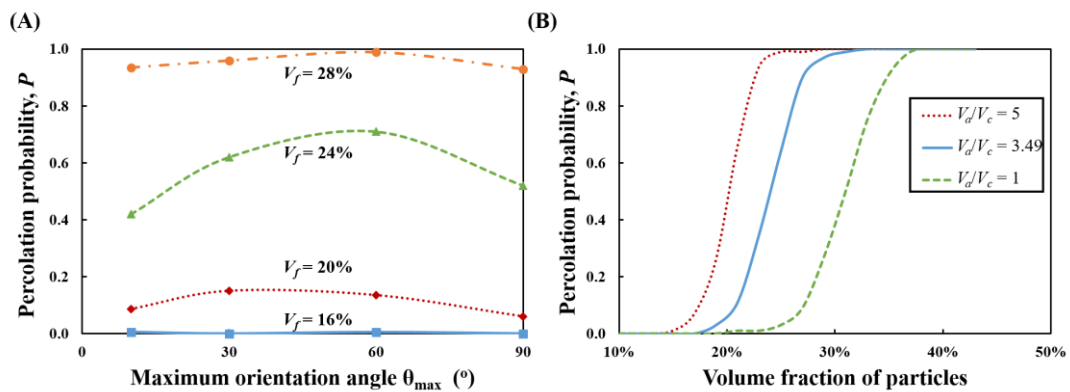


Figure 22. Effect of (A) Particle alignment and (B) Anisotropic particle growth rate on the percolation probabilities, P of CNF

The maximum probability is obtained between $\theta_{max} = 30^\circ$ and 60° . The drop in percolation probability at higher degrees of alignment can be attributed to low density of transversely oriented particles which can bridge the gap between aligned particles. The peak of percolation probability becomes broader as the particle volume fraction is increased. That is mainly because at such high volume fractions, many of the particles are grown to sufficiently large dimensions to contact with their neighboring particles.

As pointed out in section 2.1, the growth rate of particles along the a- and c- axis in the model was taken to represent the experimentally observed aspect ratio of turbostratic domains in CNFs. However, other aspect ratios may also be reached experimentally for instance via templated carbonization or hot-drawing of precursors of CNFs and consequent chain alignment⁵³.

In this section, we investigated the effect of particle aspect ratio on percolation threshold. As shown in Figure 22(B), by increasing particle anisotropic growth rate ratio from 1 to 5, there is an evident increase in percolation probability. That is simply because longer particles can reach out to other particles that are further away to form the conduction path. This increased probability indicates the effectiveness of increasing particle growth rate anisotropy in generating more conductive pathways. It is however to be noted that compared to CNTs/polymer nanocomposite, the aspect ratio of the fillers (turbostratic carbon) cannot be very large in CNF, because in practice, large particles are thermodynamically more favorable to grow in non-straight fashion.

Effect of particle alignment and anisotropic growth rate ratio on conductivity: The effect of particle alignment and anisotropic growth rates on electrical conductivity of CNF was also studied. As shown in Figure 23(A), similar to the percolation probability corresponding to different particle alignment, there is an electrical conductivity peak at about $\theta_{max} = 60^\circ$, at which the electrical conductivity is 26% higher than the case of randomly oriented particles, an indication of the more conductive pathways generated due to induced particle alignment (refer to Figure 22(A)).

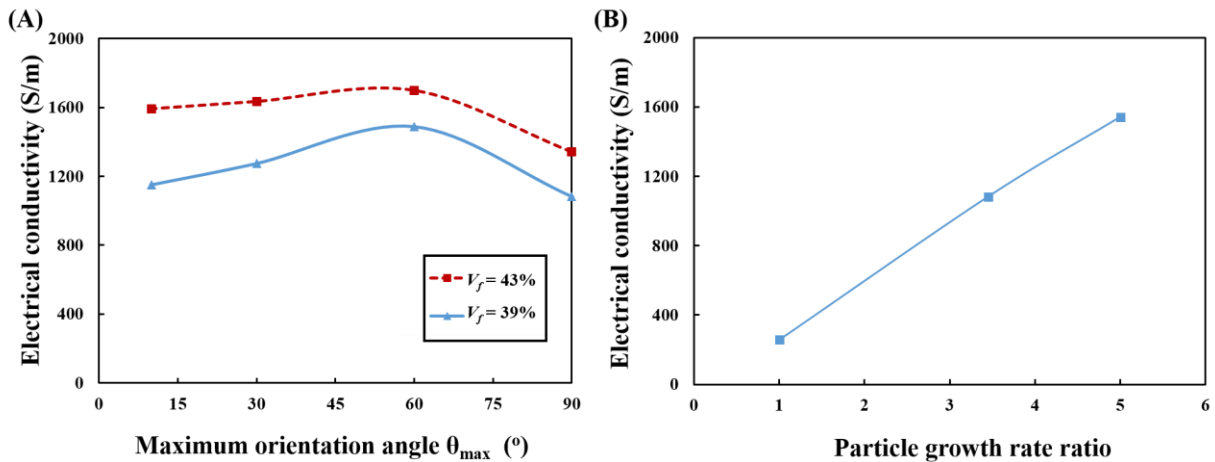


Figure 23. Effect of (A) Particle alignment and (B) Anisotropic particle growth rate on electrical conductivity of CNF

The decrease in electrical conductivity by enhancing particle alignment beyond $\theta_{max} = 60^\circ$ is mainly due to a reduction in the probability of the formation of contact points between particles in the lateral direction (similar to the trend observed in percolation probability in Figure 22(A)). These contact points can generate new conduction paths, increasing the electrical conductivity. This result is consistent with previous experimental and modeling results on the effect of conductive particle alignment (CNTs) on nanocomposite electrical conductivity^{70,75}. Moreover, this result provides an effective method for improving the electrical conductivity of electrospun CNF through partial alignment. For instance, in fabricating CNFs, the chains

of the polymer precursor can be aligned through hot-drawing as a means to induce turbostratic particle alignment in the later carbonization process. Through controlling the fabrication conditions, the alignment of turbostratic particle can be controlled and based on this modeling results, an optimum alignment condition should be targeted to achieve the maximum electrical conductivity.

In addition to particle alignment, particle aspect ratio can influence the CNF conductivity. As is shown in Figure 23(B), by increasing the particle growth rate ratio, there is an evident increase in the overall electrical conductivity. This improvement is caused by the increased percolated pathways, alluded to by the increased P for larger particle growth rate ratios.

The sensitivity of conduction path and conductivity to barrier height: Apart from the properties of particle, the matrix properties, mainly the energy barrier height corresponding to electron tunneling, will also have an important influence on overall conductivity of the CNF. The effect of matrix tunneling barrier height on the percolation probability and conductivity of CNF is shown in Figure 24(A). By lowering the barrier height, the cut-off tunneling distance will increase (Figure 18(A)), thus, the percolation threshold will be decreased, suggesting that lower barrier height will facilitate the formation of conductive path within CNF. However, the influence of barrier height on electrical conductivity is not as evident compared to the effect of other parameters discussed so far, i.e., particle conductivity and alignment (Figure 24(B)), especially at high volume fractions. The insignificant contribution of barrier height to conductivity of CNFs stems partly from the fact that at high particle volume fraction, most of the particles are in contact with other particles, thus, the tunneling distances are near the lower bound. At high particle volume fraction, the contribution of the intra-particle resistances is more important than inter-particle resistances as discussed in section 3.

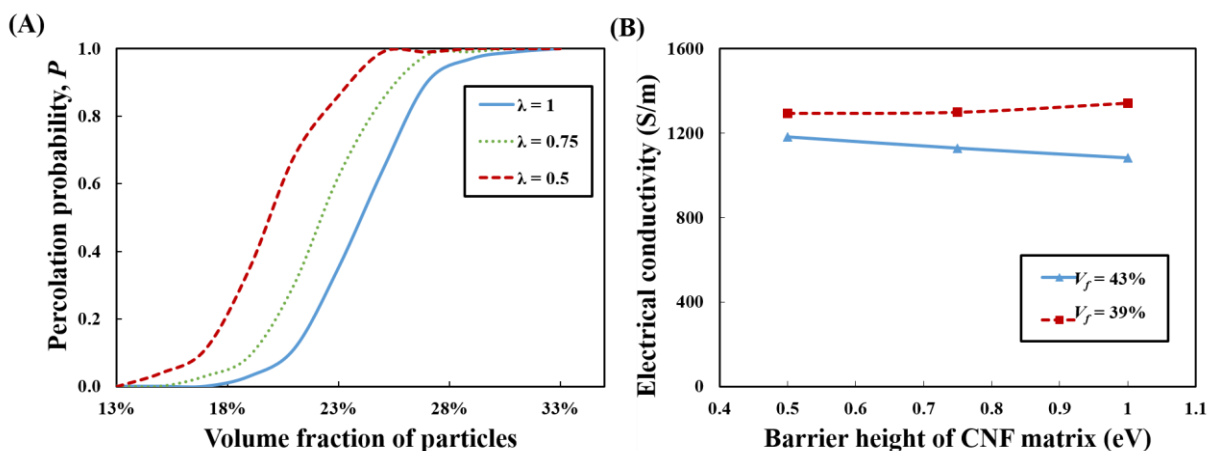


Figure 24. Effect of barrier height on (A) Percolation probability, P of CNF and (B) Electrical conductivity

Conclusion of this section

A multi-resolution two-dimensional (2D) resistor network model was developed and presented to analyze the electrical conductivity of hybrid nanomaterials which are composed of insulating matrix with hard-core (non-penetrating) conductive particles. The model takes into account both intra- and inter-particle resistance. The model was applied to predict the electrical conductivity of electrospun carbon nanofibers, assuming to be composed of conductive particles (turbostratic domains) in a matrix of amorphous carbon or remnants of the precursor (assumed to be non-conductive). The modeling results show that intra-particle resistances make an important contribution to macroscopic electrical conductivity of CNF and this contribution is higher at larger particle volume fractions. The reason for the latter is twofold. First, higher volume fraction increases the effective size of the particles and thus their electrical resistance. Second, larger particles reduce the tunneling distance between particles. By increasing the volume fraction and

conductivity of the turbostratic particle, the conductivity of whole CNF will increase, which is consistent with the experimental results. Both particle alignment and anisotropic growth rate ratio will influence the conductivity of CNFs. With respect to particle alignment, an optimum alignment is proposed to result in highest CNF conductivity. Lower or higher alignments lead to lower conductivity by reducing the possibility of the formation of a percolated conduction path within the CNFs. However, among these parameters, introducing partially alignment particle is more applicable in the fabrication process to enhance conductivity of CNF. The modeling results can provide valuable information to modify the fabrication parameters of CNF, to achieve high electrical conductivity CNF.

4.4. Formation of Wavy and Helical CNFs with Controlled Morphology

Electrospun carbon nanofiber (CNF) has been demonstrated to possess outstanding physical properties with relatively low fabrication cost. In this work we report a mechanics-based approach to fabricate CNFs with controllable waviness through carbonization of electrospun precursor nanofibers which are subjected to microbuckling inside a sacrificial matrix. Compared to the “bottom-up” method of production employed by CVD, electrospinning takes advantage of its “top-down” manufacturing process, which facilitates production, assemblage, and alignment^{1,2}. This study focuses on the fabrication, material properties and mechanics that leads to the formation of wavy carbon nanofibers, in order to establish the relationship between processing parameters and the resulting wavy fiber geometry. These fabrication-structure-properties relationships will help in designing a scalable methodology with full control of the final outcome in terms of geometry and properties. The flexible carbon nanosprings and wavy nanofibers can be used in micro and nanoelectromechanical system devices, deployable structures, flexible displays, energy storage, catalysis, nanocomposites and a multitude of other uses.

Experimental Section

Fabrication of PAN nanofiber ribbons and PAN/PMMA composites: Ribbons of PAN nanofibers as precursors of helical CNFs were fabricated by electrospinning (Figure 25). To this end, polyacrylonitrile (PAN) powder from Sigma Aldrich with a molecular weight of 150,000 g/mol was dissolved into dimethylformamide (DMF) to obtain a 12 wt. % solution (PAN in DMF). The feeding rate of the polymer solution during electrospinning was kept at 1.4 ml/h to achieve stable electrospinning jet. Highly aligned polymer nanofiber ribbon was obtained by using a rotating disk collector with a peak-up velocity of ~5.7 m/s at electrospinning voltage and distance of 18 kV and 20 cm, respectively. The as-electrospun PAN nanofiber ribbons were dip-coated with PMMA by inserting them into an 8 wt.% solution of PMMA (from Sigma Aldrich with a molecular weight of 350000 g/mol) in dichloromethane (DCM) solution for 15 minutes and then drying to form a nanocomposite containing PAN nanofiber and PMMA matrix.

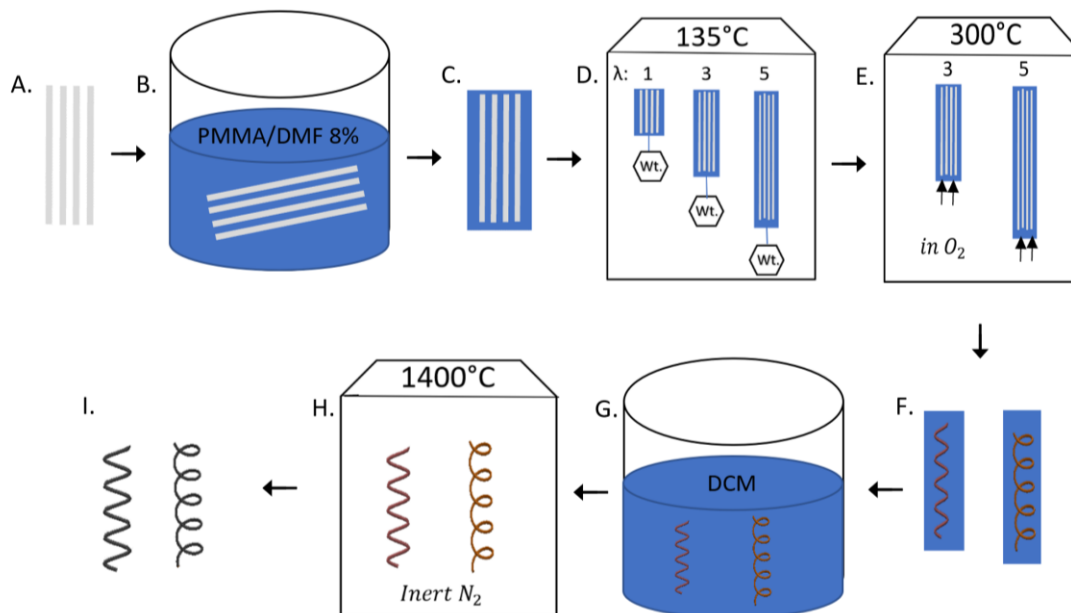


Figure 25. Schematic of manufacturing procedure: A) Electrospun PAN ribbon B) Dip coating with PMMA C) PAN/PMMA nanocomposite D) Hot drawing to stretch ratio (λ) 3 and 5 E) Entropic and chemically induced compression in stabilization F) Sinusoidal and helical PAN fibers in PMMA G) PMMA removal H) Carbonization I) Sinusoidal and helical carbon nanofibers.

Hot-drawing of PAN/PMMA ribbons and thermomechanical characterization: The electrospun PAN/PMMA nanofiber ribbons were subjected to hot drawing as follows. The as-spun PAN/PMMA composites were stretched at 135° C environment in an oven by hanging weights to them, inducing engineering stress of ~19 MPa. When the draw ratio (λ , the ratio of the final to initial length) reached the desired values (3 and 5), the stretched ribbons were cooled down to room temperature. Hot drawing plays a crucial role in fiber diameter, alignment, and crystallinity ¹. During the hot drawing process, the PAN nanofibers undergo drawing-induced crystallization ¹, while the PMMA matrix remains largely amorphous.

As the modulus values of both PAN and PMMA change with hot drawing (due to changes in chain orientation and crystallinity) and temperature (viscous effects), we performed detailed dynamic mechanical analysis (DMA) with temperature sweep from 30-160°C of pure PAN and PMMA films (hot drawn to $\lambda = 1, 3$ and 5) to obtain modulus values and moduli ratio. For this purpose, the PAN and PMMA film samples were prepared separately by solvent casting 10 % PAN/DMF and PMMA/DMF solution in a petri dish and dried in a vacuum oven at 40°C for 12 hours. The films were hot drawn at 135°C to $\lambda = 1, 3$ and 5. The DMA tests were carried out in TA instruments DMA 850 analyzer in tension mode, using sinusoidal stress with a frequency of 2 Hz and amplitude of 5 μm . The temperature was ramped from 30 to 160°C at a ramping rate of 10°C/min. The results are presented in the supplementary information (SI).

Fabrication of wavy/helical CNFs: The PAN nanofibers were subsequently stabilized. To this end, the hot-drawn PAN/PMMA composite was thermally stabilized at 300° C in the presence of oxygen which results in the conversion of $\text{C} \equiv \text{N}$ groups of PAN chains to $\text{C} = \text{N}$, forming a stable cyclic ladder-like structure ². Moreover, during the stabilization process, the entropic (mostly active in amorphous PMMA) and chemical reaction (mainly in stabilizing PAN) induce the shrinkage of hot-drawn PAN/PMMA composite. The shrinkage of the composite is dominated by the entropic forces within the PMMA, due to both its much larger relative mass and its amorphous structure which provides high mobility for PMMA chains. The PAN nanofibers accommodate the large relative shrinkage imposed on them by the matrix mainly via constraint buckling. Because of large compressive strains and condition of symmetry, the buckling under the constraint of surrounding PMMA matrix can result in either a planar wavy (sinusoidal) or a 3-dimensional helical buckling as readily observed in compressive buckling of a fiber in an elastomeric matrix ⁷⁹⁻⁸³. After the microbuckling of the PAN fibers due to thermal shrinkage in the matrix, the deformed shape of the PAN nanofibers is fixed due to chemical crosslinks (cyclization).

In the carbonization process, the PMMA phase will be fully decomposed and PAN nanofiber will be transferred to CNF. Carbonization is carried out at 1400°C in a nitrogen atmosphere in the tube furnace for 10 hours which enables the formation of turbostratic domains in the PAN nanofibers with the elimination of non-carbon atoms from the chains. Finally, we get ribbons of thousands of aligned wavy carbon nanofibers.

Characterization of the geometry of CNFs: The diameter of PAN/PMMA nanofiber was measured by using FEI Quanta 600 FE-SEM with at least 10 measurements. All other dimensional parameters were measured using image processing software ImageJ with multiple measurements of each. Wavy (2D axis) and helical fibers (3D axis) were respectively characterized in terms of output parameters such as wavelength and amplitude for wavy fibers, and pitch and helix radius for helical fibers.

Theoretical analysis for the formation of wavy/helical CNFs

The shape of the wavy carbon nanofibers observed in this study resembles those of fibers subjected to buckling inside an elastic matrix ⁷⁹⁻⁸¹. In our study, the buckling of PAN nanofibers can be caused by the entropic shrinkage of the PMMA matrix during the thermal stabilization.

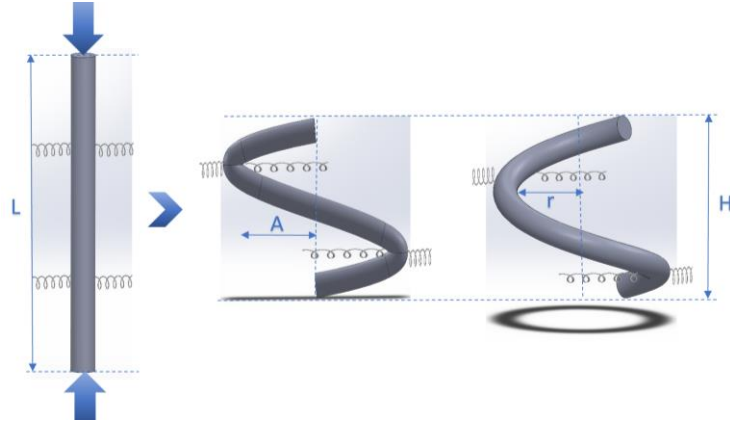


Figure 26. Straight PAN nanofiber surrounded by PMMA matrix buckled into sinusoidal and helical fiber matrix. The springs represent the equivalent elastic response of the matrix.

Here, we present a modeling scheme based on elastic energies stored in a matrix-fiber system to capture the formation of wavy/helical fibers. The buckled shape of fibers can be explained in terms of the energy minimization principle, including the elastic energy stored in the fiber as it buckles and the energy stored in the matrix as it is pushed away by a buckling fiber. This analysis only considers the post-buckled shape of the fiber.

We thus assume that during the shrinkage of the matrix, the energy released by the recoiling of the PMMA chains will be partly stored as mechanical (elastic) energy in the fibers as they undergo buckling. The buckling will also displace the matrix laterally, storing mechanical (elastic) energy in the matrix. We further assume that the deformation of the fibers and lateral deformation of the matrix during the shrinkage is elastic, and that the wavy/helical shape of the fiber will be maintained post-buckling as fibers go through thermal stabilization (chemical crosslinking) and carbonization. The primary components of the model are shown in Figure 26.

Elastic energy stored in a system of microbuckled wavy fiber-matrix (sinusoidal): The model contains a fiber with the initial length L which buckles into a sinusoidal shape. As a result of the buckling, the end-to-end distance of the fiber will change from L to αL , as shown in Figure 27A, where $0 < \alpha < 1$. For example, for a matrix shrinkage of 25% (engineering strain of -25%) where the end-to-end distance of the fiber is reduced by 25%, α is 0.75. Due to the much larger mass of the matrix, it is safe to assume that the relative change in the end-to-end distance of the fiber is equal to the shrinkage in the matrix, with the former being accommodated via microbuckling. Thus, for a given shrinkage in the matrix, a wavy fiber can deform into various mode shapes, Figure 27A. The mode shapes can be identified by a positive integer n , such that the end-to-end distance of the buckled fiber is equal to the product of n and half the wavelength of the fiber, H (Figure 26), i.e., $H = 2\alpha L/n$.

The shape of a wavy fiber with amplitude A and wavelength H can be described as:

$$y = A \sin(2\pi x/H) \quad (1)$$

The strain energy stored in sinusoidal fiber can be calculated as:

$$U = \int_0^{\alpha L} \frac{M^2}{2EI} dx \quad (2)$$

In addition, the magnitude of the moment can be expressed as the radius of curvature of the buckled fiber at an arbitrary position x as, R_{sin} ,

$$M = -EI/R_{sin} \quad (3)$$

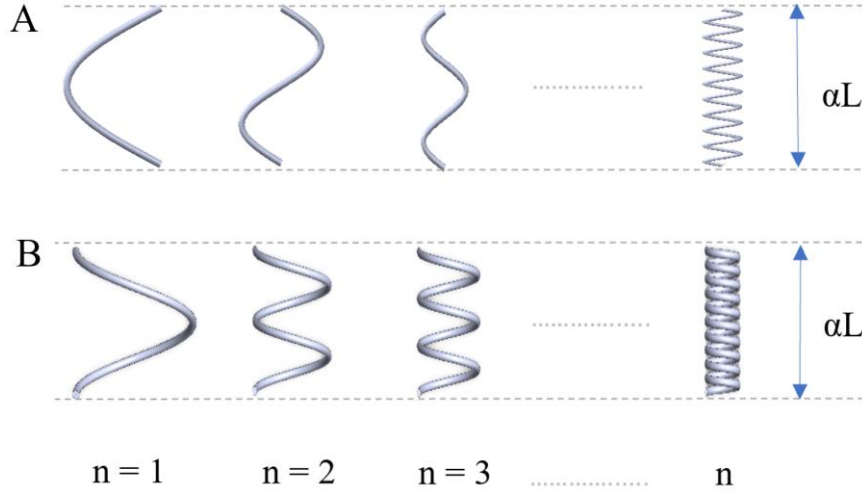


Figure 27. A) Mode shapes of sinusoidal and B) helical buckling mode.

where R_{sin} is the radius of curvature of sine curve, to be calculated from equation (1).

From (1)-(3), the strain energy in sinusoidal fiber becomes

$$U_{sin_{fib}} = \int_0^{\alpha L} \frac{\left(\left(\frac{2\pi^2 EIA}{H^2} \right) \sin^2 \left(\frac{2\pi x}{H} \right) \right)}{\left(1 + \left(\frac{4\pi^2 A^2}{H^2} \right) \cos^2 \left(\frac{2\pi x}{H} \right) \right)^3} dx \quad (4)$$

The microbuckling of the fiber is accommodated by the displacement of the matrix. The energy stored in the matrix can be estimated as follows. We represent the matrix as a combination of linear springs aligned perpendicular to the fiber axis as the matrix is assumed to behave linear elastically, shown schematically in Figure 26. The stiffness of these springs is a function of the elastic modulus of the matrix, as estimated elsewhere⁷⁹. Matrix displacement (y) will be captured in the model as elongation/compression in springs which stores energy in the matrix as:

$$y = \int_0^{\alpha L} \frac{1}{2} Ky^2 dx \quad (5)$$

where k of the matrix (stiffness per unit area) is calculated based on the work of Darby⁷⁹ as,

$$k = 8\sqrt{2G_m E_m} \quad (6)$$

In equation (6), E_m and G_m are the tensile and shear moduli of the surrounding matrix respectively. Combining equations (1), (5) and (6) ultimately gives us the energy stored in the matrix for wavy nanofiber as:

$$U_{sin_{mat}} = \frac{KA^2H}{8\pi} \left(\frac{2\alpha\pi L}{H} + \frac{\sin\left(\frac{4\alpha\pi L}{H}\right)}{2} \right) \quad (7)$$

From equations (4) and (7), the total strain energy in the fiber and matrix during sinusoidal buckling can be estimated as (note that $H = 2\alpha L/n$):

$$U_{sin} = \int_0^{\alpha L} \frac{\left(\frac{2\pi^2 EIA}{H^2} \right) \sin^2\left(\frac{2\pi x}{H}\right)}{\left(1 + \frac{4\pi^2 A^2}{H^2} \right) \cos^2\left(\frac{2\pi x}{H}\right)} dx + \frac{KA^2H}{8\pi} \left(\frac{2\alpha\pi L}{H} + \frac{\sin\left(\frac{4\alpha\pi L}{H}\right)}{2} \right) \quad (8)$$

Elastic energy stored in a system of microbuckled wavy fiber-matrix (helical): The energy stored in the system during the formation of the helical fibers can be calculated using a similar approach. For a given shrinkage in the matrix, a wavy fiber can deform into various mode shapes, Figure 27. The mode shapes can be identified by a positive integer n , such that the end-to-end distance of the buckled fiber is equal to the product of n and the pitch of the helical fiber (Figure 27B), $H = \alpha L/n$.

In a helical fiber, an arbitrary point on the helix has spatial coordinates of $[R \cos \theta, R \sin \theta, (H/2\pi) \theta]$, where θ is the radial angle ranging from 0 to 2π and H is the pitch of the helix for various mode shapes. The tangential direction at this point is then identified with a vector with the following components $(-R \sin \theta, R \cos \theta, H/2\pi)$. The length of one turn of the helix is thus $L = 2\pi\sqrt{R^2 + H^2/(2\pi)^2}$. We take L as a constant (i.e., the initial length of the fiber, ignoring axial deformations of the fiber). Thus, the in-plane radius of the helix (the radius of the projection of the fiber on a plane normal to the pre-buckling fiber axis) is:

$$r = \frac{1}{2\pi} \sqrt{L^2 - H^2} \quad (9)$$

The radius of curvature, R_{hel} , is:

$$R_{hel} = \frac{r^2 + \left(\frac{H}{2\pi}\right)^2}{r} \quad (20)$$

Therefore, the bending moment in the fiber will be:

$$M = -EI/R_{hel} \quad (11)$$

Using equation (2), we can estimate the strain energy stored in fiber as:

$$U_{hel_{fib}} = \alpha EIL / 2 \left(\frac{\frac{1}{4\pi^2}(L^2 - H^2) + \left(\frac{H}{2\pi}\right)^2}{\frac{1}{2\pi}\sqrt{L^2 - H^2}} \right)^2 \quad (12)$$

Here, we have neglected the effect of shear and torsion, as we expect insignificant contributions from them to the overall energy functions as explained in the Appendix.

The energy stored in the matrix which is deformed by a helical fiber can be calculated as follows. Considering a circular helix, each point on the curve lies at a distance r from the axis, thus, the displacement function (y) of the matrix can be approximated as the radius of the helix (Equation (9)):

Hence, the energy stored in the matrix in the case of helical fiber becomes:

$$U_{hel_{mat}} = \left(\frac{1}{2} k y^2 \right) \alpha L = \frac{\alpha k}{8\pi^2} (L^2 - H^2) L \quad (14)$$

$$y = \frac{1}{2\pi} \sqrt{L^2 - H^2} \quad (13)$$

Combining (12) and (14), the total energy stored in helical buckling becomes (note that $H = \alpha L/n$):

$$U_{hel} = \alpha E I L / 2 \left(\frac{\frac{1}{4\pi^2} (L^2 - H^2) + \left(\frac{H}{2\pi} \right)^2}{\frac{1}{2\pi} \sqrt{L^2 - H^2}} \right)^2 + \frac{\alpha k}{8\pi^2} (L^2 - H^2) L \quad (15)$$

Results and Discussions

The shape of the CNFs as a function of the hot-drawing ratios applied to the PAN/PMMA composites was studied via SEM imaging. In each case, fibers were aligned in the hot drawing direction. We considered three draw ratios, 1, 3 and 5. The draw ratio of 1 simply implies that no hot-drawing was applied to the sample (the final and initial length were the same), Figure 28A. It served as our reference sample. SEM images of carbon nanofibers (CNFs) revealed that the hot drawing ratio (λ) of 1, results in straight CNFs, while applying a hot-drawing ratio of $\lambda=3$ resulted in CNFs with a wavy profile which can be assumed as planar (2D) sinusoidal curves, Figure 28 B, whereas samples made with $\lambda=5$ exhibited a helical shape, Figure 28C. In some cases, the sinusoidal fibers have shown out of plane bents, as observed in SEM images (e.g., Figure 28B). However, the in-plane bending curvature and thus the elastic energy stored in this bending mode is respectively much larger than the out-of-plane buckling curvature and the corresponding bending elastic energy. This is the key distinguishing factor between the sinusoidal and helical fibers. As such, in our model, the elastic energy in the out-of-plane bending mode of sinusoidal fibers is ignored.

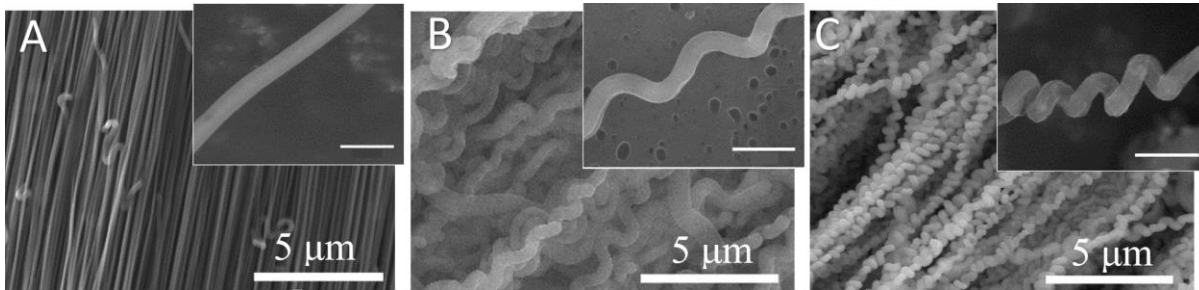


Figure 28. A) Aligned straight fibers with a single fiber shown inset B) Aligned sinusoidal fibers with a single fiber shown inset C) Aligned helical fiber with a single fiber shown inset. (All scale bars in inset images are 1 μm).

The formation of wavy and helical CNFs in cases of $\lambda=3$ and 5, in contrast to the straight CNFs formed at $\lambda=1$, is strong evidence that wavy/helical fibers form as a result of microbuckling within a thermally

shrinking PMMA matrix. To evaluate the relative ability and tendencies of PAN nanofibers and PMMA matrix to shrink during thermal stabilization, pure PAN nanofiber ribbons, PMMA films, and PAN/PMMA ribbons were subjected to various degrees of hot-drawing and their shrinkage during subsequent heat treatments was measured, Figure 29. As shown in the figure, there are considerable differences between the shrinkage of PMMA films and PAN nanofiber ribbons. After hot-drawing to a draw-ratio of 5, the matrix shrinks by ~60% at ~160 °C, compared to the small shrinkage of the PAN nanofiber ribbons (less than 10%). The small shrinkage of PAN nanofibers can be attributed to the hot-drawing induced crystallization in PAN nanofibers¹. The crystalline domains serve as permanent anchor points within each PAN nanofiber, preventing considerable shape changes by entropic forces during thermal stabilization. In contrast, PMMA ribbons remain largely amorphous throughout the whole process, and the hot-drawing can induce chain alignment in PMMA, reducing the entropy of the matrix. When the sample is heated to ~160 °C (above the glass transition temperature of the PMMA) during the thermal stabilization process, the entropic forces will drive the recoiling of the PMMA chains, leading to considerable shrinkage. Since chain alignment achieved in PMMA during hot-drawing is expected to be proportional to hot-drawing ratio, it is not surprising that the magnitude of the shrinkage is directly related to the hot-drawing ratio (compare cases of PAN/PMMA with $\lambda=3$ and 5, Figure 29). It is also interesting to note that the shrinkage profile of the PAN/PMMA films is nearly the same as that of PMMA film, suggesting that the shrinkage of the overall dimensions of the sample is driven by PMMA phase due to its much larger relative mass.

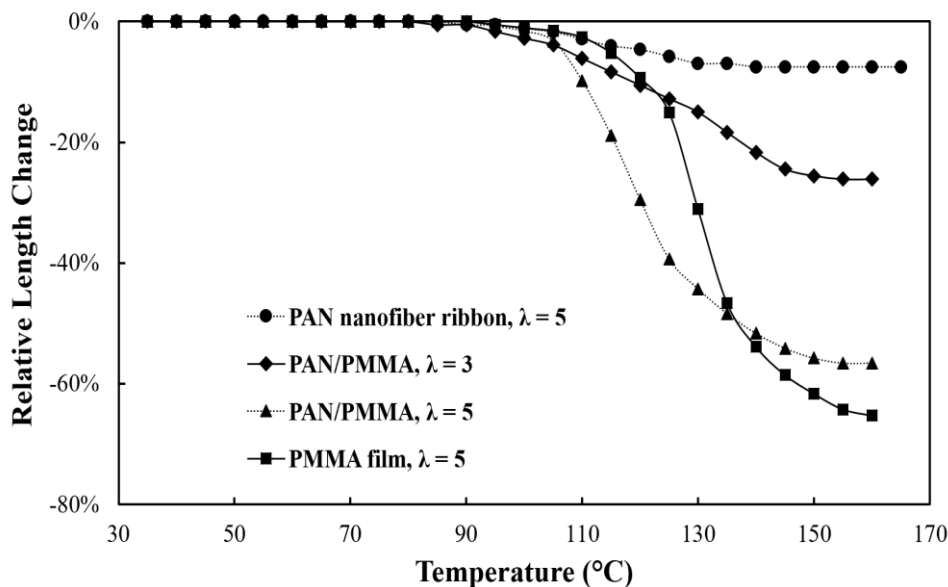


Figure 29. Stress-free relative change in length as a function of temperature for pure PAN nanofiber ribbons, PMMA films and PAN/PMMA nanocomposite ribbons (hot drawn to $\lambda = 1, 3$ and 5). The temperature change includes the range in which PAN nanofibers buckle within PMMA matrix.

The wavelength and amplitude of wavy CNFs (mostly obtained from PAN/PMMA composite samples with $\lambda = 3$) were measured as a function of the CNF diameter from SEM images such as those shown in Figure 28B. It was observed that both wavelength and amplitude increase with fiber diameter, as shown in Figure 30A. Similarly, SEM images of helical fibers (mostly obtained from PAN/PMMA composite samples with $\lambda = 5$), such as those in Figure 28C, revealed a nearly linear increase in pitch and helix radius with fiber diameter, as shown in Figure 30B.

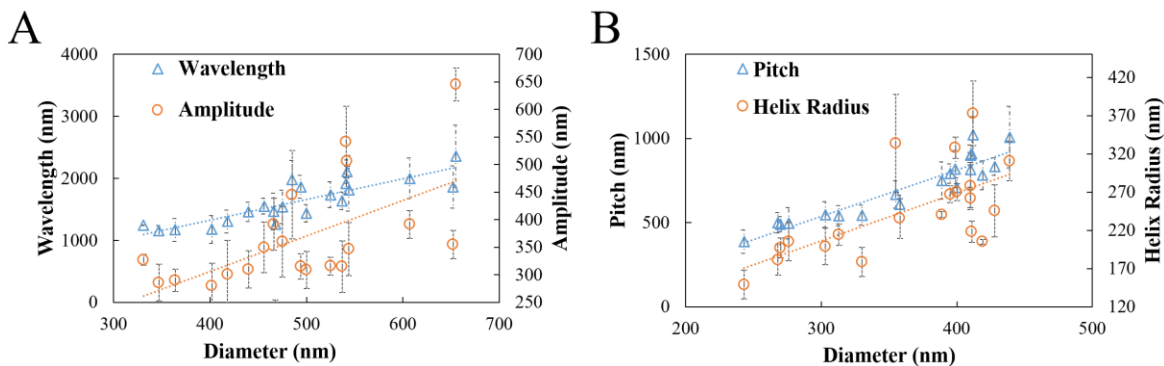


Figure 30. A) Change in wavelength and amplitude with respect to the fiber diameter for sinusoidal fibers, which formed at hot draw ratio 3, B) Change in pitch and helix radius with respect to the fiber diameter for helical fibers, which formed at hot draw ratio 5.

Surface morphology of wavy and helical fibers: As shown in Figure 31, the surface of the straight and wavy CNFs are more or less smooth, but the surface morphology of helical fibers exhibits wrinkles. The abundance of this surface morphology only in helical fibers suggests that the wrinkles form as a result of this extreme deformation. This surface features can be compared to the deformed shape of a long and thin cylindrical rod subjected to pure torsion (Torque applied parallel to the axis of the cylinder). The torque is known to provoke a twisting instability, evolving from an initial kink to a knot, and if this deformation is hindered, for example, by a surrounding matrix, wrinkles (surface instability) occur on the surface at a given critical angle of torsion^{84,85}. All of these conditions are present when the helical CNFs form, that is, torsion is inherently induced when a helix is compressed axially, and PMMA matrix applies constraint resulting in the instability on the soft surface of PAN nanofibers as they buckle.

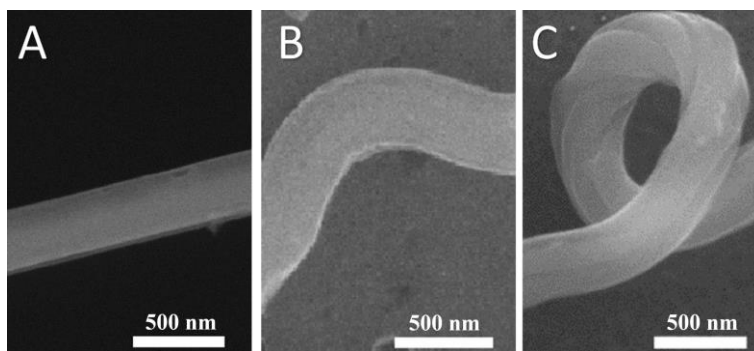


Figure 31. Surface morphology of A) straight fiber with smooth surface B) sinusoidal fiber with smooth surface, C) helical fiber with visible surface wrinkling.

Predictions of the shape of the wavy and helical fibers: We used the model developed in section 3 to predict the shape of the wavy fibers and helical fibers and also to identify which shape (helical/wavy) is more energetically favorable. To this end, for an experimentally measured value of matrix shrinkage and mode shape, we calculated the energy stored in each form, wavy or helical fibers. For each deformed shape (wavy or helical), the energy becomes the lowest for a certain value of n . Lower and higher n values will result in higher stored energy in the fiber-matrix system due to respectively excessive matrix deformation and sharp bends (curvature) of the fiber. The mode shape which resulted in the lowest energy was calculated by considering various values of n . The minimum energy states of the two shapes were then calculated and the deformed shape and mode shape with the lowest energy was reported as the predicted prevailing shape (Equations 8 and 15). The corresponding value of n (representing the mode shape) was used to calculate

the predicted wavelength of the wavy fibers and the pitch of the helical fibers. The results were then compared with the experiments.

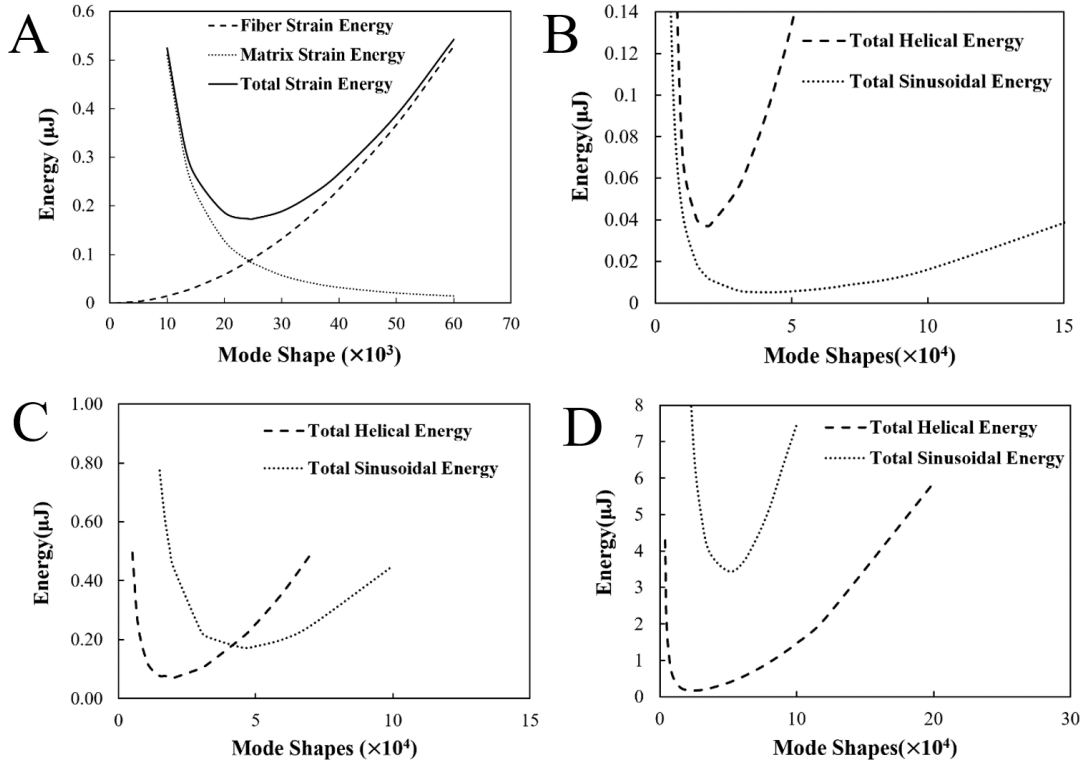


Figure 32. A) Strain energy stored in fiber and matrix in helical buckling of a 400 nm diameter fiber with initial straight length of 10 cm, surrounded by a matrix with $E_f/E_m = 250$ for $\lambda=5$ at 150°C , showcasing the mode shape with minimum energy for pitch and helix radius prediction. B) Total energy comparisons between sinusoidal and helical buckling for the case of 10 % shrinkage revealing the energetically favorable sinusoidal buckling mode C) For 25% shrinkage ($\lambda=3$), revealing that both buckling modes are energetically favorable as the minimum energy state are of same order D) For 60% shrinkage ($\lambda=5$), revealing the energetically favorable helical buckling mode.

As an example, to predict the pitch and helix radius of a fiber buckling in helical shape for $\lambda=5$, we started with a 400 nm thick fiber with an initial straight length of 10 cm, which is the same as the actual length of PAN-PMMA ribbon used in experiments. This ribbon reduces to the length of 4 cm after 60% shrinkage as shown in Figure 29 for $\lambda=5$. Using the helical buckling model presented in section 3.2, we plotted the energy stored in fiber (equation 12) and matrix (equation 14) as fiber buckles into a helix, starting with first mode shape (i.e. only one turn of the helix) to thousands of turns. A critical parameter to calculate the energies in fiber and matrix is their elastic moduli. As shown in Figure 29, most of the shrinkage of PMMA which leads to buckling of PAN nanofibers occurs within the temperature range of $100\text{-}150^\circ\text{C}$. According to the results of DMA analysis, within this range of temperature, the ratio of the moduli of PAN to PMMA remains nearly independent of temperature, but highly dependent on drawing ratio (λ). This ratio is around 90 for $\lambda=3$ and 250 for $\lambda=5$ as shown in the supplementary information document. The modulus values change with hot drawing and temperature, hence, the input values used for the model here are taken from DMA analysis for hot drawing ratio (λ) of 5 at a specific temperature of 150°C (See the supplementary document for the case of $\lambda=3$). The elastic modulus of PAN fiber is 441 MPa and 1.8 MPa for the PMMA matrix, the Poisson's ratio for PMMA at 150°C (much higher than PMMA glass transition temperature) is taken as 0.5 referenced from the book of Bicerano⁸⁶, and the shear modulus is obtained using the isotropic

material behavior. The results are plotted in Figure 31A. As shown in the plot, the minimum energy state is reached when the helix has a mode shape of 25000, resulting in minimum energy of 0.17 μJ .

We then proceeded by calculating the minimum energy that will be stored in a wavy buckling mode when subjected to a matrix shrinkage of 60%. In this case, the minimum stored energy will happen for mode shape of 50000, resulting in minimum energy of 3.5 μJ (more than 20 times the energy in the helical fibers). This value is much higher than the energy stored in the helical buckling, leading to the prediction that at $\lambda=5$ it is the helical fiber shape that prevails as the lowest energy state.

Dividing the experimental buckled length of 4 cm with these number of turns of the minimum energy state of the helical fiber (mode shape of 25000) gives us the value of pitch (H) to be 1.6 μm which is close to the experimentally measured value of 0.9 μm , for the 400 nm thick fiber (Figure 30B). Using equation 14, the radius of curvature comes out to be 590 nm which is of the same order as the experimentally observed value of around 280 nm.

Similarly, wavelength and amplitude can be predicted for the fibers that are subjected to $\lambda=3$ (shrinkage ratio α of 0.75), as shown in the supplementary document. In this case, the mode shape of the wavy and helical fibers with lowest energies are respectively 45000 and 19000, and their minimum stored energy are respectively 0.17 and 0.07 μJ . Compared to the case of $\lambda=5$, presented earlier in this section, where the minimum energy of a helical fiber was ~ 20 times less than a wavy fiber, in case of $\lambda=3$, the minimum energy of the two shapes are comparable. Based on the mode shape of the minimum energy state (45000), the value obtained for the wavelength of a 400 nm fiber that buckled in sinusoidal shape is around 2 μm and corresponding amplitude to be 740 nm which are of the same order of experimentally observed values of wavelength and amplitude of 1.2 μm and 300 nm respectively. The difference between the experimental values and the predicted from the model can be attributed to the assumptions of linear behavior and a large range of diameter distribution of fibers in the PAN ribbon.

Our analysis presented in the next section provides more insight regarding the transition from wavy (2D) shape to helical as the shrinkage is increased.

Transition from wavy to helical CNFs, a comparison with theory: The model can also explain the transition from one shape to another by increasing the value of matrix shrinkage. To this end, we used the buckling models to plot the total energy stored in sinusoidal buckling (equation 8) and helical buckling (equation 15) as a function of the mode shape to compare the minima of energies stored in the fiber matrix system of the buckled fiber for the cases of 10%, 25% ($\lambda=3$) and 60% ($\lambda=5$) shrinkage. We took the fiber diameter to be 400 nm and initial length of the fiber, L , to be 6cm. Given the periodicity in the deformation, this does not limit the scope of the applicability of these results. For 60% shrinkage ($\lambda=5$), the elastic modulus of PAN fiber at 150°C is 441 MPa and 1.8 MPa for the PMMA matrix. For 25% shrinkage ($\lambda=3$), the elastic modulus of PAN fiber at 150°C is 183 MPa and 2.1 MPa for the PMMA matrix. All these values were sourced from the DMA analysis. The Poisson's ratio for PMMA at 150°C is taken as 0.5. The case of 10% was added to better illustrate the trends. However, for the 10% matrix shrinkage, the elastic modulus values were not tested directly and estimated via a 2nd order polynomial fit interpolation using DMA data for $\lambda=1$ (no shrinkage), $\lambda=3$ (25% shrinkage) and $\lambda=5$ (60% shrinkage). As shown in Figure 32, in the case of 10% shrinkage (Figure 32B), sinusoidal shape is energetically more favorable than the helical case but as we move to 25% shrinkage (Figure 32C) both the buckling modes are more or less equally favorable and at 60% shrinkage (Figure 32D), helical mode is clearly more favorable.

Building on the results of Figure 32, we plotted the minimum energies of both the sinusoidal and helical buckling modes for a range of shrinkage from 10% to 60% with appropriate scaling of material properties based on DMA data. The results are plotted in Figure 33 for a fiber with a diameter of 400 nm. The plot presents the progression of the buckling and the total mechanical energy stored in the PAN-PMMA system as a function of the shrinkage of a buckling fiber. Based on Figure 33, it is clear that for small shrinkage value, the in-plane sinusoidal configuration is the lower energy deformation compared to a helical fiber. However, as the fiber gets more and more compressed (i.e., reducing the wavelength/pitch), there comes a

transition point where helical shape becomes energetically more favorable (For the specific conditions listed in Figure 33, this value obtained is 20% shrinkage).

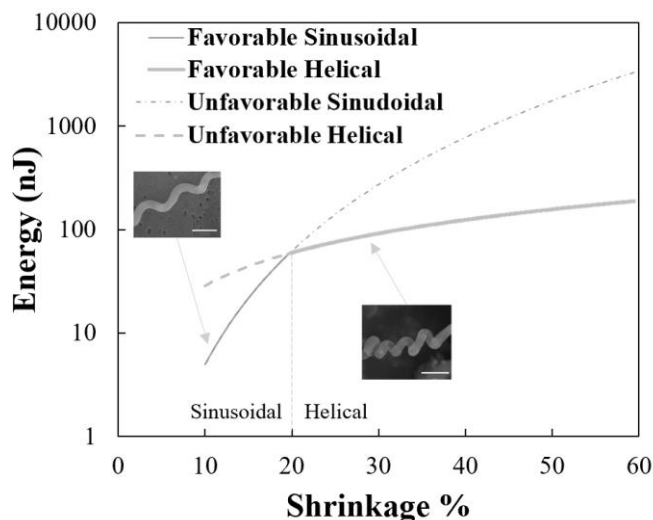


Figure 33. Total strain energy stored in case of sinusoidal and helical buckling for mode shape with minimum energy vs shrinkage of a 400 nm fiber of initial length 6 cm, showcasing the transition from sinusoidal to helical shape based on minimization of energy as shrinkage increases from 10% to 60%. (all scale bars are 1 μ m).

Qualitatively, the model prediction is in line with our experimental observation that the wavy fibers form at lower hot-drawing ratios (which correspond to lower shrinkages during stabilization). According to our experimental observation, for low hot draw ratio (λ) of 3 which corresponds to 25% shrinkage, we get mainly sinusoidal fibers, while the model predict a transition to helical shape at slightly lower shrinkage ratios (~20%). The observation of slight out of plane buckling in SEM images of the wavy fibers at 25% (such as Figure 28B) could be an indication of the onset of helical fiber formation. At higher draw ratios, the model and experiment show better matching. For instance, as we go to hot draw ratio (λ) of 5 which corresponds to 60% shrinkage, mainly helical CNFs form as predicted from the model in Figure 33.

Conclusion of this section

In this section, we have presented a novel method to produce wavy and helical carbon nanofibers (CNFs). The waviness/helicity of CNFs was achieved by subjecting the precursor PAN nanofibers to constraint buckling inside a matrix of PMMA. The shrinkage in PMMA was induced by triggering entropic forces, while the formation of crystals in PAN nanofibers had significantly limited their ability to shrink in response to entropic forces. As a result, PAN nanofibers buckled in-plane or out-of-plane, depending on the magnitude of the shrinkage of the matrix. It was observed that the wavelength (pitch) and amplitude (helix radius) of the sinusoidal and helical fibers are directly proportional to the fiber diameter. The pitch and radius in case of helical fibers and wavelength and amplitude in case of sinusoidal fibers were predicted using minimization of strain energy stored in fiber-matrix system. The results agreed well with the experiments. The transformation of wavy fibers from sinusoidal to the helical shape by increasing the shrinkage as observed in experiments was quantitatively explained by considering the elastic energy stored in the fiber-matrix system during the thermal shrinkage.

4.5. Mechanics of Porous CNFs with Application To Energy Storage

In this article, for the first time, we demonstrate the great potential of using porous CNFs as structural supercapacitor electrode material. The outline of this article is as follows: first, we demonstrate the effect of activation conditions on the morphology and microstructure of activated porous CNFs. Next, we present the supercapacitor performance of activated porous CNFs as a function of activation conditions. Next, we present the experimental result of the mechanical properties of different activated porous CNFs, the mechanism of the reduction in mechanical properties is analyzed. Next, we discuss the potential of using porous CNFs as electrode materials in structural supercapacitors. The trade-off between energy storage and load-bearing capabilities of porous CNFs activated at different conditions is analyzed with multifunctional efficiency.

Experimental Section

Fabrication of activated porous CNFs: The hollow and porous CNFs were fabricated by carbonizing polymeric precursors. Polymer precursor fibers were first electrospun using coaxial electrospinning setup. Solution pumped to a 21 gauge inner needle was made by dissolving Poly(methyl methacrylate) (average $M_w \sim 350,000$, Sigma-Aldrich) in Dimethylformamide (DMF) ($\geq 99\%$, Sigma-Aldrich) at 16 wt.%. An emulsion of PAN/PMMA in DMF was pumped to a 12 gauge outer needle. The emulsion was made by dissolving Polyacrylonitrile (PAN) (average $M_w \sim 150,000$, Sigma-Aldrich) and PMMA (average $M_w \sim 15,000$, Sigma-Aldrich) in DMF at 9.1 wt.% and 9.1 wt.% at the same time, the mixture was stirred vigorously for 12 hrs to form an emulsion. The shell and core flow rate were 0.98 ml hr^{-1} and 0.7 ml hr^{-1} . Electrospinning was conducted at a voltage of 15 kV and a distance of 20 cm. Fibers were collected using a grounded rotating drum with an angular velocity of 500rpm (take up velocity of 3.9 m s^{-1}). Temperature and relative humidity during electrospinning was $25 \pm 1^\circ\text{C}$ and $40 \pm 2\%$ respectively. After electrospinning, the precursor fibers ribbons were collected from the drum collector and stabilized in a convection oven at 270°C for 2 hrs in an air atmosphere. The stabilized fibers ribbons were then transferred to a tube furnace (MTI GSL-1700X) and carbonized in nitrogen atmosphere at 1100°C for 1 hr.⁸⁷ As prepared porous CNF ribbons were then soaked in KOH aqueous solution with concentration ranging from 1 M to 4 M for 3 hrs at room temperature, the ribbons were then taken out of the solution and dried in vacuum oven at 80°C for 3 hrs. After drying, the ribbons were thermally treated in nitrogen atmosphere at 800°C or 1000°C for 30 min in a tube furnace. The activated porous CNF ribbons were washed with deionized water and dried in vacuum oven at 80°C for 3 hrs.

Microstructure characterization: SEM images of the porous CNFs were obtained by FEI Quanta 600 FE-SEM at 20 kV. The cross-section of the porous CNFs was exposed by fracturing with a razor blade. To prepare the TEM samples, the porous CNFs were dispersed in water by bath ultrasonication for 5 mins, the porous CNF dispersion was then dropped on to TEM grid and dried at 80°C for 30 min. TEM images of the porous CNFs were acquired with JEOL JEM-2010 TEM at 200 kV. N_2 adsorption isotherms were obtained at 77K with Quantachrome Autosorb iQ. Porous CNFs were degassed at 250°C for 4 hrs under vacuum before test. The Raman spectra were acquired with a Horiba Jobin-Yvon LabRam Raman confocal microscope using He-Ne laser (633 nm). The XPS spectra were acquired by an Omicron XPS/UPS system with Al X-ray source. To increase the stability of system, a CN10 charge neutralizer installed on this XPS system is used to minimize charging on samples. The porous CNFs were attached to the sample holder using double-side copper tape.

Electrochemical characterization: The capacitance of the porous CNF electrode is characterized by using a symmetric two-electrode cell set up. 6M KOH aqueous solution was used at electrolyte. The specific capacitance of the working electrode is evaluated by cyclic voltammetry and constant current charge discharge technique using CH Instrument 700B Bipotentiostat. In cyclic voltammetry, the specific

capacitance is calculated as
$$C_{\text{specific}} = 2 \cdot \frac{1}{2k \cdot m \cdot \Delta V} \oint IdV$$
, where I is the current, k is the scan rate (V s^{-1}),

m is the weight of a single porous CNF electrode and ΔV is the scanning potential window. In constant current charge discharge test the specific capacitance is calculated as $C_{specific} = 2 \frac{I \cdot Dt}{m \cdot DV}$, where I is the discharge current, Δt is the discharge time, m is the weight of a single porous CNF electrode and ΔV is the discharge potential window.^{88,89}

Mechanical characterization: The mechanical properties of the porous CNFs were measured by single fiber tensile test using MEMS based mechanical testing platform. Single carbon fibers were placed on MEMS device using a tungsten probe controlled by a micro-manipulator under optical microscope. A Platinum block was deposited using Tescan LYRA-3 Focused Ion Beam Microscope to grip the fiber. A Newport Picomotor Actuator (model 8303) was used to actuate by the devices. Time lapse images were captured using an optical microscope during the test at 1 frame per sec. The force and displacement were determined by analyzing the images using digital image correlation (DIC) software (VIC-2D). More details of the single fiber test can be found in our previous work.⁸⁷

Results and Discussion

Morphology and structure of KOH-activated porous CNFs: The porous CNFs were fabricated by coaxial electrospinning of PAN/PMMA emulsion in the shell and PMMA in the core, followed by thermal stabilization at 270 °C for 2hrs and carbonization at 1100 °C for 60 min. The pristine porous CNFs were then activated with KOH to increase the surface area. The mass ratio of KOH to carbon and activation temperature significantly influenced the activation of carbon materials.^{90,91} Previous studies showed that the BET surface area of KOH-activated carbon material increases with the KOH/carbon mass ratio^{90,92,93} and activation temperature up to 1000 °C.⁹¹ In this study, KOH was introduced into the porous CNF mat by soaking the mat in the KOH solution. KOH solution concentrations of 1 M, 2 M and 4 M and the activation temperatures of 800 °C and 1000 °C were selected. The samples were labeled according to the activation conditions, i.e. KOH concentration and activation temperature.

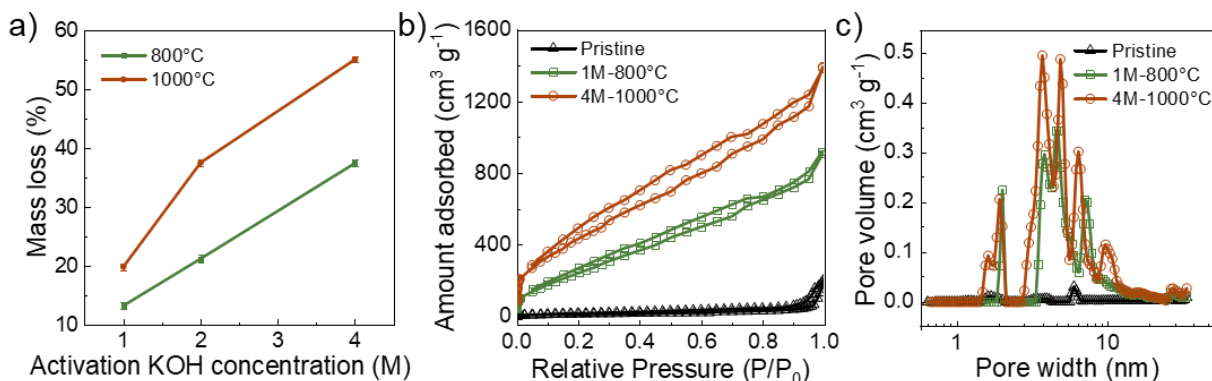


Figure 34. a) Mass loss ratio after KOH activation for different activation conditions, error bars represent the uncertainty of the electrode weight measurement, b) N₂ adsorption isotherm and c) pore size distribution for pristine, 1M-800 °C and 4M-1000 °C porous CNFs

KOH activation both at higher temperature and higher KOH concentration increased the relative mass loss as shown in **Figure 34**. The activated porous CNFs with the lowest (1M-800 °C) and highest (4M-1000 °C) mass loss ratio were selected for further studies to reveal the effect of activation on the mechanical and electrochemical performance of porous CNFs structure.

Nitrogen adsorption isotherms of pristine, 1M-800 °C and 4M-1000 °C porous CNFs are shown in Figure 34b. The BET surface area and total pore volume both increased significantly after the KOH activation as shown in Figure 34b & 1c and **Table 3**. The increased BET surface area (20 to 30 times) is a result of the partial etching of the porous CNFs during the KOH activation which leaves micro and meso pores.⁹⁰ The pore size distribution was calculated by Quenched Solid State Functional Theory (QSDFT) method, Figure 34c. The volume of micropores (< 2 nm) and mesopores (2~50 nm) increased more than 4x after 1M-800 °C activation (compared to un-activated CNFs) and increased further by another ~50% with 4M-1000 °C activation. The average pore diameter decreased from 23.83 nm in pristine CNFs to 5.3 nm for 1M-800 °C activation and 4.91nm for 4M-1000 °C activation due to the generation of new micro and meso pores.

Table 3. Nitrogen adsorption results of porous CNFs

	BET surface area (m² g⁻¹)	Average pore diameter (nm)	Total pore volume (cm³ g⁻¹)
Pristine	52.3	23.82	0.31
1M-800 °C	1059.0	5.30	1.40
4M-1000 °C	1753.9	4.91	2.15

The activated porous CNF mat and the electrode are flexible and showed good structural integrity as shown in **Figure 35a-b**. To understand the effect of the KOH activation on the morphology of the porous CNFs, the microstructure of pristine porous CNFs and activated porous CNFs (1M-800 °C and 4M-1000 °C) were studied using field emission scanning electron microscope (FE-SEM), transmission electron microscope (TEM), Raman spectroscopy, and X-ray photoelectron spectroscopy (XPS). The average diameter and shell thickness measured from SEM images (with 30 samples per case) are shown in Figure 35d. The average diameter for pristine, 1M-800 °C and 4M-1000 °C porous CNFs was 2.13±0.40 μm, 1.75±0.35 μm and 1.46±0.32 μm, respectively, and their average shell thickness were 0.31±0.06 μm, 0.31±0.06 μm and 0.28±0.06 μm, respectively. The porous CNF diameter decreased after the activation by ~17.8% after activation at 1M-800 °C and 31.5% after activation at 4M-1000 °C. However, the shell thickness experienced much smaller changes after activation. The average shell thickness remained nearly the same after 1M-800 °C activation and decreased by 11.2% after 4M-1000 °C activation.

Surface morphology of the porous CNFs also changed during the activation. The surface of the pristine porous CNFs is relatively smooth, Figure 35e. After the KOH activation, pits and dents appear on the fiber surfaces, Figure 35h & k. On the cross-section surfaces of the porous CNFs, mesopores with regular circular shape were observed in the pristine sample. These mesopores were formed due to the decomposition of PMMA islands in the emulsion during the carbonization process.⁸⁷ The mesopores maintained their shapes with smooth boundaries after light activation in the 1M-800 °C sample as shown in Figure 35i. However, with the high mass loss ratio in the 4M-1000 °C activation, the mesopore shape became more irregular, Figure 35l. A similar trend was also observed in the TEM images. The mesopores with smooth boundaries were observed in the pristine and 1M-800 °C samples, Figure 35g & j, marked by yellow circles. The mesopores became larger and irregular after severe activation in the 4M-1000 °C sample, Figure 35m. Moreover, the mesopores in the pristine and 1M-800 °C samples were separated from each other. However, with the mass loss in the KOH activation process, the mesopores began to expand and merge with each other into larger mesopores. In addition to the change of pore structure, KOH activation affected the interlayer spacing of graphitic turbostratic domain, the interlayer spacing (measured from TEM images from

five samples in each case) increased from 0.379 ± 0.008 nm to 0.494 ± 0.005 nm for the highly activated 4M-1000 °C sample as shown in Figure 35g-m. The increase in the interlayer spacing is a results of the intercalation of the reduced potassium during the KOH activation.^{90,91} During the KOH activation, the potassium (K) in KOH is reduced to metallic K at high temperature, which intercalate into the carbon lattices therefore expanding the interlayer spacing.⁹⁰

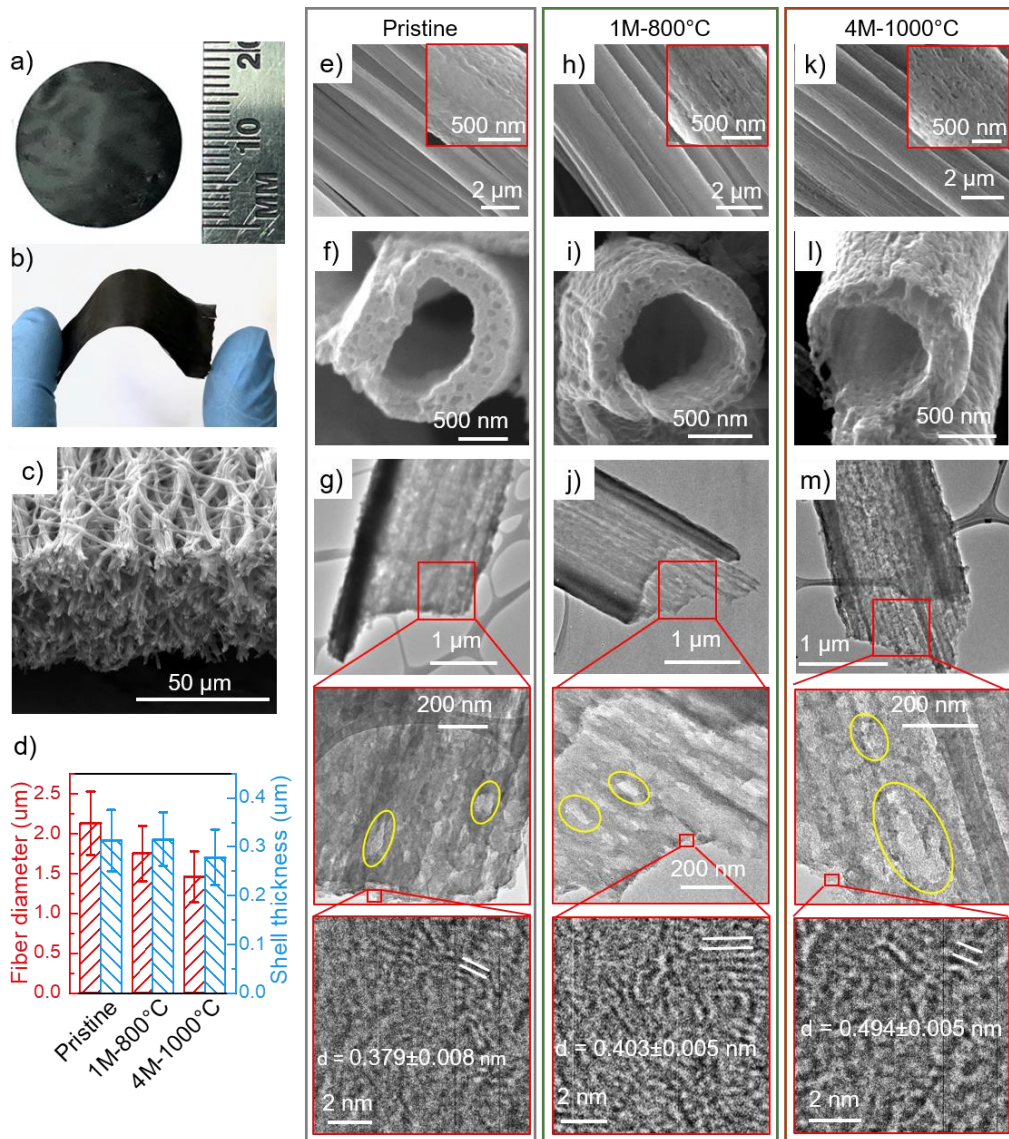


Figure 35. a) porous CNF electrode, b) bending of the activated porous CNF mat showing good structural integrity, c) SEM image of the cross-section of the activated porous CNF mat, d) fiber diameter and shell thickness for pristine, 1M-800 °C and 4M-1000 °C porous CNFs, surface morphology of e) pristine, h) 1M-800 °C and k) 4M-1000 °C porous CNFs, cross-sectional SEM images of f) pristine, i) 1M-800 °C and l) 4M-1000 °C porous CNFs and TEM images with different magnification of g) pristine, j) 1M-800 °C and m) 4M-1000 °C porous CNFs

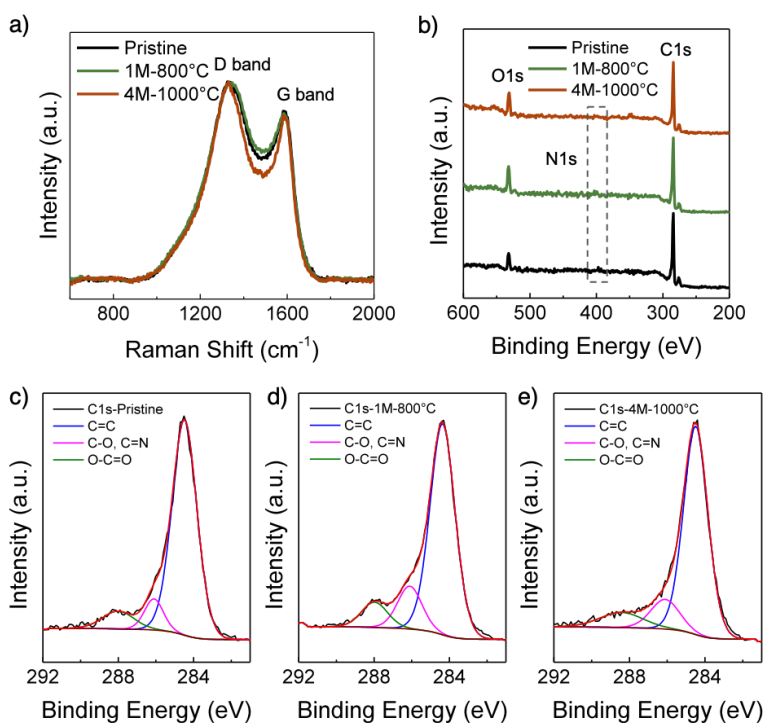


Figure 36. a) Raman spectra of pristine, 1M-800 °C and 4M-1000 °C porous CNFs, b) XPS spectra of pristine, 1M-800 °C and 4M-1000 °C porous CNFs, C1s peak of c) pristine, d) 1M-800 °C and e) 4M-1000 °C porous CNFs

Table 4. Chemical composition of porous CNFs

sample	I_D/I_G	C (at %)	N (at %)	O (at %)	C1s		
					C-O, C=N (%)	C=C (%)	O-C=O (%)
pristine	1.18	90.1	1.7	8.2	8.7	82.0	9.2
1M-800 °C	1.19	84.5	1.9	13.6	15.0	75.5	9.5
4M-1000 °C	1.21	84.4	0.7	14.9	13.0	77.1	9.9

Raman spectra of pristine, 1M-800 °C and 4M-1000 °C treated porous CNFs are presented in **Figure 36a**. All three samples had two peaks at ~ 1336 and ~ 1580 cm^{-1} , which correspond to the disorder (D) band and the graphitic (G) band, respectively. The intensity ratio of D and G bands (I_D/I_G) is an indication of the level of structural disorder in carbon materials.¹⁹ The I_D/I_G is 1.18, 1.19 and 1.21 for pristine, 1M-800 °C and 4M-1000 °C, respectively, suggesting no relative loss in the graphitic structure of the CNFs as a result of the activation.

The surface chemical composition of the pristine and KOH-activated porous CNFs was analyzed by XPS, as shown in Figure 36b-e. Strong C 1s, O 1s and a weak N 1s peaks were presented in all the survey scans (Figure 36b). The chemical composition for pristine and activated porous CNF is shown in **Table 2** was calculated as the relative area under the deconvoluted peaks. The percentage of O-C=O group increased slightly after the activation, while the C-O group showed a large increase. Moreover, as a result of the

higher content of oxygen containing groups, the porous CNFs mat and the electrode became more hydrophilic after KOH activation, possessing higher wettability in aqueous electrolyte.

Electrochemical performance: To evaluate the energy storage capability of the activated porous CNFs, the electrochemical performance of the samples was studied by cyclic voltammetry (CV) and galvanostatic charge/discharge in a symmetric two electrode system using 6 M KOH aqueous solution as electrolyte. The porous CNF electrodes are binder free and were used as-is after the KOH activation. The CV curves were obtained at various scan rates of 2 mV s^{-1} to 100 mV s^{-1} for different activation conditions. The CV curves for 1M-800 °C and 4M-1000 °C porous CNFs (Figure 37a) were nearly rectangular, indicating a capacitive behavior due to electrostatic double layer.⁹² The specific capacitance decreased with increasing scan rate as shown in Figure 37b. The highest specific capacitance (in each case obtained at 2 mV s^{-1}) was 36.4 F g^{-1} , 138.2 F g^{-1} and 191.3 F g^{-1} for pristine, 1M-800 °C and 4M-1000 °C porous CNFs, respectively.

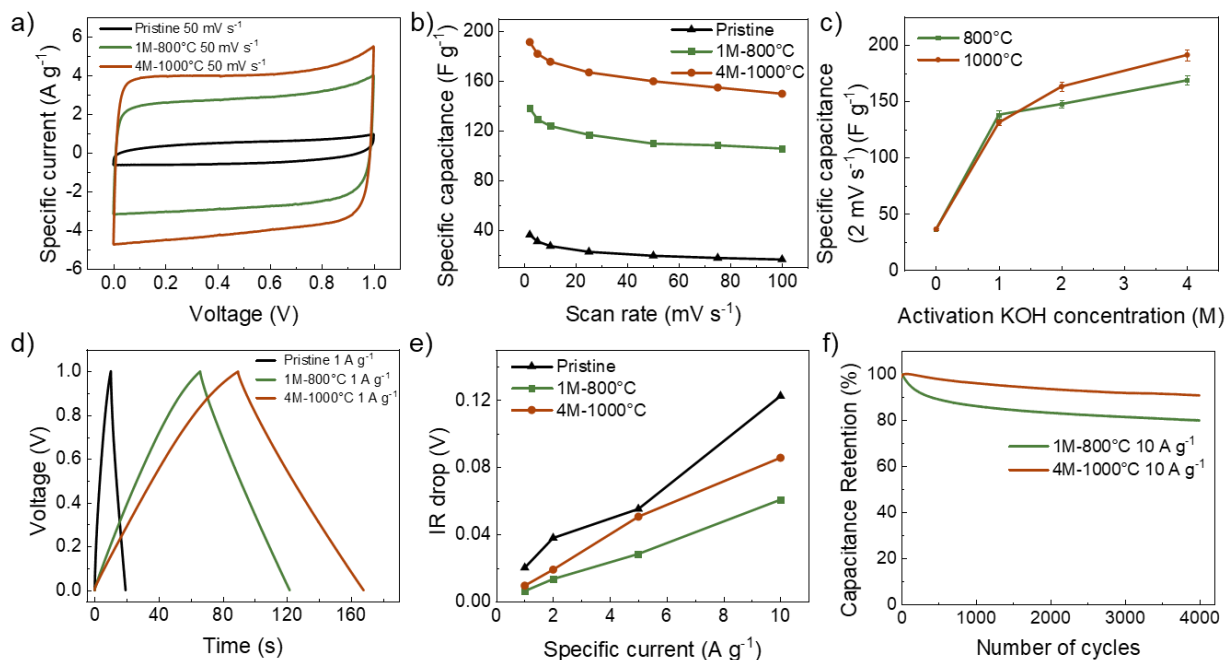


Figure 37. a) CV curves of pristine, 1M-800 °C and 4M-1000 °C porous CNFs with a scan rate of 50 mV s^{-1} , b) specific capacitance of pristine, 1M-800 °C and 4M-1000 °C porous CNFs at different scan rate, c) specific capacitance for different activation condition with a scan rate of 2 mV s^{-1} , error bars represent the uncertainty of the electrode weight measurement, d) galvanostatic charge/discharge curves for pristine, 1M-800 °C and 4M-1000 °C porous CNFs with a current density of 1 A g^{-1} , e) IR drop for pristine, 1M-800 °C and 4M-1000 °C porous CNFs with different current density and f) capacitance retention of 1M-800 °C and 4M-1000 °C porous CNFs after 4000 cycles

The KOH-activated porous CNFs showed good rate capability at high scan rate, the specific capacitance retained 76.5% and 78.3% when the scan rate is increased to 100 mV s^{-1} . This is due to the wide pore size distribution from both mesopores and micropores where the mesopores act as pathways for ion diffusion which helps the porous CNFs to maintain high capacitance at high scan rate.^{94,95} The specific capacitance evaluated at 2 mV s^{-1} for different activation conditions is shown in Figure 37c. The specific capacitance increased with higher activation KOH concentration and activation temperature, and the highest capacitance was reached with 4M-1000 °C activation.

The capacitive behavior was confirmed by the linear galvanostatic charge/discharge (CD) curves. The specific capacitance at current density of 1 A g^{-1} for pristine, 1M-800 °C and 4M-1000 °C porous CNFs was 18.5 F g^{-1} , 122.8 F g^{-1} and 158.0 F g^{-1} respectively. The voltage drop (IR drop) at the onset of the discharge curve at different current densities is shown in Figure 37e. The IR drop is small in all cases, suggesting that the test cells have very low equivalent series resistance (ESR). The KOH-activated porous CNFs showed lower IR drop compared to the pristine porous CNFs, which can be attributed to the improved hydrophilicity for the activated porous CNFs as discussed earlier.

The cycling stability of activated porous CNFs was investigated by galvanostatic charge/discharge for up to 4000 cycles. The results suggest that the activated porous CNFs have promising cycling stability, as shown in Figure 37f. The 1M-800 °C porous CNFs maintained 80% of the initial capacitance after 4000 cycles at 10 A g^{-1} , whereas the 4M-1000 °C porous CNFs retained 91% under the same test condition.

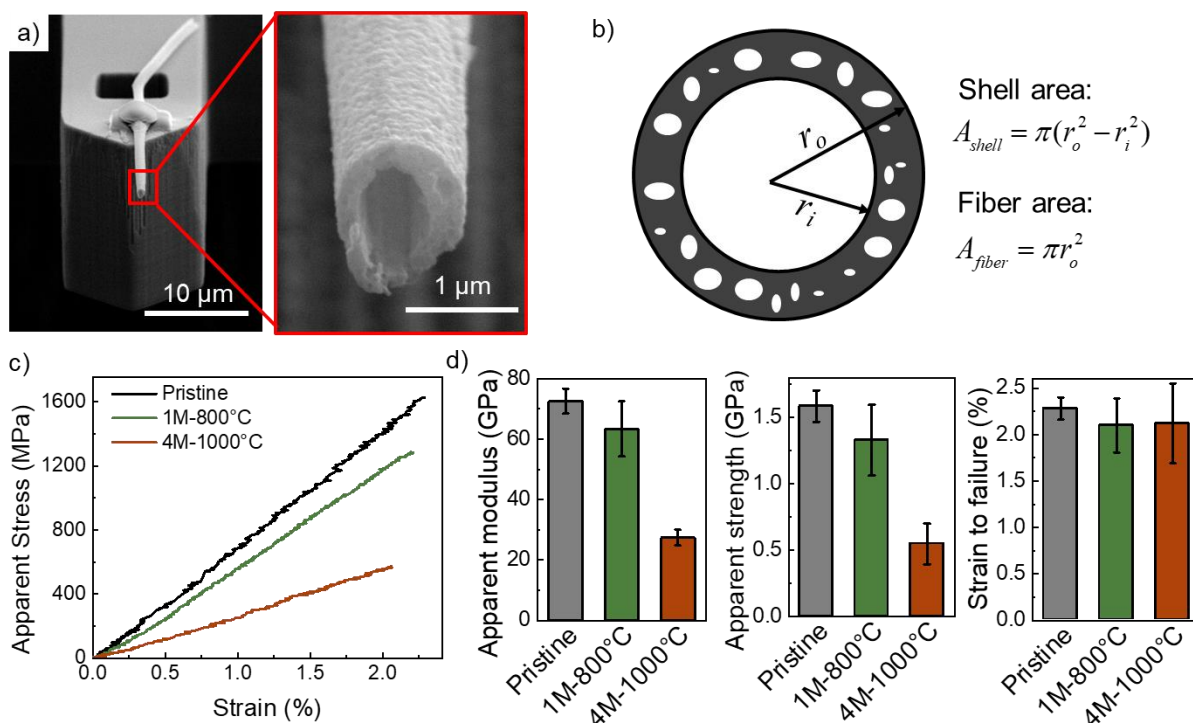


Figure 38. a) porous CNF fracture surface after the tensile test, b) schematic for the porous CNF, c) stress-strain curve for pristine, 1M-800 °C and 4M-1000 °C porous CNFs, d) apparent modulus, apparent strength and strain to failure for pristine, 1M-800 °C and 4M-1000 °C porous CNFs.

Table 5. Mechanical properties of porous CNFs

	Mass loss (%)	Strength (GPa)			Reduction	Modulus (GPa)			Reduction	Strain to failure (%)	Reduction
		Apparent	Eng			Apparent	Eng				
Pristine	N.A.	1.59 ± 0.12	0.96 ± 0.07		0	72.6 ± 4.1	44.0 ± 2.5		0	2.28 ± 0.12	0
1M-800 °C	13.2	1.33 ± 0.27	0.80 ± 0.16	16.2%		63.4 ± 9.1	38.1 ± 5.5	12.6%		2.10 ± 0.29	8.1%
4M-1000 °C	55.0	0.55 ± 0.15	0.32 ± 0.09	65.5%		27.4 ± 2.6	15.9 ± 1.5	62.3%		2.12 ± 0.43	7.2%

Mechanical characterization of porous CNFs: Single fiber tensile tests were performed on the pristine, 1M-800 °C and 4M-1000 °C porous CNFs to evaluate the load-bearing capability of the porous CNFs. Four porous CNFs were tested in each case. Fracture surfaces (as shown in **Figure 38a**) of the porous CNFs were observed in SEM to measure the shell area (A_{shell}) and fiber area (A_{fiber}), as shown in the schematic in Figure 38b. The apparent stress was calculated as $S_{apparent} = F / A_{shell}$, and the engineering stress was calculated as $S_{apparent} = F / A_{fiber}$ where F represent the force experience by the porous CNFs. The apparent stress excludes the hollow core to reflect the material properties (it does not exclude the area of the pores within the shell from the total area), whereas the engineering stress takes into account the hollow core, thus making the engineering strength a more realistic property to be considered for real applications. The apparent stress-strain curves remained linear until fracture in all three cases (Figure 38c), i.e., a brittle fracture behavior. As expected, the KOH activation reduced the mechanical properties by eliminating load-bearing material from porous CNFs as shown in Figure 38d and

Table 5. The apparent modulus and strength decreased by 12.6% and 16.2% for 1M-800 °C activation, and 62.3% and 65.5% for 4M-1000 °C activation, respectively. The strain to failure for both KOH-activated porous CNFs remained relatively close to the pristine porous CNFs

The reduction in strength and modulus as a result of KOH activation can be a result of the following three mechanisms. First, KOH activation will increase the porosity and reduce the load-bearing area. Second, pores can cause stress concentration which will reduce the strength. Third, KOH activation induces disorder in the graphitic turbostratic domains as discussed in Chapter 2.1. The porosity generated during the activation is proportional to the mass loss ratio. Close examination of the mechanical properties and mass loss ratio suggests that the modulus and strength reduction follow a similar trend as the mass loss ratio. For 1M-800 °C activation, the modulus reduction of 12.6% is very close to the 13.2% mass loss, suggesting that the reduction in modulus is mainly due to a loss in load-bearing area (first mechanism), whereas the 16.2% decrease in apparent strength is slightly larger than the mass loss, suggesting a small contribution of stress concentration and change in graphitic properties. The latter effect is expected because according to a previous study, the stress concentration around the pores are strongly related to the pore shape.⁸⁷ Since the 1M-800 °C activation condition was light, the pore structure and shape were preserved (Figure 35i,j) and the d-spacing had a small increase, as discussed in chapter 2.1. However, in the case of 4M-1000 °C, the respective 62.3% and 65.5% reduction in modulus and strength are higher than the 55.0% mass loss, indicating that in addition to the increase in porosity, the stress concentration around pores and change in graphitic domain may have contributed to the loss in the apparent strength and modulus. During 4M-1000 °C activation, the pores grew in size and became more irregular (Figure 35l,m), as discussed in chapter 2.1. These irregular pore walls increase the stress concentration. The graphitic turbostratic domain also became more disordered with a significantly higher d spacing (Figure 35m).

Trade-off between energy storage and load-bearing: An Ashby plot (**Figure 39a**) was used to compare the strength and capacitance of different porous CNFs and activated CFs. The capacitance increased by four times reaching 138.2 F g⁻¹ after the 1M-800 °C activation with only 16.2% decrease in strength. The greatest specific capacitance of 191.3 F g⁻¹ was achieved with 4M-1000 °C activation which is close to capacitance of graphene-based supercapacitors. However, this increase of capacitance comes at the cost of greater strength reduction (65.5%). While the strength of activated porous CNFs is slightly lower than activated CFs, the capacitance of activated porous CNFs is two orders of magnitude higher.

It is worth to compare the results presented here for CNFs with those on CFs. During the KOH activation, the chemical reaction happens on the surface of the carbon material. In the case of CFs, the interior of the CFs is very difficult to be activated without severe material loss on the periphery and degradation of the mechanical properties, resulting in a low SSA and capacitance. In the case of porous CNFs, there are abundant surfaces from mesopores and hollow core for the chemical reaction to take place, resulting in much higher SSA and capacitance (Figure 39b) with a mild activation. As a result, comparing

to activated CFs⁹³, the capacitance increased by 73 times (from 2.63 F g⁻¹ to 191.3 F g⁻¹) with only 86% decrease in apparent strength (from 3960 MPa to 550 MPa). This shows the great potential of using activated porous CNFs as structural supercapacitor electrode materials.

To analyze the trade-off between energy storage and load-bearing properties, a measure of multifunctional efficiency η_{mf} ^{96,97} can be defined as:

$$h_{mf} = h_e + h_s = \frac{\sigma_{mf}}{\sigma_0} + \frac{C_{mf}}{C_0},$$

where σ_{mf} and C_{mf} are the strength and specific capacitance of the multifunctional material and σ_0 and C_0 are the strength and specific capacitance of a typical reference material. The factor η_{mf} must be larger than 1.0 in order for the multifunctional material to save weight in the system. Although the multifunctional efficiency lacks objectivity because the chosen reference materials are not standardized, it does provide insight when comparing different cases. For the purpose of discussion, the specific capacitance of active carbon (125 F g⁻¹) is selected as the typical electrode material,⁹⁸ and the strength of T300 carbon fiber (3500 MPa, single fiber strength) is selected as the typical load-bearing material. The η_{mf} for pristine, 1M-800 °C and 4M-1000 °C porous CNFs based on the engineering strength is 1.33, 1.62 and 0.57 respectively suggesting that the 4M-1000 °C activated porous CNFs are most favored for structural supercapacitors.

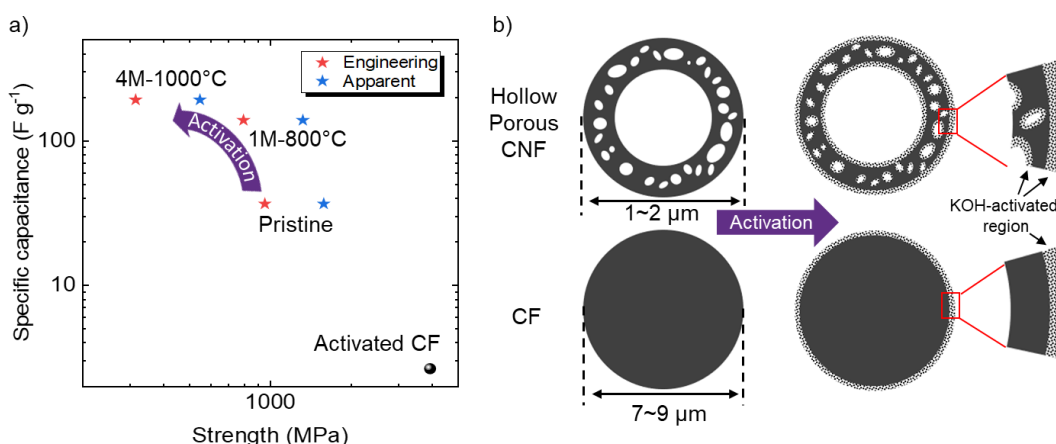


Figure 39. a) Ashby plot of specific capacitance vs strength for porous CNFs and activated CFs, porous CNFs from this work are marked by red stars (engineering strength) and blue stars (apparent strength), b) schematic showing difference between for activation of porous CNFs and CFs

Conclusion of this section

Porous CNFs were fabricated by coaxial and emulsion electrospinning. The porous CNFs were activated with KOH with different concentrations and activation temperatures. BET specific surface area for 1M-800 °C and 4M-1000 °C-treated porous CNFs increased by 20x and 34x to 1059.0 m² g⁻¹ and 1753.9 m² g⁻¹ comparing to pristine porous CNFs (52.3 m² g⁻¹), respectively. The significant increase in SSA is due to the meso and micro pores generated during the KOH activation. Microstructural analysis revealed that the mesopore structure were preserved in 1M-800 °C activation and the mesopores grew in size in 4M-1000 °C activation. The interlayer spacing in the graphitic domain also shows significant increase after activation. The activated porous CNFs showed excellent mechanical and energy storage capabilities. A clear trade-off between the energy storage and load-bearing capacities is demonstrated for the pristine and activated porous CNFs with different activation conditions. The specific capacitance increased by 4x and 5x, reaching 138.2

F g⁻¹ and 191.3 F g⁻¹ for 1M-800 °C and 4M-1000 °C porous CNFs comparing to pristine porous CNFs (36.4 F g⁻¹) with a 16.2 % and 65.5 % decrease in strength and a 12.6 % and 62.3 % decrease in modulus for 1M-800 °C and 4M-1000 °C porous CNFs respectively. The multifunctional efficiency for 1M-800 °C and 4M-1000 °C porous CNFs increased to 1.33 and 1.62, indicating a good combination of load-bearing and energy storage functions as structural supercapacitor electrode material. These results suggest that the 4M-1000 °C porous CNFs is more favorable for structural energy storage application.

4.6. Production of Graphene Nanoparticles and single layer graphene from graphite and expanded graphite via rod milling

Novel solid- and liquid-phase exfoliation methods for large-scale production of few- and mono-layer graphene with the use of rod-milling at room temperature and atmospheric pressure are respectively proposed by our group (Figure 40). For scalable production of graphene, a high-speed rod mill was designed, which can generate huge kinetic energy sufficient to break C–C bonds, and surely $\pi - \pi$ bonds between the graphite layers. While many of the exfoliation methods of graphite rely on rod mills to transfer kinetic energy to graphite, our method will benefit from the kinetic energy and momentum transfer between rods instead of balls to exfoliate graphite. The utilization of rods instead of balls significantly results in a considerable increase in the contact area, and better distributes the momentum to the graphite particles that are sandwiched between the rods. Based on preliminary data obtained in our lab, our approach is an efficient method for mass-production of graphene nanoplatelets powder with different and controllable thicknesses and dimensions.

The basics of our approach is as follows: To prepare few-layer graphene, the parent graphite is transferred into a stainless-steel jar filled with rods and rod-milled for a predetermined period of time (typically in the order of 1-6 days). A schematic diagram of the processes is shown in Figure 4. To mass-production of mono-layer graphene (Figure 40b), we can match the surface energy of graphite with a cheap organic solvent such as N-methyl-2-pyrrolidone (NMP) or N,N-dimethylformamide (DMF) with the surface tension of almost 40 mJ m^{-2} , which are the best candidates for suspending the graphene sheets. In fact, solvent surface energy of 68 mJ m^{-2} is close to the surface energy of graphite and can facilitate exfoliation procedure. At this stage, a huge shearing force applied by rod milling to the graphite is more than sufficient to overcome the van der Waals attraction between all the layers and wholly-exfoliate the graphene (Figure 4b). As an advantage of the proposed procedure, the filtrated solvent (NMP or DMF) can be reused, making procedure cost effective and more environmentally-friendly. Also, the lack of impurities in our proposed processes helps production of the high-quality graphene with ultra-high conductive properties, undoubtedly superior to previously reported graphene. In a typical experiment, 100 kg of the parent graphite and 100 lit of the organic solvent (NMP) will be poured into a stainless-steel jar and seal it. After milling for the specific period of time, the obtained mixture pump to the filtration system. Supernatant transfer back into the NMP tank and reuse in cycle and the filter cake is washed, separated and dry at 80°C for 24 h. The next step involved the rod-milling of dried sample for a short period of time (1 hr) to make it powder for presenting to the markets.

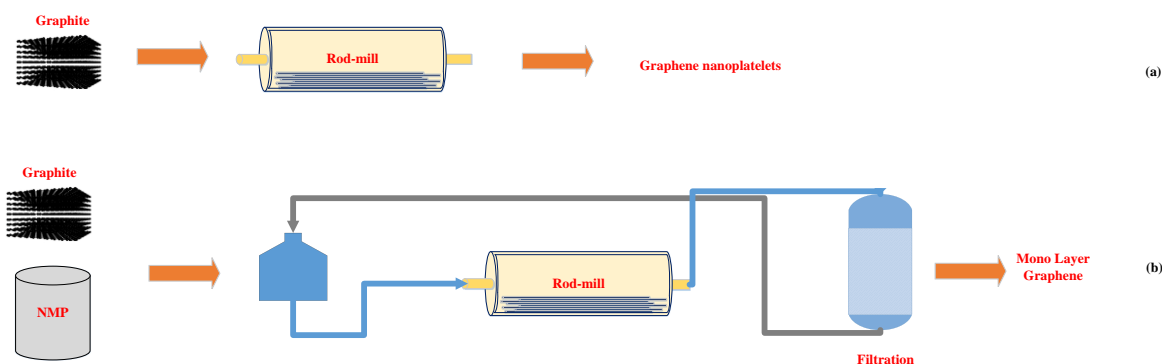


Figure 40. Preparation process of (a) few-layer graphene, (b) mono-layer graphene.

Results

Figure 41a-c show three TEM images of the graphene sheets synthesized by our proposed method. First of all, all the sheets are transparent, confirming that the synthesized graphene has few layers. Besides, the average dimension of graphene sheets is couple of micrometers, which is larger than the average dimension of products produced with mechanochemical methods by other companies like XG science (C-750). The elements' binding configuration in the graphene structure is evaluated with X-ray photoelectron spectroscopy (XPS). Figure 41d shows the XPS survey spectrum of the graphene sheets. The survey spectrum possesses three dominant peaks centered at ~ 284.1 , 529.1 , and 709.8 eV, corresponding to C 1s, O 1s, and Fe 2P, respectively. Atomic percentage of C, O and Fe elements are 83.19, 14.64 and 2.16, respectively. What we can get from preliminary results is that this method is a promising method for scalable production of graphene, however it is essential to find the optimum conditions and remove a majority of impurities. To reduce oxygen content to $< 4\%$, we need a rod-milling system working under vacuum or natural atmosphere such as N_2 or Ar.

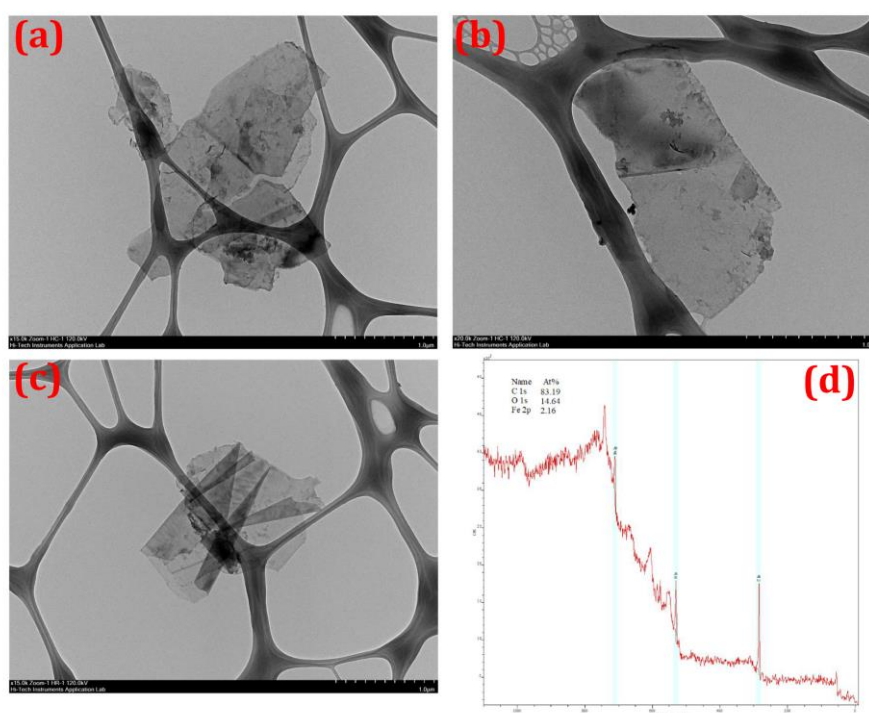


Figure 41. (a-c) TEM images and (d) XPS survey of graphene prepared by our method at rod's aspect ratio of 2, weight ratio of rods to graphite of 100, and rod-milling speed of 100 rpm for 6 days.

References

- (1) Cai, J.; Chawla, S.; Naraghi, M. Microstructural evolution and mechanics of hot-drawn CNT-reinforced polymeric nanofibers. *Carbon* **2016**, *109*, 813-822.
- (2) Chawla, S.; Cai, J.; Naraghi, M. Mechanical tests on individual carbon nanofibers reveals the strong effect of graphitic alignment achieved via precursor hot-drawing. *Carbon* **2017**, *117*, 208-219.
- (3) Chae, H. G.; Minus, M. L.; Kumar, S. Oriented and exfoliated single wall carbon nanotubes in polyacrylonitrile. *Polymer* **2006**, *47*, 3494-3504.
- (4) Papkov, D.; Zou, Y.; Andalib, M. N.; Goponenko, A.; Cheng, S. Z. D.; Dzenis, Y. A. Simultaneously Strong and Tough Ultrafine Continuous Nanofibers. *ACS Nano* **2013**, *7*, 3324-3331.
- (5) Cai, J. Z.; Chawla, S.; Naraghi, M. Microstructural evolution and mechanics of hot-drawn CNT-reinforced polymeric nanofibers. *Carbon* **2016**, *109*, 813-822.
- (6) B.D. Cullity, S. R. S.: *Elements of X-ray Diffraction, Third Edition*; Prentice-Hall: New York, 2001.
- (7) Sreekumar, T. V.; Liu, T.; Min, B. G.; Guo, H.; Kumar, S.; Hauge, R. H.; Smalley, R. E. Polyacrylonitrile single-walled carbon nanotube composite fibers. *Adv Mater* **2004**, *16*, 58-61.
- (8) Chae, H. G.; Newcomb, B. A.; Gulgunje, P. V.; Liu, Y. D.; Gupta, K. K.; Kamath, M. G.; Lyons, K. M.; Ghoshal, S.; Pramanik, C.; Giannuzzi, L.; Sahin, K.; Chasiotis, I.; Kumar, S. High strength and high modulus carbon fibers. *Carbon* **2015**, *93*, 81-87.
- (9) Naraghi, M.; Chasiotis, I.; Kahn, H.; Wen, Y.; Dzenis, Y. Novel method for mechanical characterization of polymeric nanofibers. *Rev Sci Instrum* **2007**, *78*.
- (10) Arshad, S. N.; Naraghi, M.; Chasiotis, I. Strong carbon nanofibers from electrospun polyacrylonitrile. *Carbon* **2011**, *49*, 1710-1719.
- (11) Beese, A. M.; Papkov, D.; Li, S. Y.; Dzenis, Y.; Espinosa, H. D. In situ transmission electron microscope tensile testing reveals structure-property relationships in carbon nanofibers. *Carbon* **2013**, *60*, 246-253.
- (12) Baniyadi, M.; Xu, Z.; Cai, J.; Daryadel, S.; Quevedo-Lopez, M.; Naraghi, M.; Minary-Jolandan, M. Correlation of annealing temperature, morphology, and electro-mechanical properties of electrospun piezoelectric nanofibers. *Polymer* **2017**, *127*, 192-202.

- (13) Deng, L. B.; Young, R. J.; van der Zwaag, S.; Picken, S. Characterization of the adhesion of single-walled carbon nanotubes in poly (p-phenylene terephthalamide) composite fibres. *Polymer* **2010**, *51*, 2033-2039.
- (14) Wang, Y.-X.; Wang, C.-G.; Bai, Y.-J.; Bo, Z. Effect of the drawing process on the wet spinning of polyacrylonitrile fibers in a system of dimethyl sulfoxide and water. *J Appl Polym Sci* **2007**, *104*, 1026-1037.
- (15) Liu, Y.; Chae, H. G.; Kumar, S. Gel-spun carbon nanotubes/polyacrylonitrile composite fibers. Part I: Effect of carbon nanotubes on stabilization. *Carbon* **2011**, *49*, 4466-4476.
- (16) Chae, H. G.; Minus, M. L.; Rasheed, A.; Kumar, S. Stabilization and carbonization of gel spun polyacrylonitrile/single wall carbon nanotube composite fibers. *Polymer* **2007**, *48*, 3781-3789.
- (17) Ramachandramoorthy, R.; Beese, A.; Espinosa, H. In situ electron microscopy tensile testing of constrained carbon nanofibers. *International Journal of Mechanical Sciences* **2017**.
- (18) Liu, C.-K.; Feng, Y.; He, H.-J.; Zhang, J.; Sun, R.-J.; Chen, M.-Y. Effect of carbonization temperature on properties of aligned electrospun polyacrylonitrile carbon nanofibers. *Materials & Design* **2015**, *85*, 483-486.
- (19) Zussman, E.; Chen, X.; Ding, W.; Calabri, L.; Dikin, D. A.; Quintana, J. P.; Ruoff, R. S. Mechanical and structural characterization of electrospun PAN-derived carbon nanofibers. *Carbon* **2005**, *43*, 2175-2185.
- (20) Cai, J.; Naraghi, M.: Effect of Templating Graphitization on Electrical Conductivity of Electrospun Carbon nanofiber. In *58th AIAA/ASCE/AHS/ASC Structures, Structural Dynamics, and Materials Conference; AIAA SciTech Forum; American Institute of Aeronautics and Astronautics*, 2017.
- (21) Shilpa; Das, S. K.; Afzal, M. A. F.; Srivastava, S.; Patil, S.; Sharma, A. Enhanced electrical conductivity of suspended carbon nanofibers: Effect of hollow structure and improved graphitization. *Carbon* **2016**, *108*, 135-145.
- (22) Cai, J. Z.; Naraghi, M. Computational analysis of electrical conduction in hybrid nanomaterials with embedded non-penetrating conductive particles. *Modell. Simul. Mater. Sci. Eng.* **2016**, *24*.
- (23) Askounis, A.; Yamada, Y.; Ikuta, T.; Takahashi, K.; Takata, Y.; Sefiane, K. On the linear dependence of a carbon nanofiber thermal conductivity on wall thickness. *AIP Advances* **2016**, *6*, 115119.

- (24) Cai, J.; Naraghi, M.: Developing a Numerical Scheme to Capture the Piezoresistivity of CNF/CNTs Hybrid Nanofibers. In *58th AIAA/ASCE/AHS/ASC Structures, Structural Dynamics, and Materials Conference*; AIAA SciTech Forum; American Institute of Aeronautics and Astronautics, 2017.
- (25) Cai, J. Z.; Chawla, S.; Naraghi, M. Piezoresistive effect of individual electrospun carbon nanofibers for strain sensing. *Carbon* **2014**, *77*, 738-746.
- (26) Wang, Y.; Serrano, S.; Santiago-Avilés, J. J. Raman characterization of carbon nanofibers prepared using electrospinning. *Synthetic Met* **2003**, *138*, 423-427.
- (27) Ferrari, A. C. Raman spectroscopy of graphene and graphite: Disorder, electron–phonon coupling, doping and nonadiabatic effects. *Solid State Communications* **2007**, *143*, 47-57.
- (28) Matthews, M. J.; Pimenta, M. A.; Dresselhaus, G.; Dresselhaus, M. S.; Endo, M. Origin of dispersive effects of the Raman D band in carbon materials. *Phys Rev B* **1999**, *59*, R6585-R6588.
- (29) Wang, Y.; Serrano, S.; Santiago-Aviles, J. J. Raman characterization of carbon nanofibers prepared using electrospinning. *Synth. Met.* **2003**, *138*, 423-427.
- (30) Rahaman, M. S. A.; Ismail, A. F.; Mustafa, A. A review of heat treatment on polyacrylonitrile fiber. *Polym. Degrad. Stab.* **2007**, *92*, 1421-1432.
- (31) Liu, Y. D.; Chae, H. G.; Kumar, S. Gel-spun carbon nanotubes/polyacrylonitrile composite fibers. Part III: Effect of stabilization conditions on carbon fiber properties. *Carbon* **2011**, *49*, 4487-4496.
- (32) Tyson, C. N. Fracture Mechanisms in Carbon-Fibers Derived from Pan in Temperature-Range 1000-2800 Degreesc. *J. Phys. D-Appl. Phys.* **1975**, *8*, 749-758.
- (33) Kim, M. A.; Jang, D.; Tejima, S.; Cruz-Silva, R.; Joh, H. I.; Kim, H. C.; Lee, S.; Endo, M. Strengthened PAN-based carbon fibers obtained by slow heating rate carbonization. *Scientific Reports* **2016**, *6*.
- (34) Reynolds, W. N.; Sharp, J. V. Crystal Shear Limit to Carbon-Fiber Strength. *Carbon* **1974**, *12*, 103-110.
- (35) Sahin, K.; Fasanella, N. A.; Chasiotis, I.; Lyons, K. M.; Newcomb, B. A.; Kamath, M. G.; Chae, H. G.; Kumar, S. High strength micron size

carbon fibers from polyacrylonitrile-carbon nanotube precursors. *Carbon* **2014**, *77*, 442-453.

(36) Ozkan, T.; Naraghi, M.; Chasiotis, I. Mechanical properties of vapor grown carbon nanofibers. *Carbon* **2010**, *48*, 239-244.

(37) Koziol, K.; Vilatela, J.; Moisala, A.; Motta, M.; Cunniff, P.; Sennett, M.; Windle, A. High-Performance Carbon Nanotube Fiber. *Science* **2007**, *318*, 1892-1895.

(38) Xu, Z.; Liu, Y.; Zhao, X.; Peng, L.; Sun, H.; Xu, Y.; Ren, X.; Jin, C.; Xu, P.; Wang, M.; Gao, C. Ultrastiff and Strong Graphene Fibers via Full-Scale Synergetic Defect Engineering. *Adv Mater* **2016**, *28*, 6449-6456.

(39) Sheng, L.; Wei, T.; Liang, Y.; Jiang, L.; Qu, L.; Fan, Z. Ultra-high toughness all graphene fibers derived from synergetic effect of interconnected graphene ribbons and graphene sheets. *Carbon* **2017**, *120*, 17-22.

(40) Rath, J. P.; Chaki, T. K.; Khastgir, D. Change in fiber properties due to the heat treatment of nylon 6 tire cords. *J Appl Polym Sci* **2008**, *108*, 3960-3967.

(41) Kromm, F. X.; Lorriot, T.; Coutand, B.; Harry, R.; Quenisset, J. M. Tensile and creep properties of ultra high molecular weight PE fibres. *Polymer Testing* **2003**, *22*, 463-470.

(42) Motta, M.; Moisala, A.; Kinloch, I. A.; Windle, A. H. High Performance Fibres from 'Dog Bone' Carbon Nanotubes. *Adv Mater* **2007**, *19*, 3721-3726.

(43) Vollrath, F.; Knight, D. P. Liquid crystalline spinning of spider silk. *Nature* **2001**, *410*, 541.

(44) Naraghi, M.; Filleter, T.; Moravsky, A.; Locascio, M.; Loutfy, R. O.; Espinosa, H. D. A Multiscale Study of High Performance Double-Walled Nanotube-Polymer Fibers. *Acs Nano* **2010**, *4*, 6463-6476.

(45) Prudenziati, M.; Morten, B.; Cilloni, F.; Ruffi, G. Very High-Strain Sensitivity in Thick-Film Resistors - Real and False Super Gauge Factors. *Sensor Actuator* **1989**, *19*, 401-414.

(46) Wetzel, B.; Rosso, P.; Hauptert, F.; Friedrich, K. Epoxy nanocomposites – fracture and toughening mechanisms. *Engineering Fracture Mechanics* **2006**, *73*, 2375-2398.

(47) Quaresimin, M.; Schulte, K.; Zappalorto, M.; Chandrasekaran, S. Toughening mechanisms in polymer nanocomposites: From experiments to modelling. *Compos Sci Technol* **2016**, *123*, 187-204.

(48) Chatterjee, S.; Nafezarefi, F.; Tai, N. H.; Schlagenhaut, L.; Nüesch, F. A.; Chu, B. T. T. Size and synergy effects of nanofiller hybrids including graphene nanoplatelets and carbon nanotubes in mechanical properties of epoxy composites. *Carbon* **2012**, *50*, 5380-5386.

(49) Chandrasekaran, S.; Sato, N.; Tölle, F.; Mülhaupt, R.; Fiedler, B.; Schulte, K. Fracture toughness and failure mechanism of graphene based epoxy composites. *Compos Sci Technol* **2014**, *97*, 90-99.

(50) Johnson, D. J. Structure Property Relationships in Carbon-Fibers. *J. Phys. D-Appl. Phys.* **1987**, *20*, 286-291.

(51) Newcomb, B. A.; Giannuzzi, L. A.; Lyons, K. M.; Gulgunje, P. V.; Gupta, K.; Liu, Y.; Kamath, M.; McDonald, K.; Moon, J.; Feng, B.; Peterson, G. P.; Chae, H. G.; Kumar, S. High resolution transmission electron microscopy study on polyacrylonitrile/carbon nanotube based carbon fibers and the effect of structure development on the thermal and electrical conductivities. *Carbon* **2015**, *93*, 502-514.

(52) Chae, H. G.; Choi, Y. H.; Minus, M. L.; Kumar, S. Carbon nanotube reinforced small diameter polyacrylonitrile based carbon fiber. *Compos Sci Technol* **2009**, *69*, 406-413.

(53) Naraghi, M.; Chawla, S. Carbonized Micro- and Nanostructures: Can Downsizing Really Help? *Materials* **2014**, *7*, 3820-3833.

(54) Liu, J.; Yue, Z.; Fong, H. Continuous Nanoscale Carbon Fibers with Superior Mechanical Strength. *Small* **2009**, *5*, 536-542.

(55) Chae, H. G.; Newcomb, B. A.; Gulgunje, P. V.; Liu, Y.; Gupta, K. K.; Kamath, M. G.; Lyons, K. M.; Ghoshal, S.; Pramanik, C.; Giannuzzi, L.; Şahin, K.; Chasiotis, I.; Kumar, S. High strength and high modulus carbon fibers. *Carbon* **2015**, *93*, 81-87.

(56) Bhattacharyya, A. R.; Sreekumar, T. V.; Liu, T.; Kumar, S.; Ericson, L. M.; Hauge, R. H.; Smalley, R. E. Crystallization and orientation studies in polypropylene/single wall carbon nanotube composite. *Polymer* **2003**, *44*, 2373-2377.

(57) Papkov, D.; Beese, A. M.; Goponenko, A.; Zou, Y.; Naraghi, M.; Espinosa, H. D.; Saha, B.; Schatz, G. C.; Moravsky, A.; Loutfy, R.; Nguyen, S. T.; Dzenis, Y. Extraordinary Improvement of the Graphitic Structure of Continuous Carbon Nanofibers Templated with Double Wall Carbon Nanotubes. *Acs Nano* **2012**, *7*, 126-142.

(58) Zhang, Y.; Song, K.; Meng, J.; Minus, M. L. Tailoring Polyacrylonitrile Interfacial Morphological Structure by Crystallization in the

Presence of Single-Wall Carbon Nanotubes. *Acs Appl Mater Inter* **2013**, *5*, 807-814.

(59) Haggemueller, R.; Fischer, J. E.; Winey, K. I. Single Wall Carbon Nanotube/Polyethylene Nanocomposites: Nucleating and Templating Polyethylene Crystallites. *Macromolecules* **2006**, *39*, 2964-2971.

(60) Wang, P.-H.; Ghoshal, S.; Gulgunje, P.; Verghese, N.; Kumar, S. Polypropylene nanocomposites with polymer coated multiwall carbon nanotubes. *Polymer* **2016**, *100*, 244-258.

(61) Cai, J.; Naraghi, M. Non-intertwined Graphitic Domains in Nanoscale leads to Super Strong and tough Continuous 1D Nanostructures. *Carbon*.

(62) Li, X.; Yang, Y.; Zhao, Y.; Lou, J.; Zhao, X.; Wang, R.; Liang, Q.; Huang, Z. Electrospinning fabrication and in situ mechanical investigation of individual graphene nanoribbon reinforced carbon nanofiber. *Carbon* **2017**, *114*, 717-723.

(63) Toray Data Sheet. <http://www.toraycfa.com/pdfs/T300DataSheet.pdf> (accessed Oct. 2017).

(64) Xu, Z.; Liu, Y.; Zhao, X.; Peng, L.; Sun, H.; Xu, Y.; Ren, X.; Jin, C.; Xu, P.; Wang, M.; Gao, C. Ultrastiff and Strong Graphene Fibers via Full - Scale Synergetic Defect Engineering. *Adv Mater* **2016**, *28*, 6449-6456.

(65) Cai, J.; Naraghi, M.: Effect of Templating Graphitization of Functionalized SWNTs on Mechanical Properties of Hot-drawn Carbon Nanofibers. In *2018 AIAA/ASCE/AHS/ASC Structures, Structural Dynamics, and Materials Conference; AIAA SciTech Forum; American Institute of Aeronautics and Astronautics*, 2018.

(66) Liu, Y.; Kumar, S. Polymer/Carbon Nanotube Nano Composite Fibers—A Review. *Acs Appl Mater Inter* **2014**, *6*, 6069-6087.

(67) Krucinska, I.; Stypka, T. Direct Measurement of the Axial Poisson Ratio of Single Carbon-Fibers. *Compos Sci Technol* **1991**, *41*, 1-12.

(68) Shah, P. H.; Batra, R. C.: Effect of Covalent Functionalization on Young's Modulus of a Single-Wall Carbon Nanotube. In *Modeling of Carbon Nanotubes, Graphene and their Composites*; Tserpes, K. I., Silvestre, N., Eds.; Springer International Publishing: Cham, 2014; pp 111-134.

(69) Saha, B.; Schatz, G. C. Carbonization in Polyacrylonitrile (PAN) Based Carbon Fibers Studied by ReaxFF Molecular Dynamics Simulations. *J Phys Chem B* **2012**, *116*, 4684-4692.

(70) Du, F. M.; Fischer, J. E.; Winey, K. I. Effect of nanotube alignment on percolation conductivity in carbon nanotube/polymer composites. *Phys. Rev. B* **2005**, *72*.

(71) Hu, N.; Masuda, Z.; Yan, C.; Yamamoto, G.; Fukunaga, H.; Hashida, T. The electrical properties of polymer nanocomposites with carbon nanotube fillers. *Nanotechnology* **2008**, *19*.

(72) Klein, C. A. Pyrolytic Graphites - Their Description as Semimetallic Molecular Solids. *J Appl Phys* **1962**, *33*, 3338-&.

(73) Simmons, J. G. Generalized Formula for Electric Tunnel Effect between Similar Electrodes Separated by a Thin Insulating Film. *J. Appl. Phys.* **1963**, *34*, 1793-&.

(74) Kim, C.; Yang, K. S.; Kojima, M.; Yoshida, K.; Kim, Y. J.; Kim, Y. A.; Endo, M. Fabrication of electrospinning-derived carbon nanofiber webs for the anode material of lithium-ion secondary batteries. *Adv Funct Mater* **2006**, *16*, 2393-2397.

(75) Bao, W. S.; Meguid, S. A.; Zhu, Z. H.; Meguid, M. J. Modeling electrical conductivities of nanocomposites with aligned carbon nanotubes. *Nanotechnology* **2011**, *22*.

(76) Brebbia, C. A.; Walker, S.: *Boundary Element Techniques in Engineering*; Elsevier Science, 2013. pp. 47-48.

(77) Balberg, I.; Binenbaum, N. Cluster Structure and Conductivity of 3-Dimensional Continuum-Systems. *Phys Rev A* **1985**, *31*, 1222-1225.

(78) Alberty, J.; Carstensen, C.; Funken, S. A. Remarks around 50 lines of Matlab: short finite element implementation. *Numer Algorithms* **1999**, *20*, 117-137.

(79) Darby, M. I.; Kanellopoulos, V. N. Theory of fibre buckling in carbon-fibre reinforced plastics. *Journal of Physics D: Applied Physics* **1987**, *20*, 298-302.

(80) Mueller, C.; Gorius, A.; Nazarenko, S.; Hiltner, A.; Baer, E. Single Fiber Microbuckling in a Model Composite. *J Compos Mater* **1996**, *30*, 1912-1921.

(81) Slesarenko, V.; Rudykh, S. Microscopic and macroscopic instabilities in hyperelastic fiber composites. *Journal of the Mechanics and Physics of Solids* **2017**, *99*, 471-482.

(82) Chen, Y.; Liu, Y.; Yan, Y.; Zhu, Y.; Chen, X. Helical coil buckling mechanism for a stiff nanowire on an elastomeric substrate. *Journal of the Mechanics and Physics of Solids* **2016**, *95*, 25-43.

- (83) Antartis, D. A.; Mott, R. N.; Chasiotis, I. Silicon nanosprings fabricated by glancing angle deposition for ultra-compliant films and interfaces. *Materials & Design* **2018**, *144*, 182-191.
- (84) Ciarletta, P.; Destrade, M. Torsion instability of soft solid cylinders. *IMA Journal of Applied Mathematics* **2014**, *79*, 804-819.
- (85) Mora, S.; Abkarian, M.; Tabuteau, H.; Pomeau, Y. Surface instability of soft solids under strain. *Soft Matter* **2011**, *7*.
- (86) Bicerano, J.: *Prediction of polymer properties*; Marcel Dekker, 2002.
- (87) Chen, Y.; Cai, J.; Boyd, J. G.; Kennedy, W. J.; Naraghi, M. Mechanics of Emulsion Electrospun Porous Carbon Fibers as Building Blocks of Multifunctional Materials. *ACS Appl. Mater. Interfaces* **2018**, *10*, 38310-38318.
- (88) Zhang, S. L.; Pan, N. Supercapacitors Performance Evaluation. *Adv. Energy. Mater.* **2015**, *5*.
- (89) Stoller, M. D.; Ruoff, R. S. Best practice methods for determining an electrode material's performance for ultracapacitors. *Energy Environ. Sci.* **2010**, *3*, 1294-1301.
- (90) Wang, J.; Kaskel, S. KOH activation of carbon-based materials for energy storage. *J. Mater. Chem.* **2012**, *22*.
- (91) Yoon, S. H.; Lim, S.; Song, Y.; Ota, Y.; Qiao, W. M.; Tanaka, A.; Mochida, I. KOH activation of carbon nanofibers. *Carbon* **2004**, *42*, 1723-1729.
- (92) Zhu, Y.; Murali, S.; Stoller, M. D.; Ganesh, K. J.; Cai, W.; Ferreira, P. J.; Pirkle, A.; Wallace, R. M.; Cychosz, K. A.; Thommes, M.; Su, D.; Stach, E. A.; Ruoff, R. S. Carbon-based supercapacitors produced by activation of graphene. *Science* **2011**, *332*, 1537-1541.
- (93) Qian, H.; Diao, H.; Shirshova, N.; Greenhalgh, E. S.; Steinke, J. G.; Shaffer, M. S.; Bismarck, A. Activation of structural carbon fibres for potential applications in multifunctional structural supercapacitors. *J. Colloid Interface Sci.* **2013**, *395*, 241-248.
- (94) Zhi, M. J.; Yang, F.; Meng, F. K.; Li, M. Q.; Manivannan, A.; Wu, N. Q. Effects of Pore Structure on Performance of An Activated-Carbon Supercapacitor Electrode Recycled from Scrap Waste Tires. *ACS Sustainable Chem. Eng.* **2014**, *2*, 1592-1598.
- (95) Zhi, M.; Liu, S.; Hong, Z.; Wu, N. Electrospun activated carbon nanofibers for supercapacitor electrodes. *RSC Adv.* **2014**, *4*, 43619-43623.

(96) Chan, K. Y.; Jia, B.; Lin, H.; Hameed, N.; Lee, J. H.; Lau, K. T. A critical review on multifunctional composites as structural capacitors for energy storage. *Compos. Struct.* **2018**, *188*, 126-142.

(97) Kwon, S. R.; Harris, J.; Zhou, T.; Loufakis, D.; Boyd, J. G.; Lutkenhaus, J. L. Mechanically Strong Graphene/Aramid Nanofiber Composite Electrodes for Structural Energy and Power. *Acs Nano* **2017**, *11*, 6682-6690.

(98) Gamby, J.; Taberna, P. L.; Simon, P.; Fauvarque, J. F.; Chesneau, M. Studies and characterisations of various activated carbons used for carbon/carbon supercapacitors. *J. Power Sources* **2001**, *101*, 109-116.